

# Kazakh-British Technical University

Kair Kh. Nussupov, Nurzhan B. Beisenkhanov, Assanali T. Sultanov.

The Formation of Silicon Carbide in the  
Silicon Surface Layers by Multiple  
Implantation of Accelerated C Ions into Si.

ИНФОРМАЦИОННОЕ ОБЕСПЕЧЕНИЕ КОМПЛЕКСНОЙ ПРОГРАММЫ  
НАУЧНО-ТЕХНИЧЕСКОГО ПРОГРЕССА СТРАН - ЧЛЕНОВ СЭВ

до 2000 года

МЕЖДУНАРОДНЫЙ ЦЕНТР  
НАУЧНОЙ И ТЕХНИЧЕСКОЙ  
ИНФОРМАЦИИ

ИНСТИТУТ ПРОБЛЕМ  
ТЕХНОЛОГИИ МИКРОЭЛЕКТРОНИКИ И  
ОСОБОЧИСТЫХ МАТЕРИАЛОВ  
АН СССР

ИОННО-ЛУЧЕВАЯ МОДИФИКАЦИЯ  
МАТЕРИАЛОВ

АНАЛИТИЧЕСКИЙ ОБЗОР

МОСКВА  
1987

ПРИОРИТЕТНЫЕ НАПРАВЛЕНИЯ

ЭЛЕКТРОНИЗАЦИЯ НАРОДНОГО ХОЗЯЙСТВА  
НОВЫЕ МАТЕРИАЛЫ И ТЕХНОЛОГИИ ИХ ПРОИЗВОДСТВА И ОБРАБОТКИ

Заметное место среди опубликованных работ занимают исследования коррозии металлов при воздействии высокотемпературной окислительной среды, а также водной коррозии. Важное значение этих проблем обусловлено созданием аппаратов новой техники.

В ряде цитируемых работ суммируются некоторые результаты промышленного применения ионной имплантации для улучшения механических свойств металлов.

Предлагаемый библиографический справочник по имплантации ионов в металлы свидетельствует о непрерывном прогрессе наших знаний об особенностях и технологических возможностях метода.

С. ИОННАЯ ИМПЛАНТАЦИЯ В ПОЛУПРОВОДНИКИ

Методика ионной имплантации в полупроводники

Продолжается развитие ускорительной техники по трем новым линиям:

а) использование ионов очень высоких энергий (более 1 МэВ) для решения специальных задач, связанных с созданием "скрытых" слоев, особенно в GaAs и вероятным развитием применения трехмерных интегральных схем;

б) развитие установок с заторможенными ионными пучками (очень малые энергии).

В СССР, насколько известно, пока есть лишь одна установка в ИФЭ АН КазССР;

в) острофокусные имплантационные ускорители. По некоторым данным, особенно значительных успехов достигла фирма "Extrion" в США. Много и успешно работают японские исследователи (лаборатория Наиба в Осаке, фирма Хитати). Значительны также успехи в использовании острофокусированных электронных пучков для решения задач микроэлектроники.

Вызывает серьезный интерес новый метод кластерных ионов, который, строго говоря, не включает в себя элемента "имплантации", т.е. внедрения ионов в уже готовую подложку. Этот метод, позволяющий в широких пределах менять среднюю энергию взаимодействия частиц, из которых растет пленка, заслуживает самого внимательного изучения и скорейшего экспериментального осуществления в СССР.

Совершенно очевидно, что воспроизводимые результаты в исследовательских, а также и в прикладных работах можно получать только в установках с достаточно совершенной системой откачки (безмасляный вакуум).

Вторичные эффекты, сопровождающие имплантацию ионов в полупроводники и не описываемые количественно имеющимися теоретическими моделями

На последней международной конференции в Будапеште серьезное внимание было уделено неоднократно наблюдавшимся в таких материалах, как кремний, алмаз, арсенид галлия и т.д. явлениям аномально глубокого проникновения примесей, внедренных в качестве ускоренных ионов, не описываемых общепринятыми моделями, а также аномалий, обусловленных радиационными дефектами, "мигрирующими" необычными путями. Сопоставление достаточно многочисленных публикаций, вклю-

In the book "Ion-beam modification of materials" (Moscow, 1987), on the problems of developing installations with inhibited ion beams (very low energies), it is said that "In the USSR, as far as is known, there is so far only one installation at the Institute of High Energy Physics of the Academy Sciences of the Republic of Kazakhstan.

This accelerator is transferred to low energies by Professor Kair Nusupov.

## References

- 1 Nussupov K.Kh., Beisenkhanov N.B. and J.Tokbakov. Investigation of Structure and Phase Transformations in Silicon Implanted by C at Room Temperature // Nucl. Instrum. and Meth. in Phys. Res. – B103. – 1995. – P. 161–174.
- 2 Nussupov K.Kh., Beisenkhanov N.B., Keiinbay S., Sultanov A.T. Silicon carbide synthesized by RF magnetron sputtering in the composition of a double layer antireflection coating SiC/MgF<sub>2</sub>. Optical Materials. 128. 2022. 112370. ИМПАКТ-фактор 3.75.
- 3 Nussupov K.Kh., Sigle V.O. and Beisenkhanov N.B. Investigation of the formation of Si and SiC crystalline phases in room temperature C implanted Si //Nucl. Instrum. and Meth. in Phys.Res. – B82. – 1993. – P.69–79.
- 4 S.A. Kukushkin\*, K.Kh. Nussupov, A.V. Osipov, N.B. Beisenkhanov\*, D.I. Bakranova. Structural properties and parameters of epitaxial silicon carbide films, grown by atomic substitution on the high-resistance (111) oriented silicon. // Superlattices and Microstructures. 111. 2017. 899-911.
- 5 Kair Kh. Nussupov and Nurzhan B. Beisenkhanov. The Formation of Silicon Carbide in the SiC<sub>x</sub> Layers (x = 0.03–1.4) Formed by Multiple Implantation of C Ions in Si. // In book: Silicon Carbide - Materials, Processing and Applications in Electronic Devices. Moumita Mukherjee (Ed.). 2011. Chapter 4. *InTech*. PP. 69-114.
- 6 K.Kh. Nussupov\*, N.B. Beisenkhanov, D.I. Bakranova, S. Keinbai, A.A. Turakhun, A.A. Sultan. Low-temperature synthesis of α-SiC nanocrystals. Physics of the Solid State. Vol. 61, iss. 12. 2019. P.2473-2479.
- 7 Kair Kh. Nussupov and Nurzhan B. Beisenkhanov. Ion Synthesis of SiC and Its Instability at High Temperatures // In book: Physics and Technology of Silicon Carbide Devices. – Dr. Yasuto Hijikata (Ed.). 2013. Chapter 3. *InTech*. PP.47–96.
- 8 K.Kh. Nussupov, N.B. Beisenkhanov, S.K. Zharikov, I.K. Beisembetov, B.K. Kenzhaliev, T.K. Akhmetov, and B.Zh. Seitov. Structure and Composition of Silicon Carbide Films Synthesized by Ion Implantation. Physics of the Solid State. 2014, Vol. 56 (11), pp. 2307–2321.
- 9 Beisenkhanov N. B. Crystallization of β-SiC in thin SiC<sub>x</sub> layers (x = 0.03–1.4) synthesized by multiple implantation of carbon ions into silicon // Technical Physics. – 2011. - Vol. 56, № 2. - P. 274–281.
- 10 Nussupov K.Kh., Beisenkhanov N.B., Valitova I.V., Mit' K.A., Mukhamedshina D.M., Dmitrieva E.A. Structure properties of carbon implanted silicon layers // J. of Materials Science: Materials in Electronics. – 2008. – 19. – P. 254–262.



## Laboratory of Alternative Energy and Nanotechnology

- Activities of the laboratory
- Elaboration of a safe technology for the production of silicon solar cells
- Development of small-sized wind turbines
- Development and modernization of the heavy ion accelerator
- Synthesis and study of thin nanolayers (1 - 100 nm)

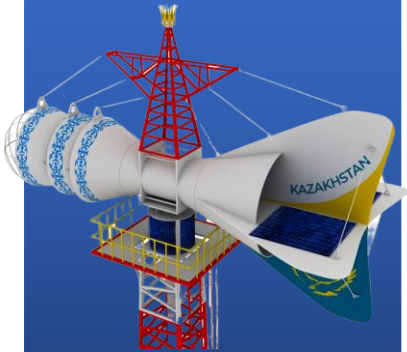




# Laboratory of Alternative Energy and Nanotechnology



**Wind Energy**



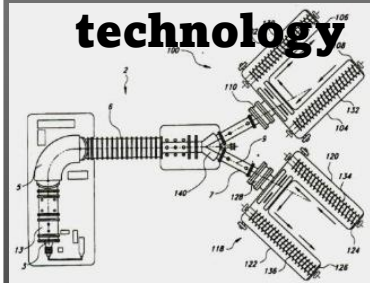
**Solar Energy**



**Study and synthesis of thin films**



**Development of accelerator technology**



# Wind Energy

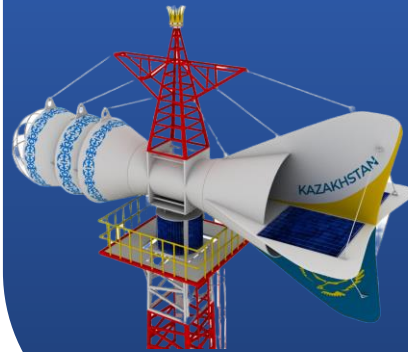


# KBTU



In January in Central Kazakhstan the average monthly wind speed is 4 - 6 m/s, and in South Kazakhstan it drops to 4 - 2 m/s. In summer, the wind speed decreases. The average monthly wind speed in July in the north is 2-3 m/s, in the south - 1-2 m/s.

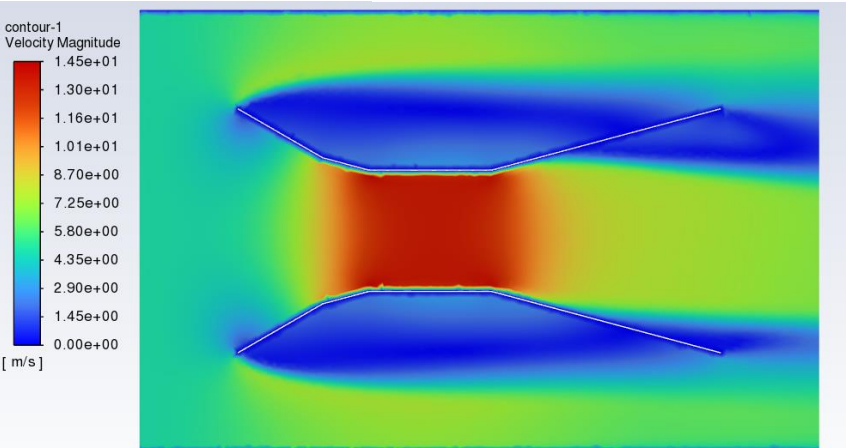
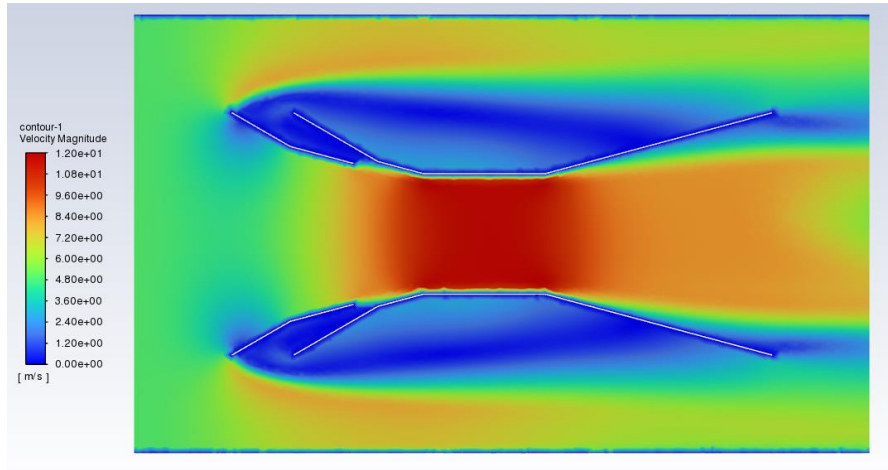
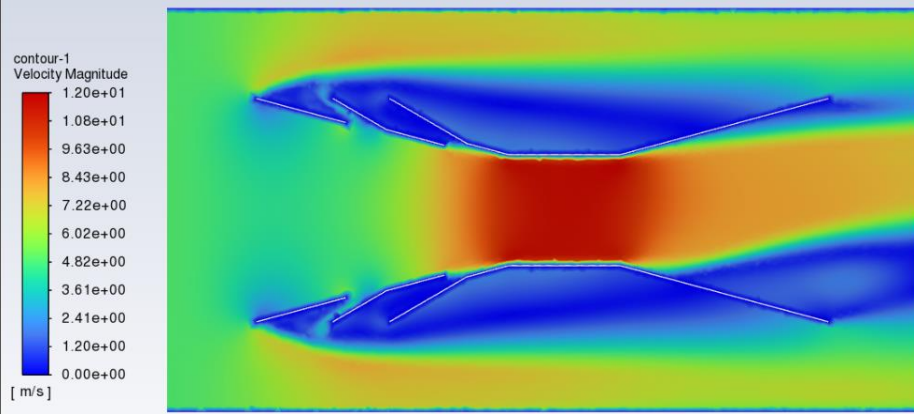
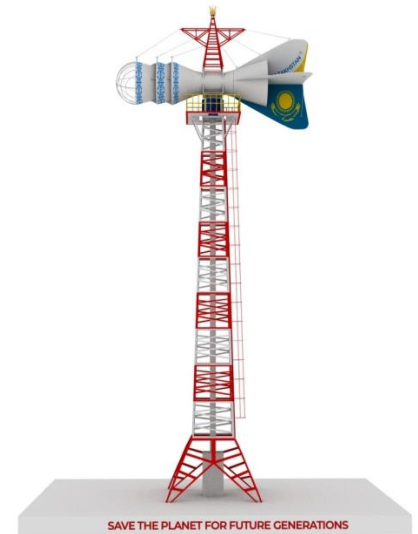
The wind generator starts to produce current when the wind is 3 m/s and turns off when the wind is more than 25 m/s. The maximum power is achieved with a wind of 15 m/s.



# Wind Energy




# KBTU



## Wind Energy



SAVE THE PLANET FOR FUTURE GENERATIONS



Europäisches Patentamt  
European Patent Office  
Office européen des brevets


URKUNDE	CERTIFICATE	CERTIFICAT
<p><b>Europäisches Patent</b></p> <p>Es wird hiermit bescheinigt, dass für die in der Patentschrift beschriebene Erfindung ein europäisches Patent für die in der Patentschrift bezeichneten Vertragsstaaten erteilt worden ist.</p>	<p><b>European patent</b></p> <p>It is hereby certified that a European patent has been granted in respect of the invention described in the patent specification for the Contracting States designated in the specification.</p>	<p><b>Brevet européen</b></p> <p>Il est certifié qu'un brevet européen a été délivré pour l'invention décrite dans le fascicule de brevet, pour les Etats contractants désignés dans le fascicule de brevet.</p>
<p>Europäisches Patent Nr. European patent No. Brevet européen n°</p>	<p><b>3411590</b></p>	
<p>Patentinhaber Proprietor(s) of the patent Titulaire(s) du brevet</p>	<p><b>Nussupov, Kair</b> ULI Zharskov 167-76 Almaty 050057/KZ</p> <p><b>JSC "Kazakh-British Technical University"</b> ULI Tole bi 69 Almaty 050000/KZ</p>	

München, den  
Munich,  
Munich, le

*António Campinos*  
**António Campinos**  
Präsident des Europäischen Patentamts  
President of the European Patent Office  
Président de l'Office européen des brevets

31.07.19

United States of America



To Promote the Progress  
of Science and Useful Arts

The Director

of the United States Patent and Trademark Office has received an application for a patent for a new and useful invention. The title and description of the invention are enclosed. The requirements of law have been complied with, and it has been determined that a patent on the invention shall be granted under the law.

Therefore, this United States

# Patent

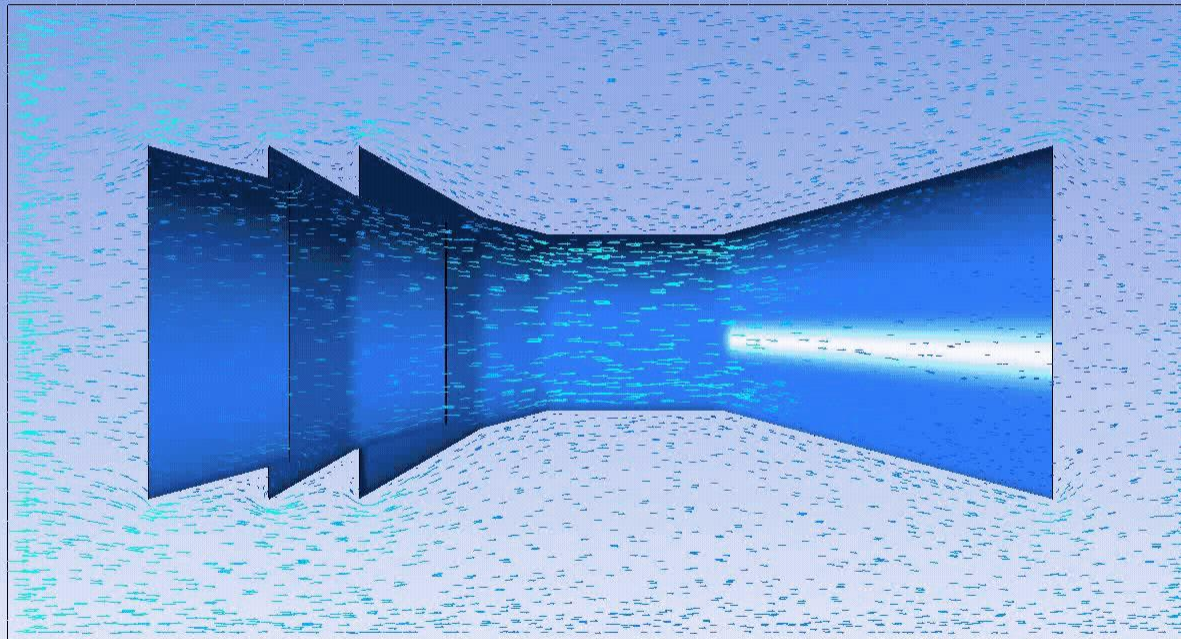
grants to the person(s) having title to this patent the right to exclude others from making, using, offering for sale, or selling the invention throughout the United States of America, and if the invention is a process, of the right to exclude others from using, offering for sale or selling throughout the United States of America, products made by that process, for the term set forth in 35 U.S.C. 154(a)(2) or (c)(1), subject to the payment of maintenance fees as provided by 35 U.S.C. 41(b). See the Maintenance Fee Notice on the inside of the cover.

*Donna H. Hampford*

Performing the Functions and Duties of the Under Secretary of Commerce for Intellectual Property and  
Director of the United States Patent and Trademark Office



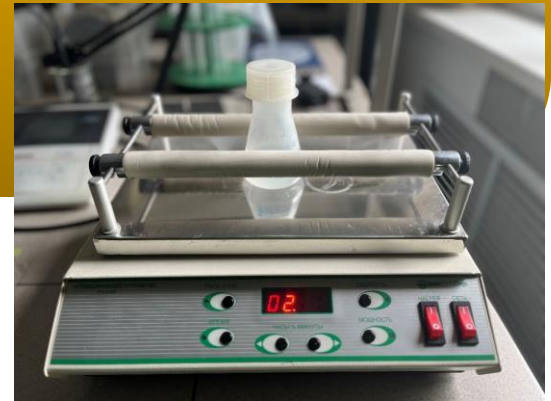
Velocity  
Vector 1  
1.378e+01  
1.033e+01  
6.889e+00  
3.444e+00  
0.000e+00  
[m s<sup>-1</sup>]



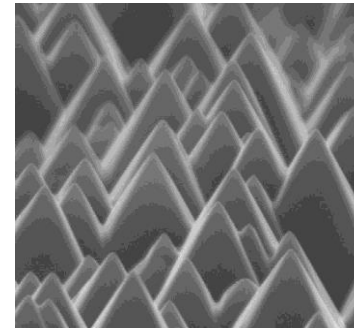
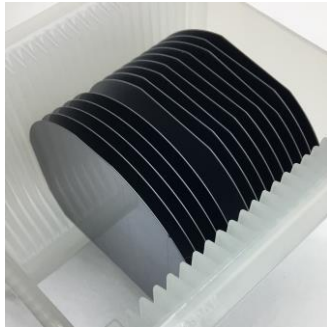
# Solar Energy



The Laboratory of Alternative Energy and Nanotechnology is working on the creation of a safe (sustainable) technology for the production of silicon solar cells. At the moment, the laboratory has achieved success in the formation of p-n junctions by the sol-gel method, passivating coatings by magnetron sputtering, diffusion barriers, etc.

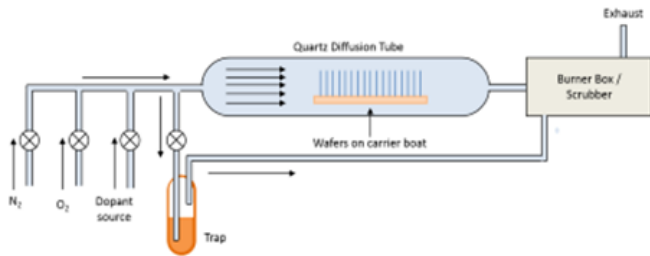


# 1<sup>st</sup> step Test incoming wafer



2<sup>nd</sup> step Saw damage removal and Surface texturization

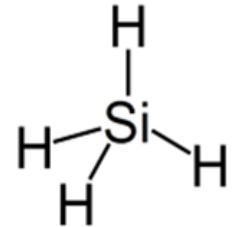
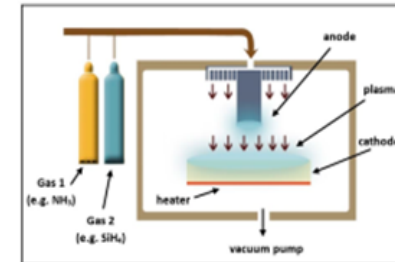
## 3<sup>rd</sup> step POCl<sub>3</sub> Diffusion process



To date, silicon solar cells occupy a major share of the market. However, their production involves several steps using toxic gases.



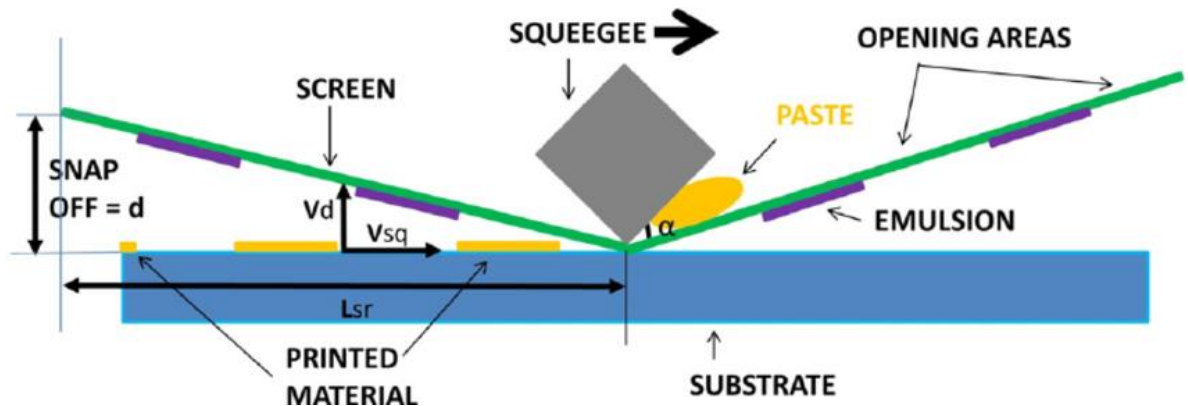
## 4<sup>th</sup> step Surface passivation by PECVD of SiN:H



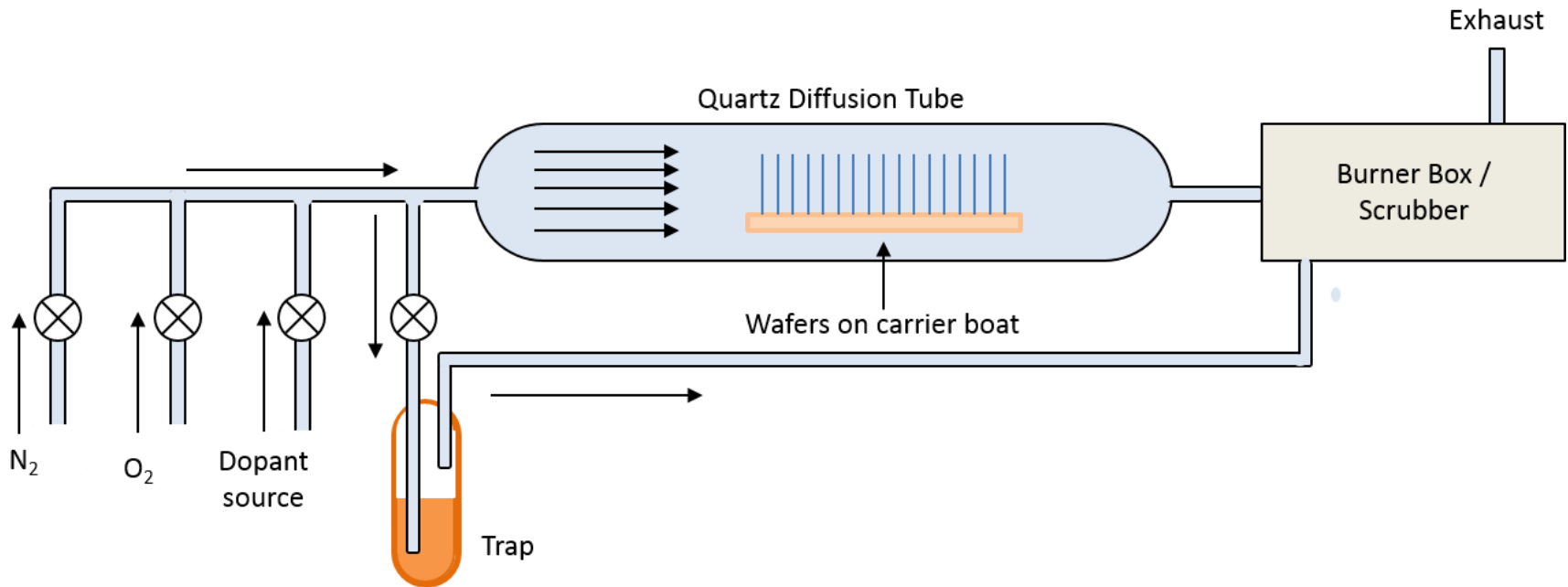
Generally, less than 10% and as little as 3% of the silane that flows through a plasma chamber to deposit the silicon is actually utilized, with the rest remaining unreacted.



5<sup>th</sup> step Front side Ag metallization, Al BSF, and Ag rear busbars. Co-firing of pastes



# 3<sup>rd</sup> step POCl<sub>3</sub> Diffusion process



To date, silicon solar cells occupy a major share of the market. However, their production involves several steps using toxic gases.

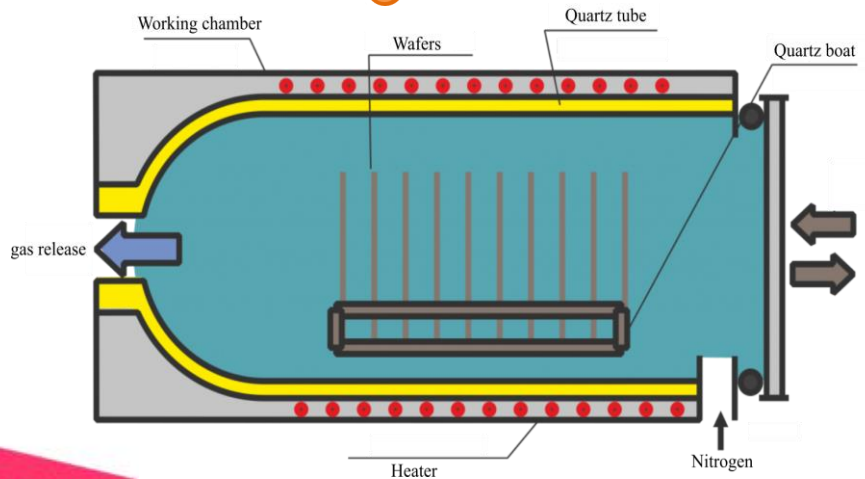
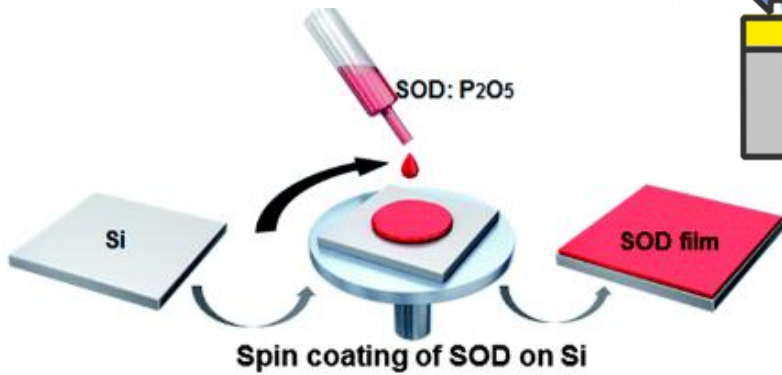
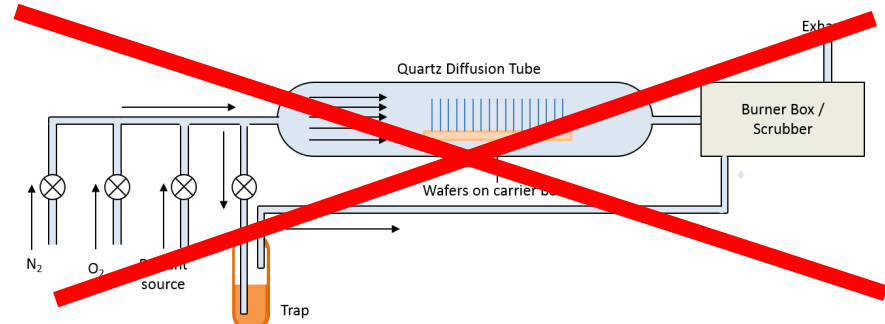


TEOS:H<sub>2</sub>O:C<sub>2</sub>H<sub>5</sub>OH

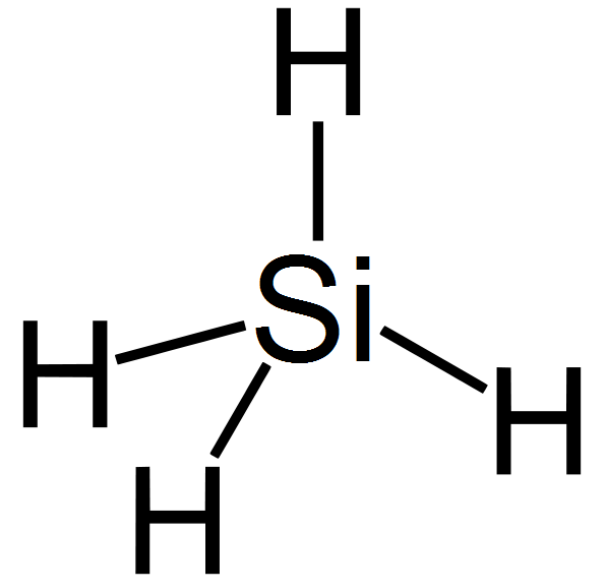
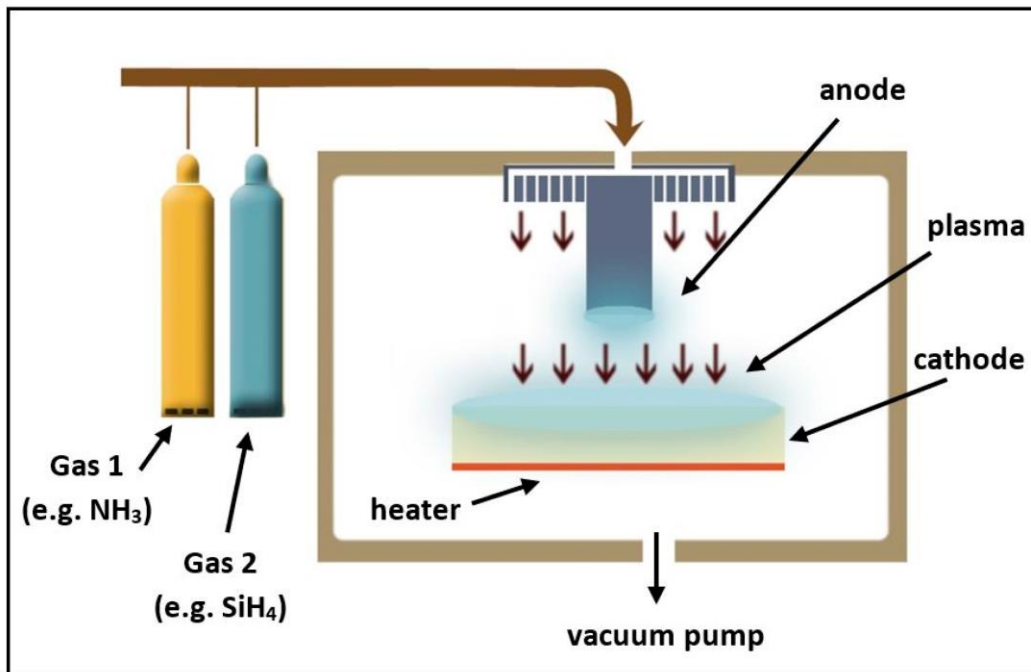
H<sub>3</sub>PO<sub>4</sub> (85%)

Stirring for 1 hour  
70°C

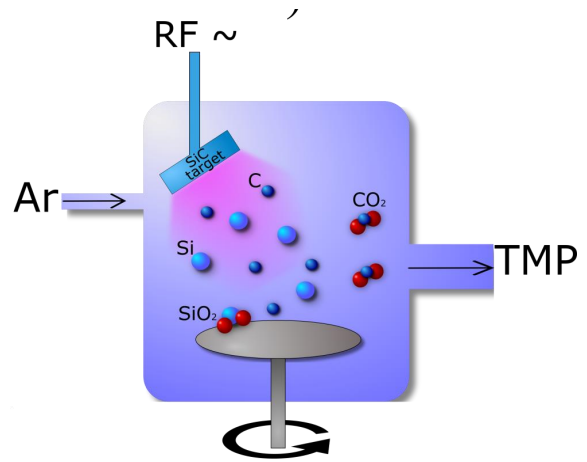
Cooling at RT



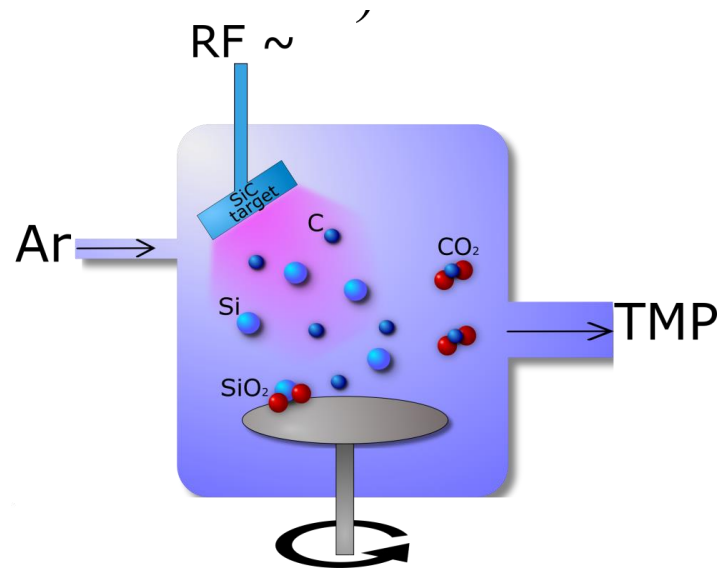
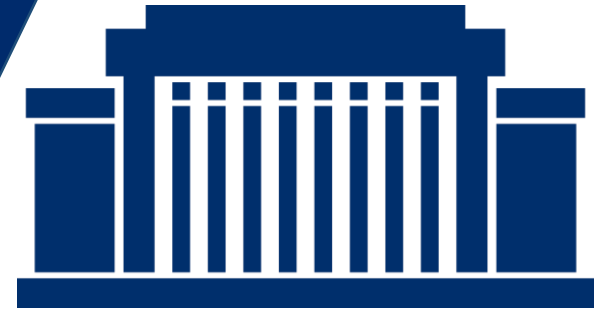
# 4<sup>th</sup> step Surface passivation by PECVD of SiN:H



Generally, less than 10% and as little as 3% of the silane that flows through a plasma chamber to deposit the silicon is actually utilized, with the rest remaining unreacted.



# Safe technology for the production of c-Si solar cells



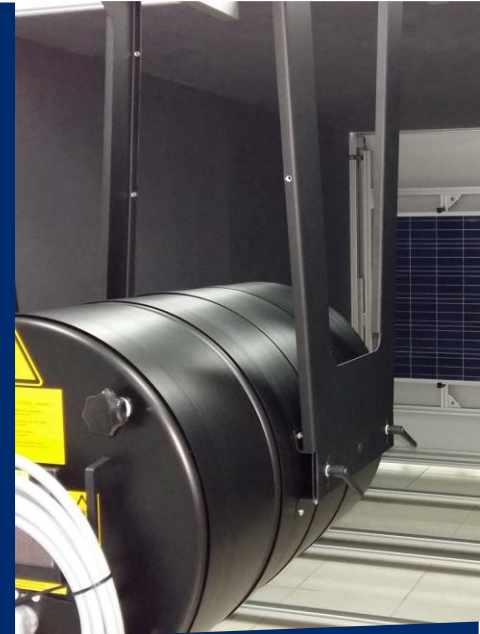
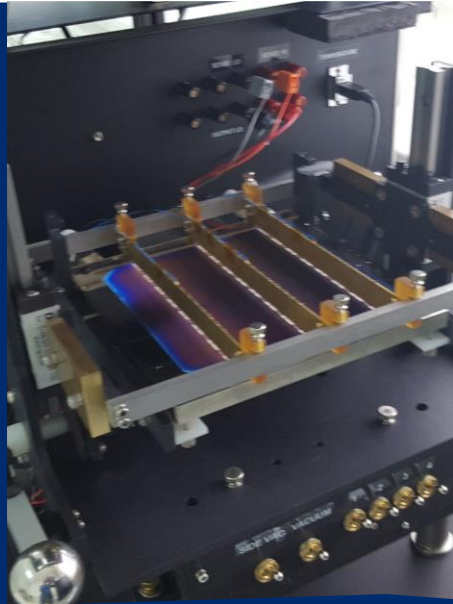
Magnetron sputtering is a deposition technology involving a gaseous plasma which is generated and confined to a space containing the material to be deposited – the ‘target’. The surface of the target is eroded by high-energy ions within the plasma, and the liberated atoms travel through the vacuum environment and deposit onto a substrate to form a thin film.





# LAEaN Equipment





## LAeaN Equipment





# LAEaN Equipment





Inventor, professor Kair Nussupov (the head of laboratory): “In the near future, we will be able to gradually establish this technology in Kazakhstan at a higher level using a low-energy high-current accelerator of heavy ions separated by mass.



Figure 3 – Modernization of a unique accelerator of light and heavy ions, designed to create a p-n-junctions and growing of thick films by ion-beam deposition of low-energy ions. Entered into a preproduction of solar panels.



# Detectors for space and accelerators

Федеральная служба России  
по гидрометеорологии и мониторингу окружающей среды

ГОСУДАРСТВЕННОЕ УЧРЕЖДЕНИЕ  
ИНСТИТУТ ПРИКЛАДНОЙ ГЕОФИЗИКИ  
им. академика Е.К. Федорова (ГУ ИПГ им. академика Е.К. Федорова)  
129128, г. Москва, Ростокинская ул., 9 Для телеграмм: Москва.Земля  
Тел. 181-04-37 Факс 181-81-86

28.02.97г № 01-8/75 На №

И.о. директора Института  
физики высоких энергий  
АН Республики Казахстан  
Ю.А. Еременко

На Ваш запрос направляю Вам Заключение по использованию поставляемых Вами  
ионно-легированных кремниевых полупроводниковых детекторов ядерных частиц,  
разработанных под руководством зав. лабораторией Нусупова Каира Хамзаевича.



Авдюшин С.И.

**ЗАКЛЮЧЕНИЕ**

по использованию детекторов

По результатам, полученным при использовании вышеуказанных детекторов, может  
быть сделано Заключение об отсутствии отказов в работе детекторов при их эксплуатации в  
течение длительного времени (более 20 000 часов) в условиях открытого космоса.

Главный конструктор В.А. Крутов



**(12) United States Patent**  
Nussupov

(10) Patent No.: US 6,414,328 B1  
(45) Date of Patent: Jul. 2, 2002

- (54) METHOD AND APPARATUS FOR THE CONVEYING AND POSITIONING OF ION IMPLANTATION TARGETS
- (76) Inventor: Kair Nussupov, P.O. Box 197, 3089 Brighton 6 St., Brooklyn, NY (US) 11235
- (\* Notice: Subject to any disclaimer, the term of this patent is extended or adjusted under 35 U.S.C. 154(b) by 0 days.
- (21) Appl. No.: 09/434,373  
(22) Filed: Nov. 5, 1999
- (51) Int. CL<sup>7</sup> H01J 37/317  
(52) U.S. CL. 250/492.21; 250/492.2  
(58) Field of Search 250/492.21, 492.3, 250/492.2

FOREIGN PATENT DOCUMENTS

GB 2196176 4/1988  
JP 2-79350 3/1990

\* cited by examiner  
Primary Examiner—John R. Lee  
Assistant Examiner—Anthony Quash  
(74) Attorney, Agent, or Firm—Richard C. Litman

**ABSTRACT**  
(57)  
An economical, high capacity, multi-chamber target presentation unit is used in the ion beam processing of semiconductor wafers in the fabrication of integrated circuits. The multi-chamber target presentation unit comprises a central vacuum chamber where the semiconductor wafers are processed and two symmetrically disposed lateral vacuum chambers wherein one of the lateral vacuum chambers is the loading chamber into which the semiconductor wafers which are mounted on cassettes are loaded, while the other lateral vacuum chamber is the discharge chamber into which the semiconductor wafers are transferred after processing. The cassettes with mounted wafers are conveyed from one vacuum chamber to another by means of several screw conveyors and a looped chain conveyor. The present invention continuously processes large semiconductor wafers both efficiently and economically. The present invention has a large capacity and a high throughput being able to continuously process a large number of semiconductor wafers in a relatively short period of time.

- References Cited**  
U.S. PATENT DOCUMENTS
- |             |         |                 |            |
|-------------|---------|-----------------|------------|
| 4,568,234 A | 2/1986  | Lee et al.      | 414,404    |
| 4,818,326 A | 4/1989  | Liu et al.      | 156,345    |
| 4,928,016 A | 3/1990  | Mori et al.     | 230,440.1  |
| 4,948,979 A | 8/1990  | Musaka et al.   | 250,492.2  |
| 4,973,586 A | 12/1990 | Ray             | 230,492.2  |
| 5,124,557 A | 6/1992  | Aikien          | 250,442.11 |
| 5,380,793 A | 2/1995  | Aikien et al.   | 250,492.21 |
| 6,002,109 A | 12/1999 | Johngard et al. | 219,390    |

16 Claims, 13 Drawing Sheets

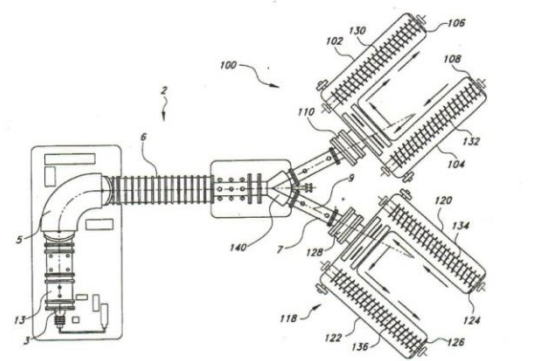


Figure 4 :

- An official letter from Moscow (Russia) regarding the absence of failures of nuclear radiation detectors aboard spacecraft during 20,000 hours.
- US patent on modernization of heavy ion accelerator.
- Copyright certificate on detectors' manufacture.



Figure 5 - Rometer instrument for measuring of electrical resistance and the device taumeter 2M to measure the lifetime of the minority carriers of silicon wafers.

Figure 6 - Upgraded the TM-200-01 MAGNA installation for deposition of nanostructures and diffusion barriers on silicon wafers individually by magnetron sputtering



# High temperature treatment



Figure 7 – Furnaces "Annealing TM-4M" (Russia) for prolonged heat treatment and the passivation of the silicon surface, AS-One 150 (Annealsys, France) for rapid heat treatment of the films and formation of necessary structures and characteristics.

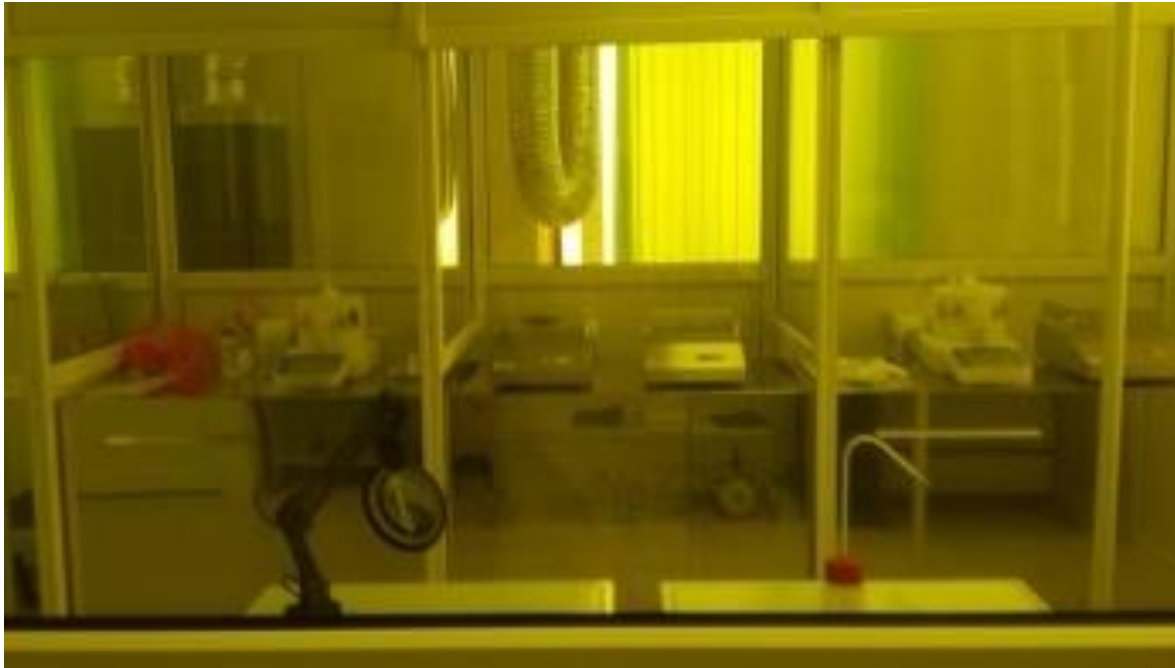


Figure 8 – The clean zone in the photolithography rooms. Automatic installation EM-5006A for two-side contact photolithography for the 150 mm silicon wafers. Installations for deposition, drying and manifestations of photoresist, installation for exposure and alignment in photolithography to form a pattern on the surface of the silicon wafer and to formation of a contact grid.





Figure 9 – Units for liquid chemical treatment in dimethylformamide and Caro mix in clean air with bath for remove of photoresist and DION-A003 for the production of pure water (18 MOm) in photolithographic technology

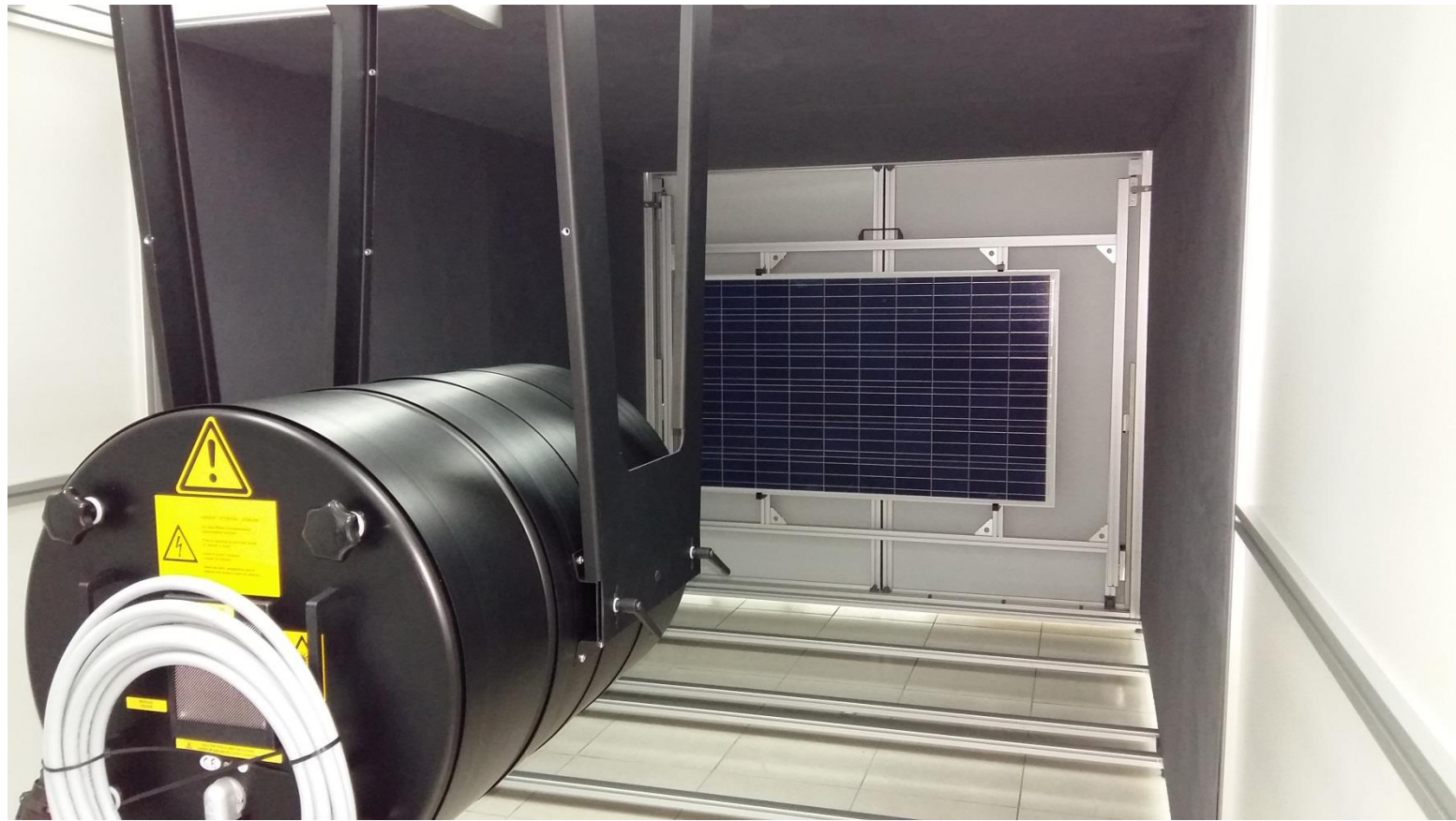


Figure 11 – Installation Pulsed Solar Simulator System (Berger Lichttechnik, Germany) for testing the solar modules.

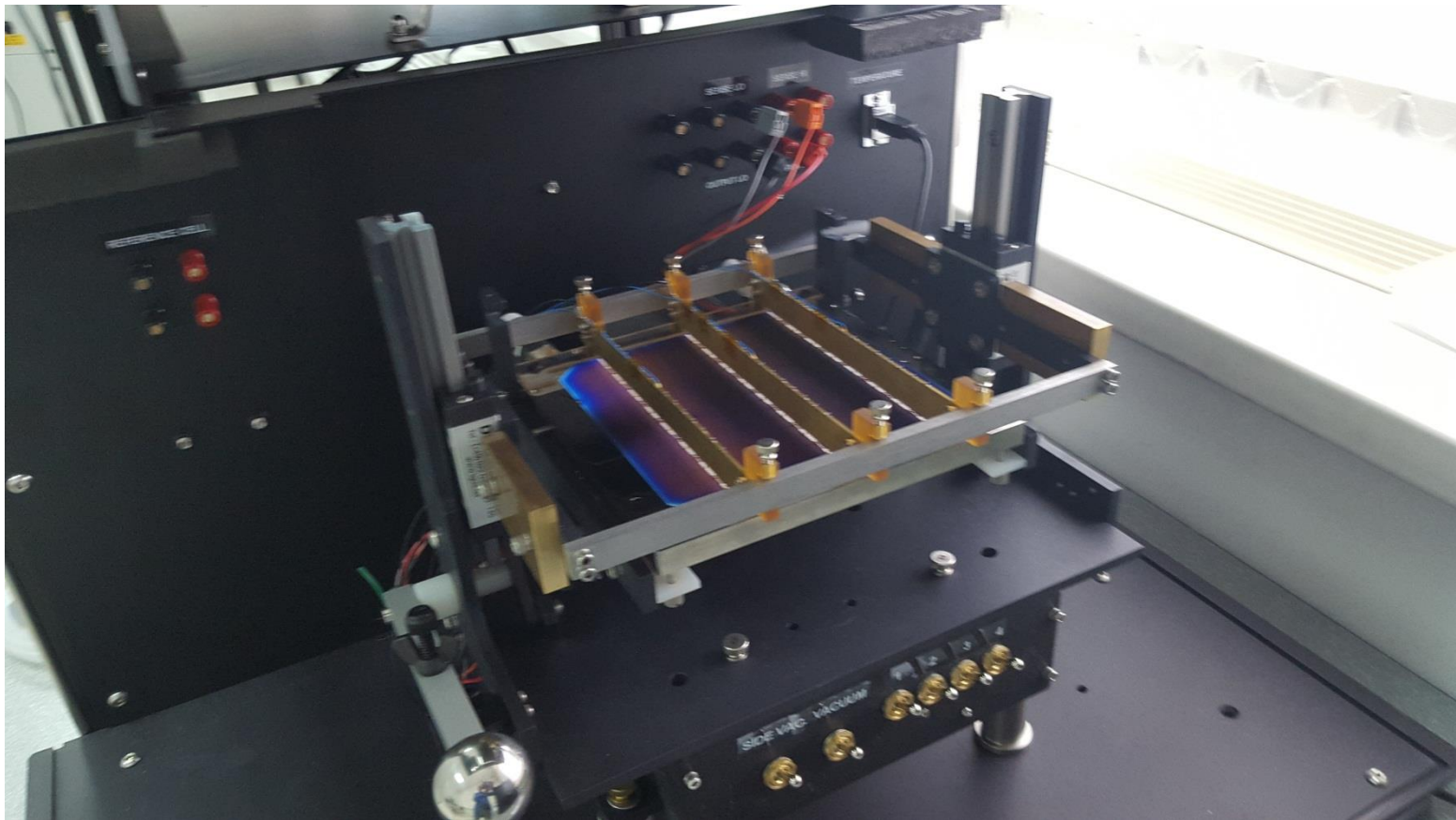


Figure 12 – Installation "Sun 3000" (USA) Solar Simulator for testing the solar cells



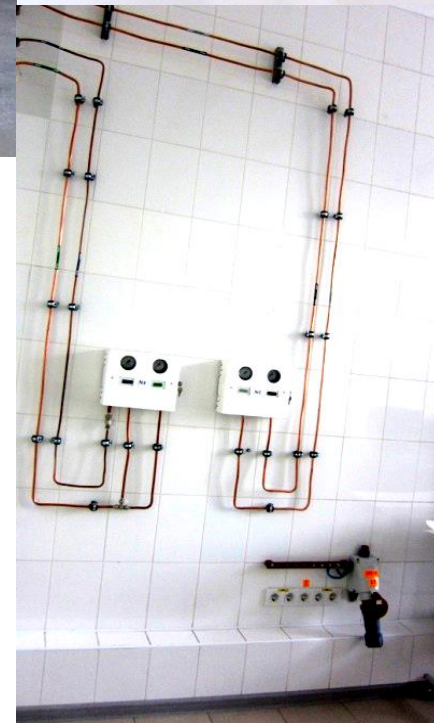


Figure 24 - Gas system and cylinders placed in specially designed cabinets on the territory of Kazakh-British Technical University and the extensive system of delivery of all types of gas in the "clean room"





Figure 20 - Luminous spectrometer Lumina to determine the fluorescent properties of the films in the ultraviolet, visible and near infrared ranges.

Figure 21 - Infrared FTIR spectrometer of the latest model Nicolet iS50 FT-IR with Raman prefix to determine the chemical composition, structure and optical properties of the films

Figure 22 - Spectrophotometer Evolution-300 to measure transparency, reflection and absorption of the films in the ultraviolet, visible and near infrared ranges.

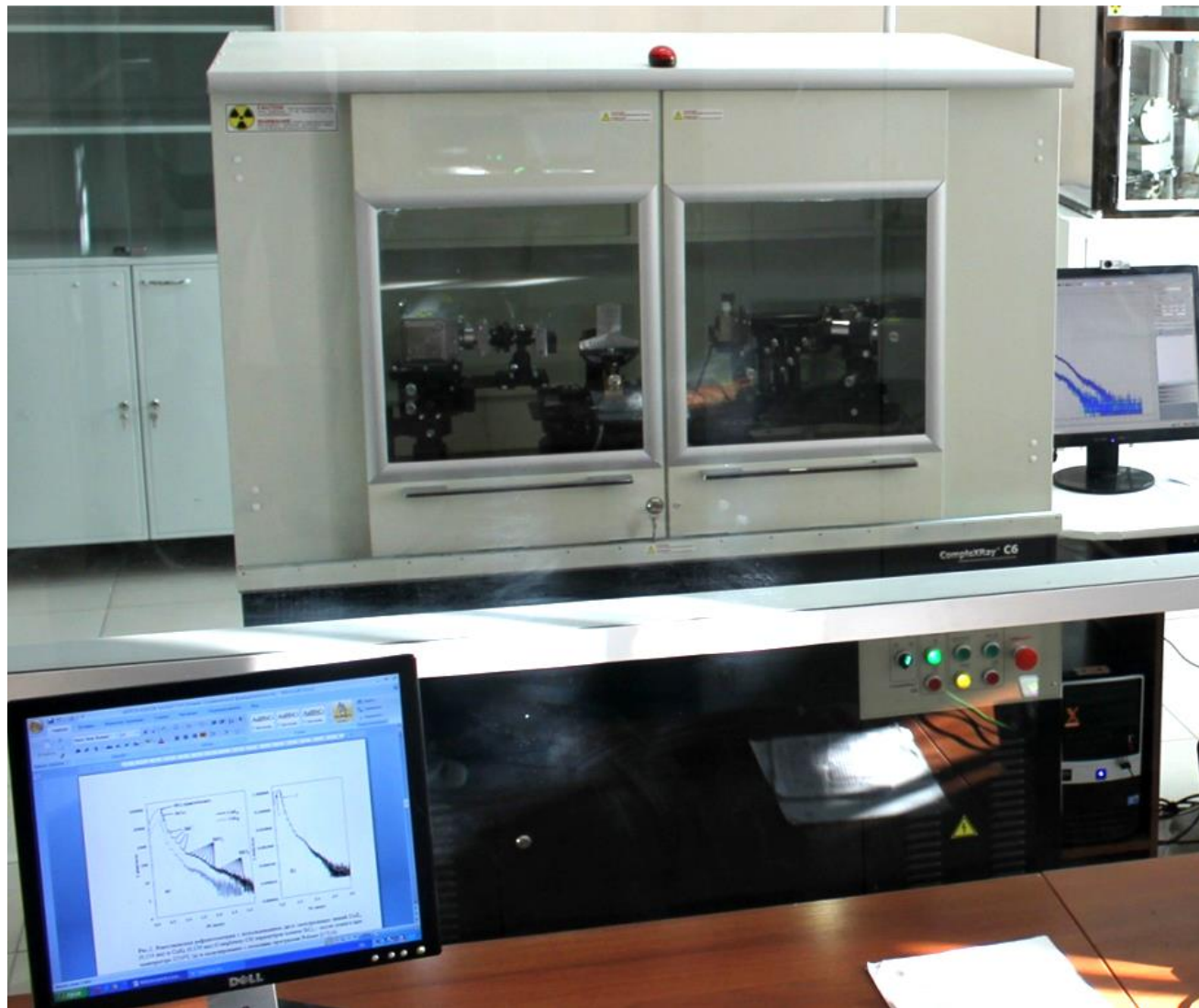


Figure 18 - Modern X-ray reflectometer Complexray C6 to determine the thickness, density and roughness of the films entered into a preproduction of solar cells

Promising application of thin-film technology is the synthesis of SiC, possessing 2 such valuable properties as high hardness ( $33400 \text{ Mn/m}^2$ ), chemical resistance, high melting point ( $2830^\circ\text{C}$ ), wide bandgap ( $2.3\text{--}3.3 \text{ eV}$ ), etc.

Doped with different impurities, silicon carbide is used in semiconductor technology. Field-effect transistors, diodes and other electronic devices based on SiC have several advantages compared to similar silicon devices. Among them, the opportunity to work at temperatures up to  $600^\circ\text{C}$ , high speed and high radiation resistance.

Unfortunately, since it is still difficult to grow SiC material of crystalline quality to meet requirements for a large scale industrial application, small-size and high-cost SiC wafers severely limit their applications at present.

Of particular interest is the synthesis of SiC layers in silicon by ion implantation due to the possibilities to obtain the films of a given thickness and composition, nanolayers of chemical compounds and multilayer structures.

It is of considerable interest to study the effect of the concentration component, nanoclusters, the phase composition of SiC films and their heat or plasma treatment on the crystallization processes and clustering, the size of nanocrystals and, consequently, the physical properties of the films.

The composition and structure of homogeneous  $\text{SiC}_{1.4}$ ,  $\text{SiC}_{0.95}$ ,  $\text{SiC}_{0.7}$ ,  $\text{SiC}_{0.4}$ ,  $\text{SiC}_{0.12}$  and  $\text{SiC}_{0.03}$  layers, received by multiple high-dose implantation of carbon ions with energies of 40, 20, 10, 5 and 3 keV are investigated. The influence of decay of carbon- and carbon-silicon clusters during thermal annealing or hydrogen glow discharge plasma processing on the formation of tetrahedral Si–C-bonds and crystallization processes in silicon layers with high and low concentrations of carbon, is studied.

Single-crystal (100) silicon wafers of sizes  $7 \times 12 \times 0.4 \text{ mm}^3$  with an electrical resistivity 4–5  $\Omega \cdot \text{cm}$  were implanted by  $^{12}\text{C}^+$  ions with energies of 40, 20, 10, 5, and 3 keV at room temperature in vacuum reached by fully oil-free pumping. To prevent sample heating, the ion current density was kept below  $4 \mu\text{A}/\text{cm}^2$ .

The glow discharge hydrogen plasma was generated at a pressure of 6.5 Pa with a capacitive coupled radio frequency (r.f.) power (27.12 MHz) of about 12.5 W. The temperature of processing -  $100^\circ\text{C}$  (5 min).



## 2. Experimental

The SiC<sub>x</sub> films structure was investigated by:

- X-ray diffraction using a narrow collimated ( $0.05 \times 1.5 \text{ mm}^2$ ) monochromatic (CuK<sub>a</sub>) X-ray beam directed at an angle of  $5^\circ$  to the sample surface. The average crystallite size was estimated from the width of X-rays lines by Jones method.
- atomic force microscopy (JSPM 5200, Jeol, Japan) using AFM AC technique;
- transmission electron microscopy (JSPM 5200, Jeol, Japan) using AFM AC technique.
- the IR transmission spectra were recorded in differential regime on double-beam infrared spectrometer UR-20 ( $400\text{--}5000 \text{ cm}^{-1}$ ).
- Auger electron spectroscopy. The parameters were as follows: incident electron beam of diameter  $1 \text{ }\mu\text{m}$ , energy  $10 \text{ keV}$ , angle of incidence  $45^\circ$ , diameter of scanning region  $300 \text{ mm}$ , vacuum  $1.33 \times 10^{-8} \text{ Pa}$ , angle of Ar<sup>+</sup> beam incidence  $45^\circ$ .

Table 1. Values of energy,  $E$ , dose,  $D$ , projected range,  $R_p(E)$ , and straggling,  $\Delta R_p(E)$ , for  $^{12}\text{C}^+$  ions in Si, used for constructing a rectangular distribution profile

<b>E, keV</b>	<b>40</b>	<b>20</b>	<b>10</b>	<b>5</b>	<b>3</b>	
<b>D(SiC<sub>1.0</sub>), 10<sup>17</sup> cm<sup>-2</sup></b>	5,60	1,92	0,990	0,330	<b>0,230</b>	
<b>D(SiC<sub>0.8</sub>), 10<sup>17</sup> cm<sup>-2</sup></b>	4,48	1,54	0,792	0,264	<b>0,184</b>	
<b>D(SiC<sub>0.5</sub>), 10<sup>17</sup> cm<sup>-2</sup></b>	2,80	0,96	0,495	0,165	<b>0,115</b>	
<b>D(SiC<sub>0.3</sub>), 10<sup>17</sup> cm<sup>-2</sup></b>	1,68	0,576	0,297	0,099	<b>0.069</b>	
<b>D(SiC<sub>0.1</sub>), 10<sup>17</sup> cm<sup>-2</sup></b>	0,56	0,192	0,099	0,033	<b>0,023</b>	
<b>D(SiC<sub>0.03</sub>), 10<sup>17</sup> cm<sup>-2</sup></b>	0,168	0,058	0,030	0,010	<b>0,007</b>	
<b>N<sub>C</sub>(Burenkov) profile (Burenkov et al., 1985)</b>	<b>R<sub>p</sub>(E), nm</b>	120,4	60,0	30,3	16,1	<b>10,5</b>
	<b>ΔR<sub>p</sub>(E), nm</b>	46,0	28,3	16,9	10,2	<b>7,2</b>
<b>N<sub>C</sub>(Gibbons) profile (Gibbons et al., 1975)</b>	<b>R<sub>p</sub>(E), nm</b>	93,0	47,0	24,0	12,3	<b>7,5</b>
	<b>ΔR<sub>p</sub>(E), nm</b>	<b>34,0</b>	<b>21,0</b>	<b>13,0</b>	<b>7,00</b>	<b>4,3</b>

Kair Kh. Nussupov and Nurzhan B. Beisenkhanov. The Formation of Silicon Carbide in the SiC<sub>x</sub> Layers (x = 0.03–1.4) Formed by Multiple Implantation of C Ions in Si. // In book: Silicon Carbide - Materials, Processing and Applications in Electronic Devices. Moumita Mukherjee (Ed.). 2011. Chapter 4. *InTech*. PP. 69-114.

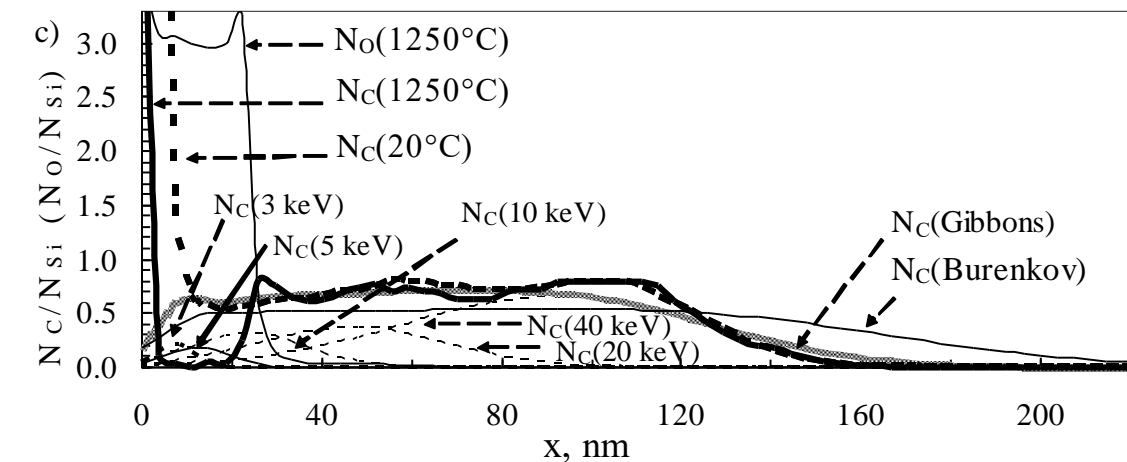
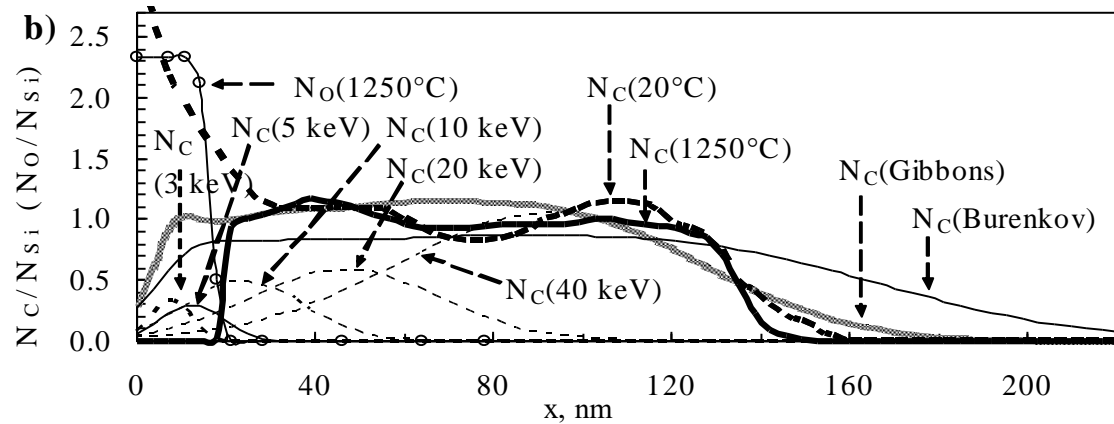
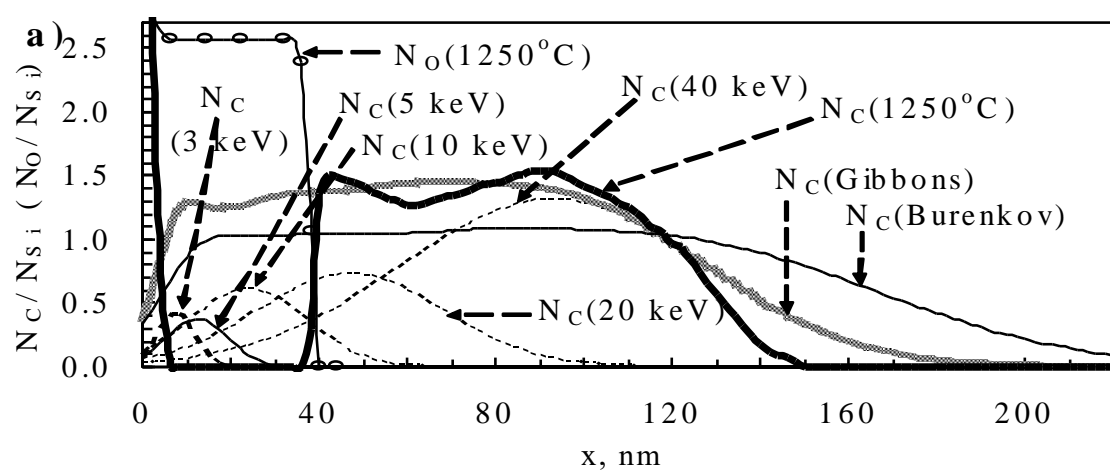
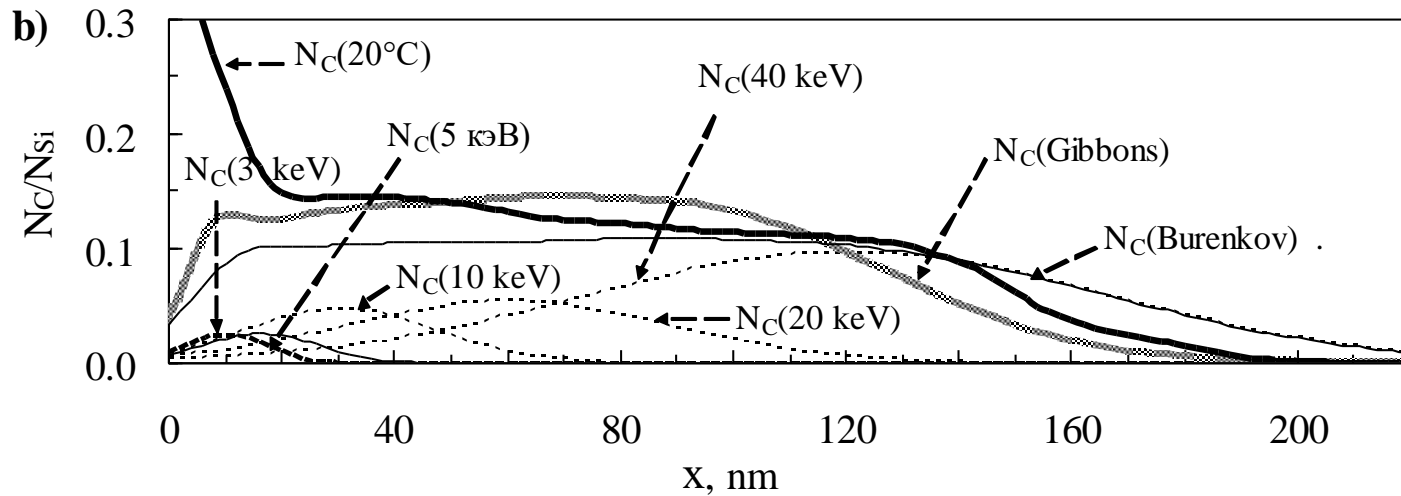
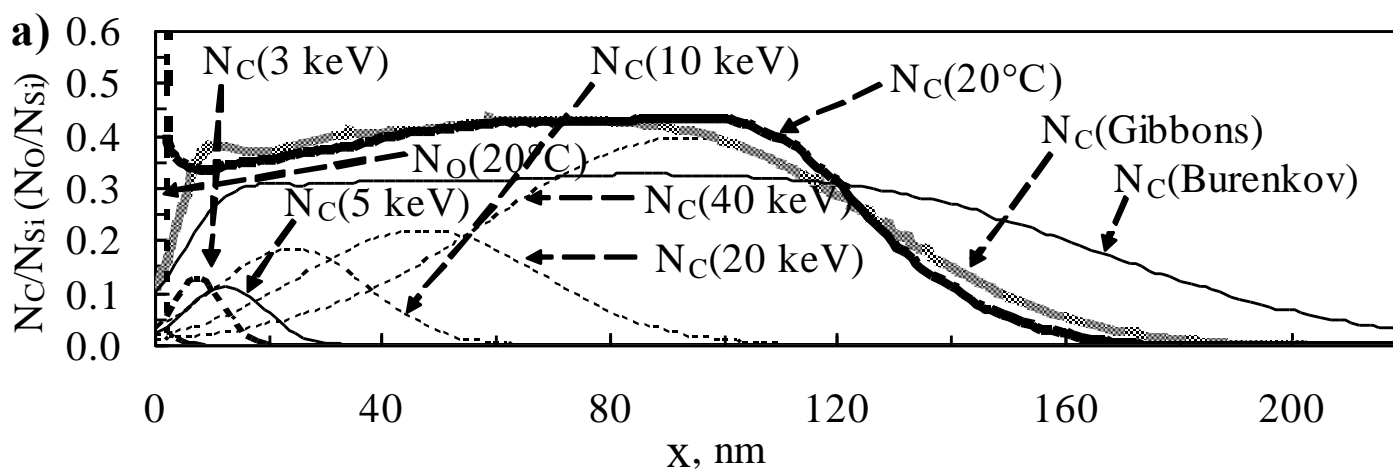


Fig. 1.  $^{12}\text{C}$  distribution profiles in **S4** produced by ion implantation (table 1) (a)  $\text{SiC}_{1.4}$ ; (b)  $\text{SiC}_{0.95}$ ; (c)  $\text{SiC}_{0.7}$ .

$N_{\text{C}}(\text{Burenkov})$  and  $N_{\text{C}}(\text{Gibbons})$  are the profiles calculated according to Burenkov et al. (1985) and Gibbons et al. (1975), respectively, where  $N_{\text{C}}(\text{Gibbons}) = N_{\text{C}}(40 \text{ keV}) + N_{\text{C}}(20 \text{ keV}) + N_{\text{C}}(10 \text{ keV}) + N_{\text{C}}(5 \text{ keV}) + N_{\text{C}}(3 \text{ keV})$ .  $N_{\text{C}}(20^{\circ}\text{C})$ ,  $N_{\text{C}}(1250^{\circ}\text{C})$  and  $N_{\text{O}}(1250^{\circ}\text{C})$  are the Auger profiles of carbon and oxygen, respectively, in a layer after high-dose implantation and annealing at  $T = 1250^{\circ}\text{C}$ , 30 min.



3 Nussupov K.Kh., Sigle V.O. and Bejsenkanov N.B. Investigation of the formation of Si and SiC crystalline phases in room temperature C implanted Si // Nucl. Instrum. and Meth. in Phys.Res. – B82. – 1993. – P.69–79.



**Fig. 2.**  $^{12}\text{C}$  distribution profiles in Si produced by ion implantation (see table 1).  
(a)  $\text{SiC}_{0.4}$ ; (b)  $\text{SiC}_{0.12}$ .

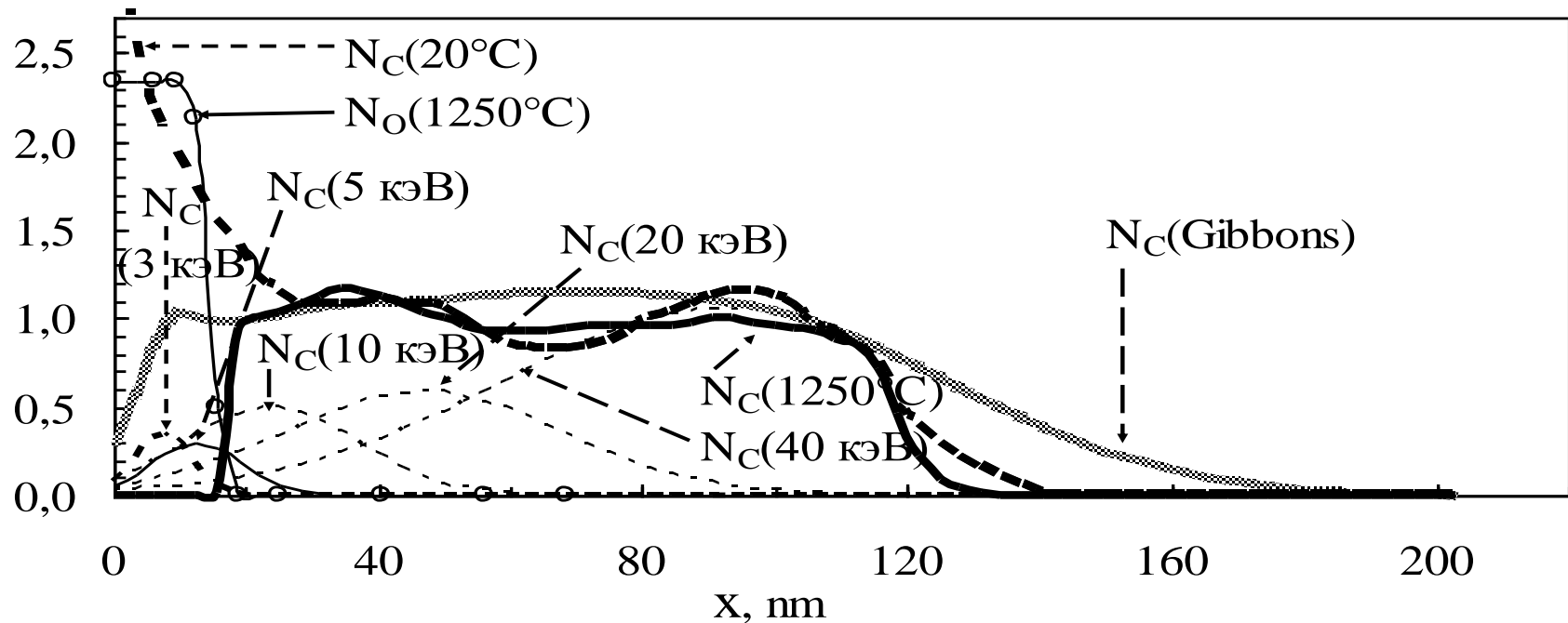
Depth range, nm	40–110	20–110	25–120	10–120	20–120
$\text{SiC}_x$ (Burenkov)	$\text{SiC}_{1.0}$	$\text{SiC}_{0.8}$	$\text{SiC}_{0.5}$	$\text{SiC}_{0.3}$	$\text{SiC}_{0.1}$
$\text{SiC}_x$ (Gibbons)	$\text{SiC}_{1.38}$	$\text{SiC}_{1.06}$	$\text{SiC}_{0.67}$	$\text{SiC}_{0.40}$	$\text{SiC}_{0.13}$
$\text{SiC}_x$ (AES)	$\text{SiC}_{1.4}$	$\text{SiC}_{0.95}$	$\text{SiC}_{0.7}$	$\text{SiC}_{0.4}$	$\text{SiC}_{0.12}$

**Table 2.** Average values of carbon concentration  $x = N_C/N_{\text{Si}}$  in the  $\text{SiC}_x$  layers calculated according Burenkov et al. (1985) and Gibbons et al. (1975) and experimentally obtained by Auger electron spectroscopy



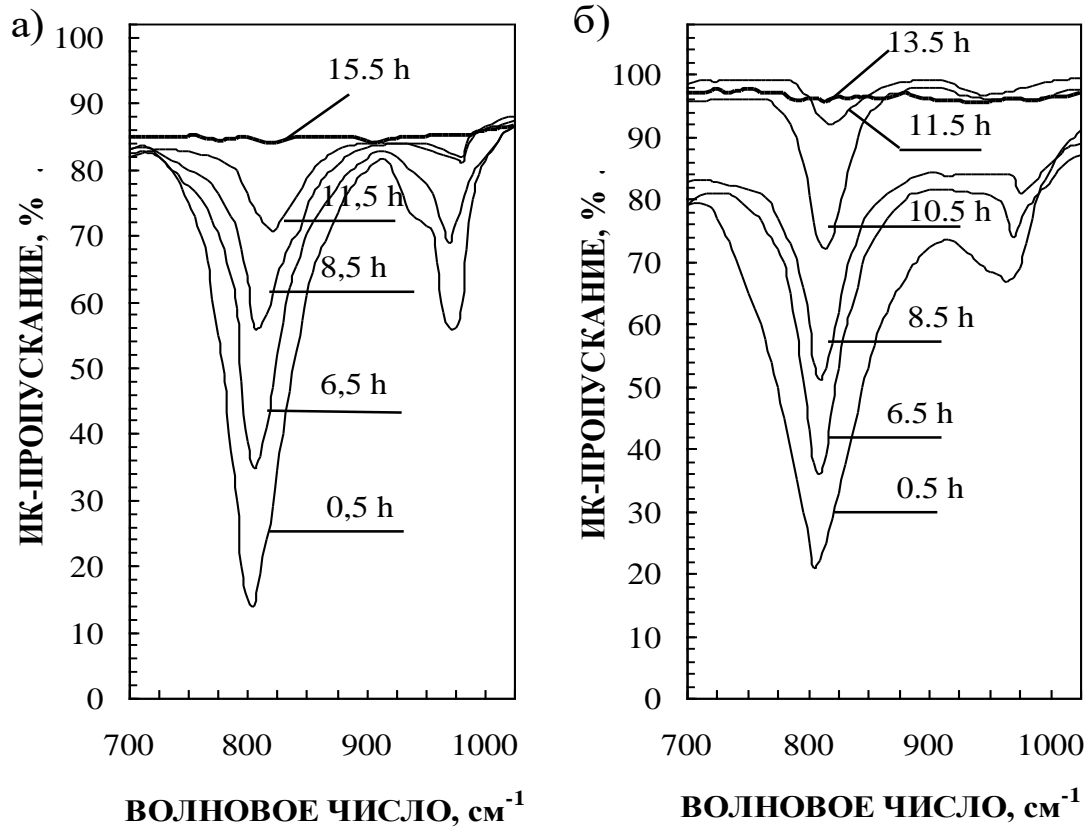
Figure 1b shows that the average concentrations of carbon and oxygen were:  $N_C/N_{Si} = 0.95$  in the depth of the layer from 20 to 110 nm and  $N_O/N_{Si} \approx 2.33$  at the surface of the layer to a depth of almost 20 nm. In this case, penetration of oxygen atoms up to 80 nm deep into the layer is observed. For the  $SiC_{0.95}$  layer, after annealing at  $1250^\circ C$  for 30 minutes, almost 30% of the carbon atoms were desorbed from the film. The “SiC film – Si substrate” boundary in the experiment also turned out to be sharper than the calculated one.

The deformation of the rectangular Auger profile of the distribution of C atoms in Si compared to the calculated profile, manifested in a thinning of the “film-substrate” transition region, an increase in the carbon concentration at the surface and in areas near the maxima of the carbon distribution for individual ion energies, is due to the effects of surface sputtering and changes in composition layer during high-dose implantation of carbon into silicon.



$^{12}C$  distribution profiles in Si:  $N_C(\text{Burenkov})$  and  $N_C(\text{Gibbons})$  are the calculated profiles, where  $N_C(\text{Gibbons}) = N_C(40 \text{ keV}) + N_C(20 \text{ keV}) + N_C(10 \text{ keV}) + N_C(5 \text{ keV}) + N_C(3 \text{ keV})$ .  $N_C(20^\circ C)$ ,  $N_C(1250^\circ C)$  and  $N_O(1250^\circ C)$  are the Auger profiles of carbon and oxygen ( $1250^\circ C$ , 30 min).

After annealing at a temperature of 1200°C for 30 minutes, an intense SiC peak at 800 cm<sup>-1</sup>, corresponding to TO phonons, as well as a SiC peak at 960 cm<sup>-1</sup>, corresponding to LO phonons, is observed in the IR transmission spectra. During long-term high-temperature annealing (1200°C), a gradual decrease in the amplitude of the TO and LO phonon peaks of IR transmission indicates the decomposition of the SiC film structure, i.e. about the instability of these films at high temperatures.



The nature of SiC films formed on substrates with different crystallographic directions is different. It can be seen that the transmission spectra of the vibrational modes (TO- and LO-) of SiC on the Si substrate with the <111> direction are more diffuse and the level of the transmission spectra of two modes superimposed on each other does not allow reaching the initial zero level in the region of the wave number equal to 915 cm<sup>-1</sup>, in contrast to SiC films on a Si substrate with the <100> direction. This is due to the half-width of these peaks.

Dependence of the IR transmission spectra of silicon implanted with <sup>12</sup>C ions on the annealing duration at T = 1200°C: a) n-Si, KEF-4.5, orientation (100); b) p-Si, KDB-10, orientation (111).

## Electron diffraction of the $\text{SiC}_x$ layer

The layers  $\text{SiC}_{1.4}$ ,  $\text{SiC}_{0.95}$  and  $\text{SiC}_{0.7}$  are solid, homogeneous, fine polycrystalline films (Figs. 4a-c, 5a, b and 6a, b, light areas, respectively). Some electron diffraction patterns contain superimposed point (*c*-Si) and ring (SiC) electron diffraction patterns (Fig.4b,c, 5b and 6b). These patterns were recorded from areas 3 where the objects were presented together with single- and polycrystalline structures (for example  $\text{Si}+\text{SiC}_{1.4}$ ). In Figs. 4b, 5b and 6b the microstructure of sections 1 (light area), 2 (intermediate region) and 3 (dark area) are shown.

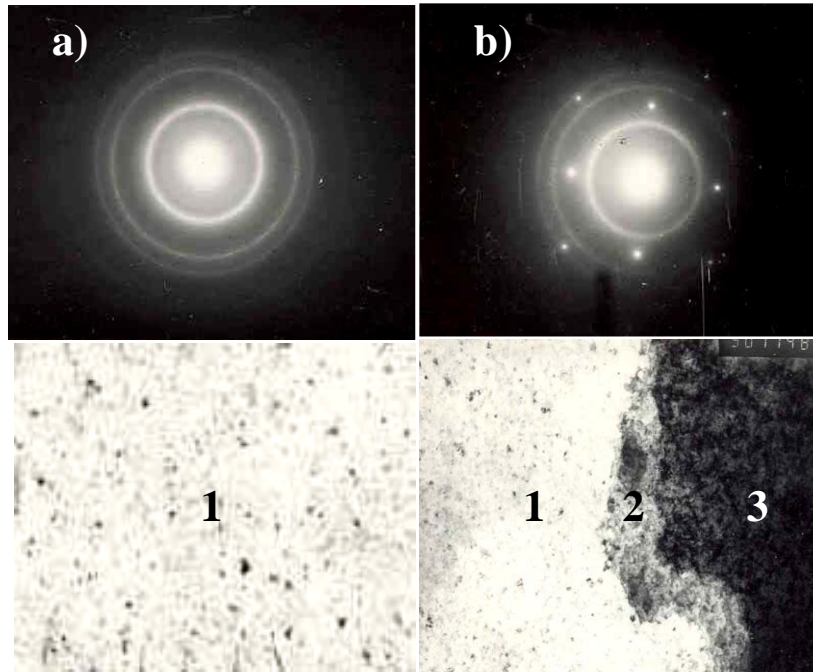


Fig. 4. Electron diffraction patterns and microstructure ( $\times 50000$ ) of the  $\text{SiC}_{1.4}$  layer after annealing at temperature  $1200^\circ\text{C}$  for 30 min: rings – SiC, point reflections – Si, bright regions –  $\text{SiC}_{1.4}$  layer, dark regions – *c*-Si. a)  $\text{SiC}_{1.4}$  region; b)  $\text{SiC}_{1.4}$  regions + intermediate Si–  $\text{SiC}_{1.4}$  layer + *c*-Si: (1)  $\text{SiC}_{1.4}$  regions, (2) regions of an intermediate Si–  $\text{SiC}_{1.4}$  layer, (3) double-diffraction regions.

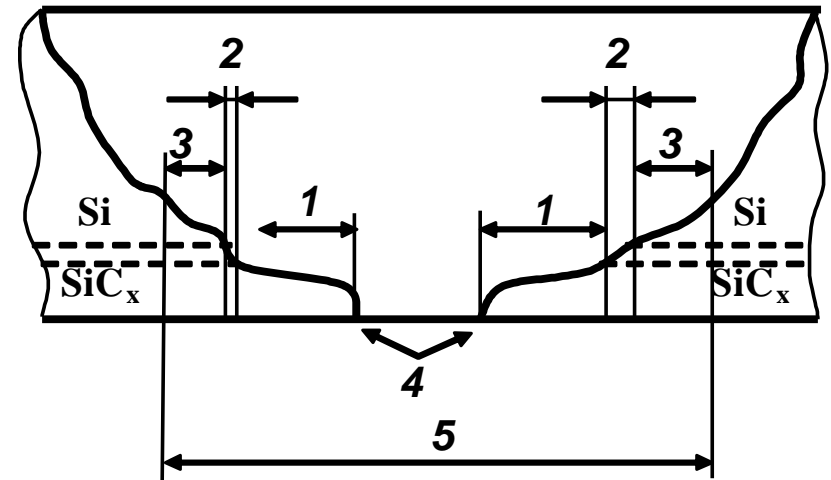


Fig. 3. Schematic cross section of the sample under study: (1)  $\text{SiC}_x$  regions, (2) regions of an intermediate Si–  $\text{SiC}_x$  layer, (3) double-diffraction regions, (4) a through hole, and (5) the area to be analyzed by transmission electron microscopy.

The  $\text{SiC}_x$  layer is a continuous, homogeneous, finely dispersed nanocrystalline film of SiC (a, b, light areas). Transition layer with a lower concentration of carbon between the Si substrate and  $\text{SiC}_{0.7}$  is not uniform. It can be assumed that excess silicon atoms that are between the large SiC grains, in the process of recrystallization are combined with the substrate, forming a sawtooth SiC–Si structure (Fig. 6b).

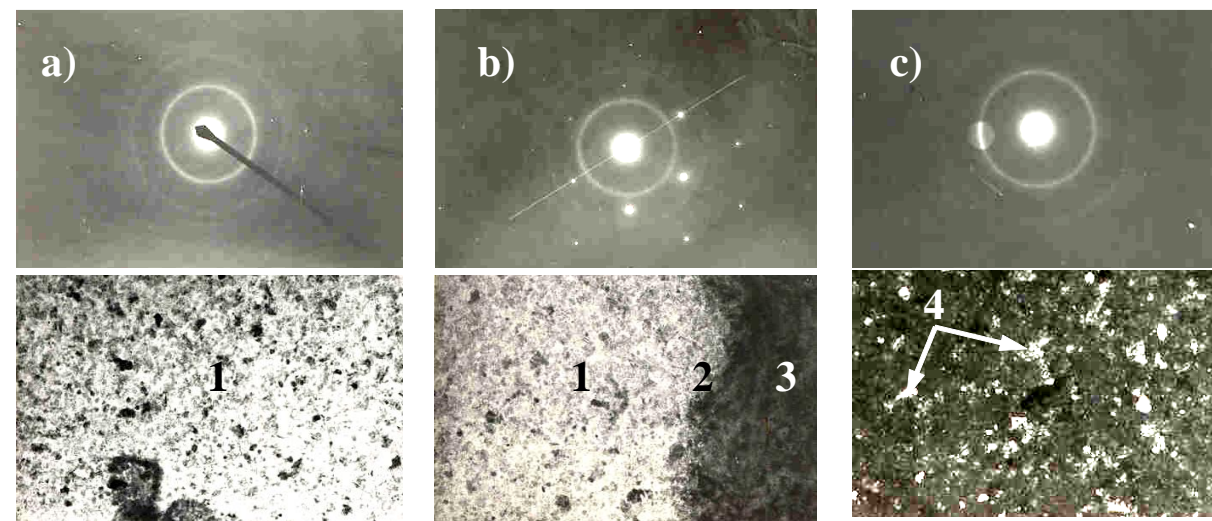


Fig. 5. Electron diffraction patterns and microstructure ( $\times 50000$ ) of the  $\text{SiC}_{0.95}$  layer ( $1200^\circ\text{C}$ , 30 min): rings – SiC, point reflections – Si, bright regions –  $\text{SiC}_{0.95}$  layer, dark regions – c-Si. a)  $\text{SiC}_{0.95}$  region; b)  $\text{SiC}_{0.95}$  regions + intermediate Si– $\text{SiC}_{0.95}$  layer + c-Si, c) SiC crystallites in dark-field image regime: (1)  $\text{SiC}_{0.95}$  regions, (2) regions of an intermediate Si– $\text{SiC}_{0.95}$  layer, (3) double-diffraction regions, (4) SiC crystallites.

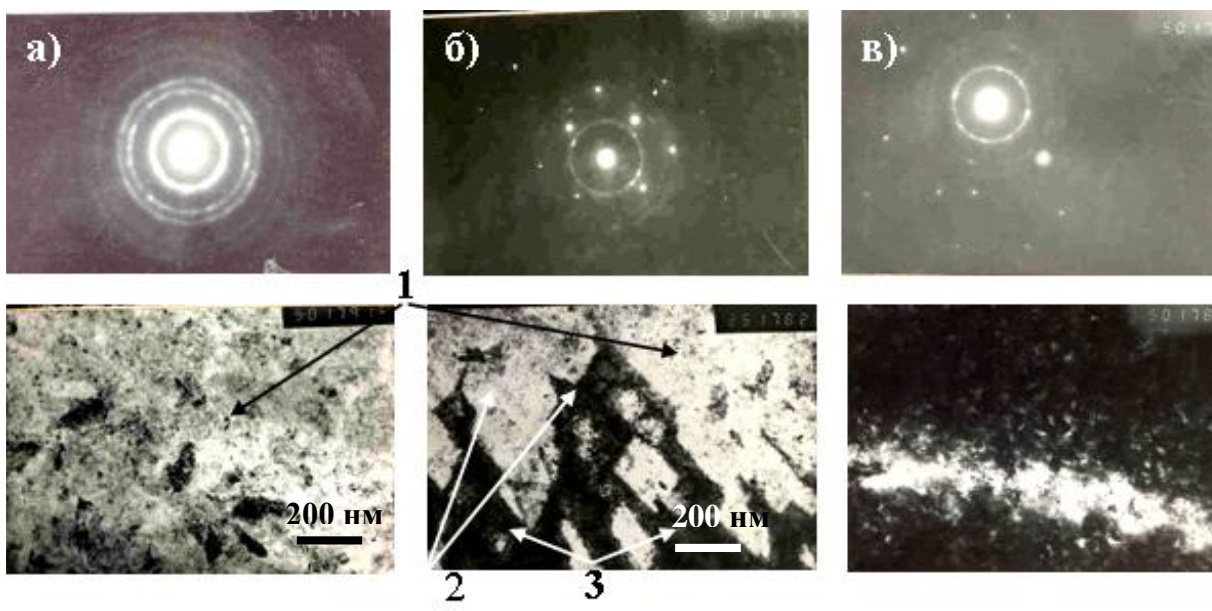


Figure 6 – Electron diffraction patterns and microstructure ( $\times 50000$ ) of the  $\text{SiC}_{0.7}$  layer ( $1200^\circ\text{C}$ , 30 min): rings – SiC, point reflections – Si, bright regions –  $\text{SiC}_{0.7}$  layer, dark regions – c-Si. a)  $\text{SiC}_{0.7}$  region; b)  $\text{SiC}_{0.7}$  regions + intermediate Si– $\text{SiC}_{0.7}$  layer + c-Si, c) SiC crystallites in dark-field image regime: (1)  $\text{SiC}_{0.7}$  regions, (2) regions of an intermediate Si– $\text{SiC}_{0.7}$  layer, (3) double-diffraction regions.



After annealing of the SiC<sub>1.4</sub> layer in vacuum 10<sup>-4</sup> Pa at temperatures 1200 and 1400°C in the X-ray diffraction patterns the intensive lines of polycrystalline silicon carbide are observed (Fig. 7a, b). There are also 2 weak lines of polycrystalline silicon, apparently, from the transition layer “Si–SiC<sub>1.4</sub>”, where presents excess silicon, forming in the annealing process the Si crystallites. The intensity of SiC lines after annealing at 1400°C was significantly lower than after annealing at 1200°C, may be due to evaporation of silicon at high temperatures (Semenov et al., 2009). The processing by glow discharge hydrogen plasma (27.12 MHz, 12.5 W, 6.5 Pa, 100°C) for 5 min led to the complete disintegration of silicon crystallites.

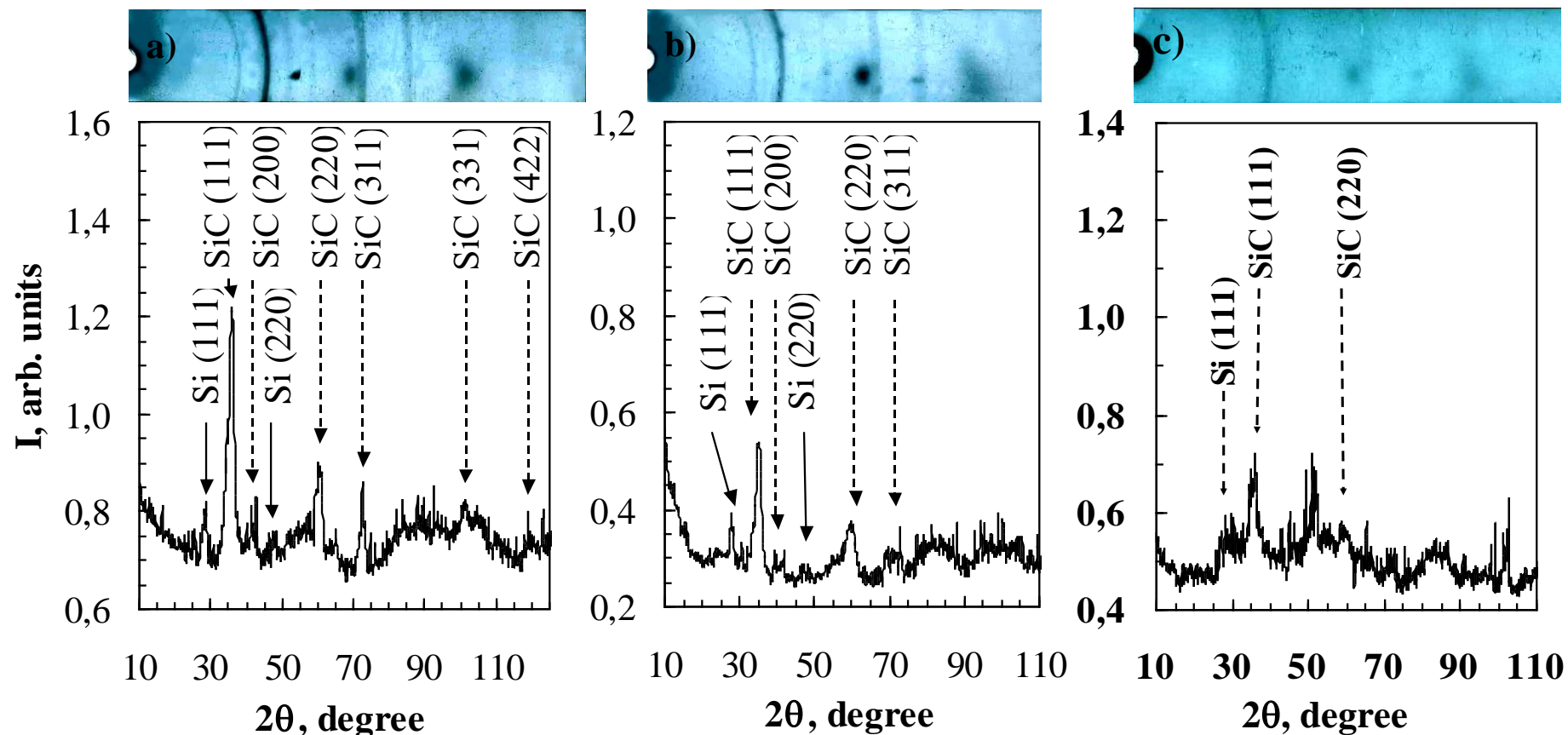
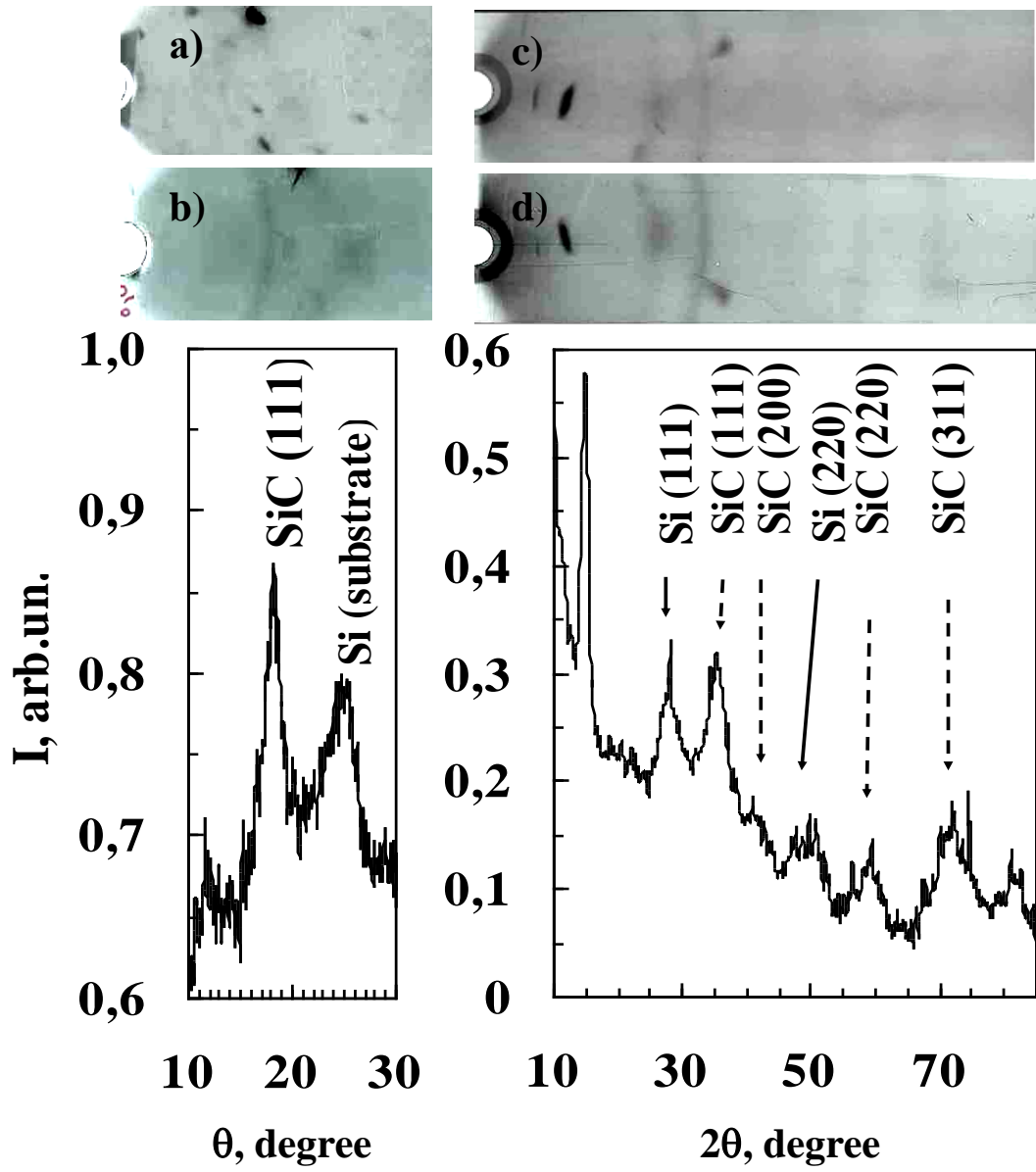


Fig. 7. X-ray diffraction patterns of the SiC<sub>1.4</sub> layer annealed for 30 min at (a) 1200°C, (b) 1400°C, (c) after annealing at 1400°C and processing by glow discharge hydrogen plasma for 5 min.



After annealing of the  $\text{SiC}_{0.95}$  layer at 1100°C and below (Fig. 8a) not seen any lines of polycrystalline phases. A weak line of  $\beta\text{-SiC}(111)$  becomes more pronounced after annealing at 1250°C (Fig. 8b).

The diffraction pattern of the  $\text{SiC}_{0.7}$  layer (Fig. 8c) demonstrates the presence of  $\beta\text{-SiC}(111)$  line and weak  $\text{Si}(111)$  line after annealing at 1000°C for 30 min due to the decrease of the concentration of stable carbon clusters. Annealing at 1100°C led to an increase in the intensity of the  $\beta\text{-SiC}(111)$  and  $\text{Si}(111)$  lines (Fig. 8d) and to an appearance of  $\beta\text{-SiC}(200)$ ,  $\beta\text{-SiC}(220)$ ,  $\beta\text{-SiC}(311)$  and  $\text{Si}(220)$  lines, which indicates an improvement in the crystallite structure and a preferred content of polycrystalline  $\beta\text{-SiC}$  phase in comparison with the poly-Si content, which is caused by a relatively high concentration of carbon.

Fig. 8. X-ray diffraction patterns of the  $\text{SiC}_{0.95}$  layer annealed at (a) 1100°C, (b) 1250°C and of the  $\text{SiC}_{0.7}$  layer annealed at (c) 1000°C, (d) 1100°C, for 30 min obtained using X-ray chambers RKD (a, b) and RKU-114M1 (c, d). Intensity curves correspond to X-ray patterns (b, d).

In the layer  $\text{SiC}_{0.4}$  the presence of polycrystalline phases of SiC and Si after implantation and annealing at 1000, 1100 and 1250°C are revealed. High intensity peaks of SiC after annealing at 1100°C (Fig. 9a) indicates on intensive process of crystallization of  $\beta$ -SiC due to lower content of stable clusters in comparison with the layers  $\text{SiC}_{1.4}$ ,  $\text{SiC}_{0.95}$  and  $\text{SiC}_{0.7}$ . High amplitude of  $\beta$ -SiC peaks after annealing at 1250°C confirms this assertion.

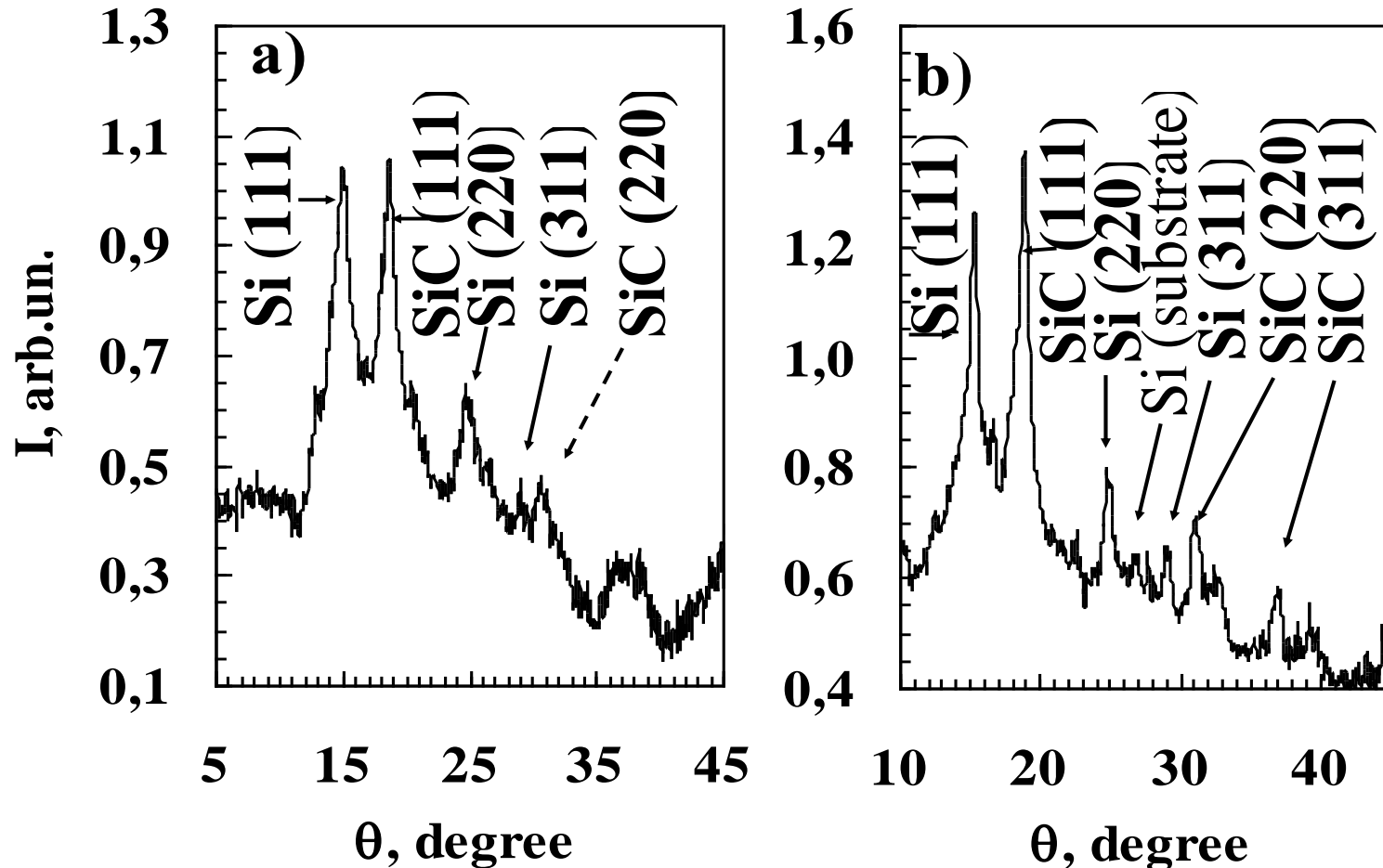


Fig. 9. X-ray diffraction patterns of the  $\text{SiC}_{0.4}$  layer annealed for 30 min at (a) 1100°C and (b) 1250°C.

In diffraction pattern of  $\text{SiC}_{0.12}$  layer after implantation a broad diffuse line of amorphous silicon  $\text{Si}(111)$  ( $\theta = 14.3^\circ$ ) is observed (Fig.10a). After annealing at  $800^\circ\text{C}$  a narrowing of this line, at  $900^\circ\text{C}$  - a sharp narrowing of the line  $\text{Si}(111)$  and the appearance of  $\text{Si}(220)$  and  $\text{Si}(311)$  lines of polycrystalline Si phase, as well as two weak lines of  $\beta\text{-SiC}$ , at  $1250^\circ\text{C}$  - a decrease of the integrated intensity of Si lines, are observed.

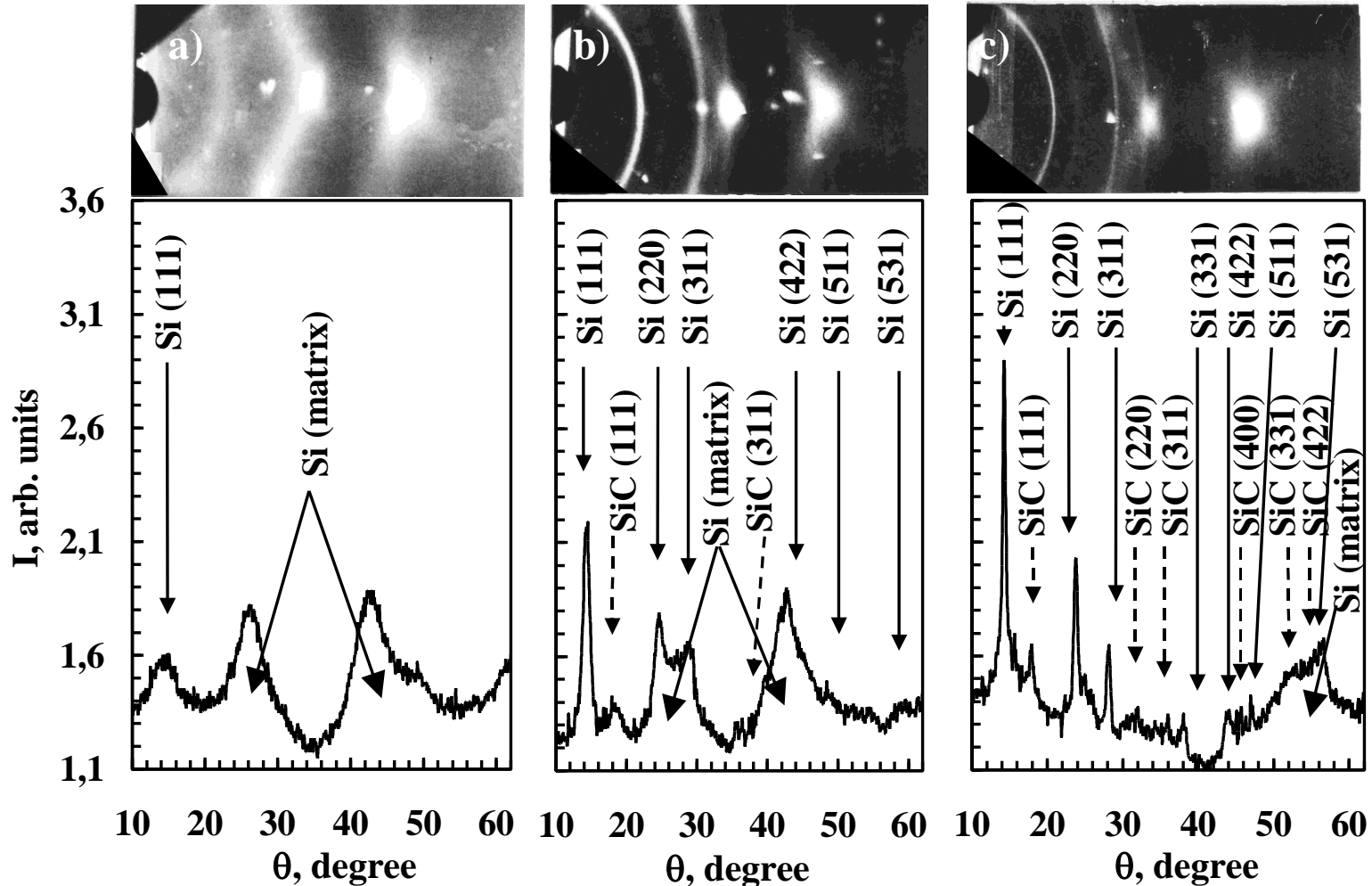


Fig. 10. X-ray diffraction patterns of the  $\text{SiC}_{0.12}$  layer (a) before and after annealing for 30 min at (b)  $1100^\circ\text{C}$  and (c)  $1250^\circ\text{C}$ .



The implantation of carbon causes the formation of weakly ordered set of randomly oriented Si<sup>7</sup> regions of size ~1.5 nm. Temperature dependence of the average crystallite size Si (Fig. 11a, curve 1) and SiC (curve 2) in plane (111) shows that at low temperatures the curve 1 is characterized by slow growth in the size of weakly ordered Si nanocrystals. Their transformation into well ordered Si crystallites at 800°C is taken place. Average size of Si crystallites is 47 nm after annealing at 1250°C. The formation of β-SiC crystallites prevent a complete recrystallization of layer at this temperature.

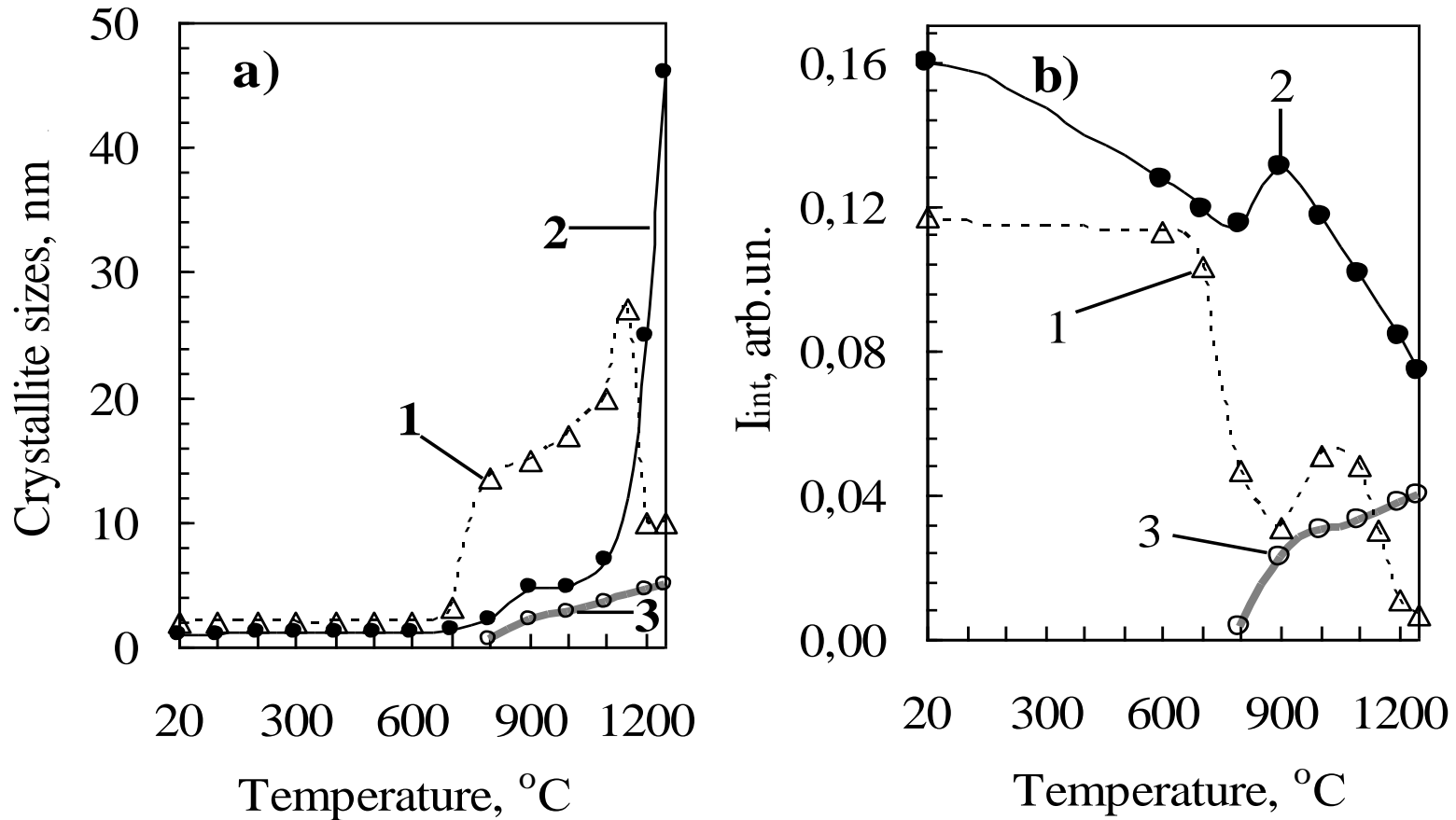


Fig. 11. Average sizes (a) of Si and SiC crystallites in the (111) plane and (b) the integrated intensities of the Si(111) and SiC(111) lines after implantation of carbon ions in silicon and annealing. 1 – Si (for layer SiC<sub>0.03</sub>), 2 – Si (for layer SiC<sub>0.12</sub>), 3 – SiC (for layer SiC<sub>0.12</sub>).

The integrated intensity curve of Si(111) line, which is proportional to the phase volume, has three sections in the temperature ranges of 20–800°C, 800–900°C and 900–1250°C (Fig. 11b).

In the range of 20–800°C  $I_{\text{int}}$  decreases, indicating a decrease in the total volume of nanocrystals Si, although their sizes increase up to 2.2 nm. The growth of weak ordered Si crystallites is accompanied by the displacement of carbon atoms in the surrounding space, which no longer contribute to the intensity of the Si(111) line due to increased concentration of carbon.

In addition, there is recrystallization of silicon near the substrate. It is assumed that, after annealing at 800°C (Figs. 11b and 12) approximately  $k_{800} \approx [I_{\text{int}}(800^\circ\text{C})/I_{\text{int}}(20^\circ\text{C})] \times 100\% = 72\%$  of silicon atoms in the layer is incorporated into crystallites of Si. The remaining atoms of Si (28%) are in an amorphous mixture of Si and C atoms, or reunited with the substrate.

Figure 6 – Electron diffraction patterns and microstructure ( $\times 50000$ ) of the  $\text{SiC}_{0.7}$  layer ( $1200^\circ\text{C}$ , 30 min): rings – SiC, point reflections – Si, bright regions –  $\text{SiC}_{0.7}$  layer, dark regions – c-Si

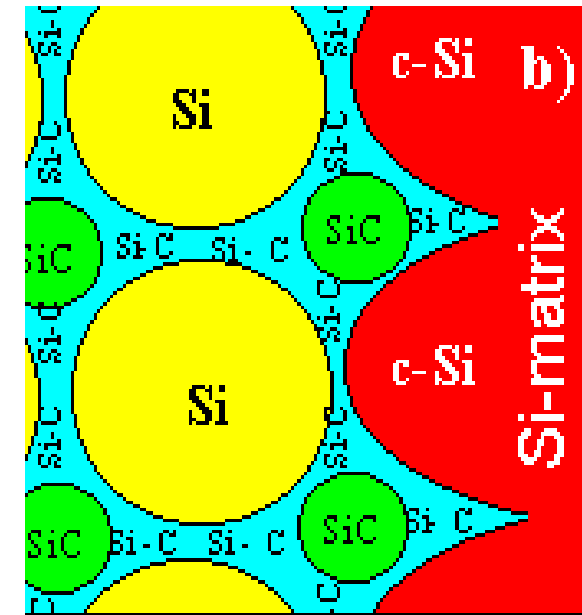
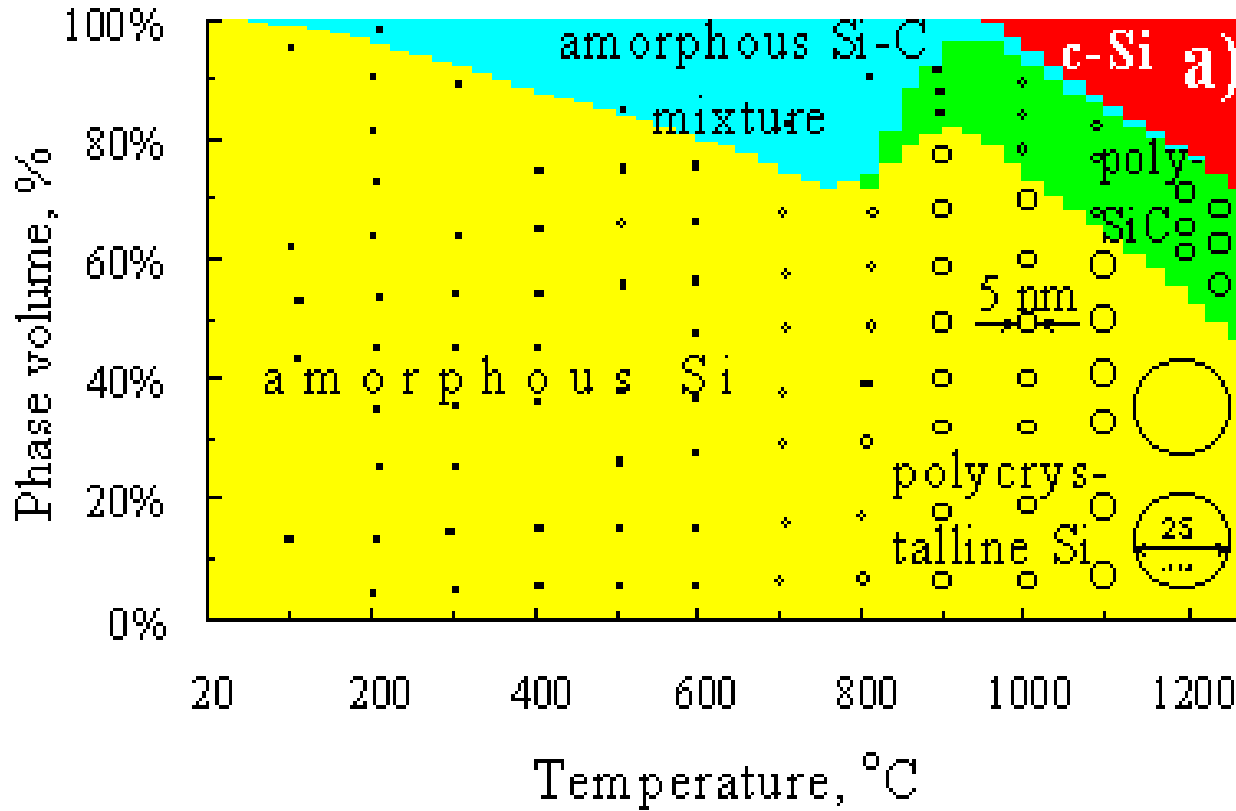
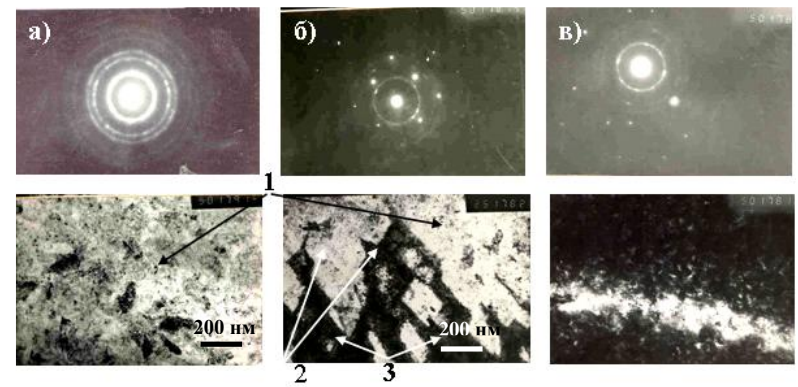


Fig. 12. Crystallization of the  $\text{SiC}_{0.12}$  layer: (a) the phase volumes at various annealing temperatures and (b) the formation of crystalline Si and SiC crystallites in the temperature range  $900\text{--}1000^\circ\text{C}$ .

Fig. 12 schematically shows the variation of the structure of the layer, its phase composition and phase volume, as well as the average grain size as a function of annealing temperature (a) and scheme of Si and SiC crystallite formation in this layer (b). The diagram is based on the curves in Fig. 11a, b for  $\text{SiC}_{0.12}$ .

"amorphous Si-C mixture" + "c-Si" = 100% – ("poly-SiC" + "poly-Si" + "amorphous -Si").

In the range of 800–900°C the increase in both size crystallites Si (from 2.2 to 4.7 nm) and the volume of polycrystalline phase of Si (Fig. 11a and 12) is observed. This is due to the formation of SiC crystallites at 900°C in the regions of carbon accumulation and the joining of excess silicon atoms to Si crystallites. So,  $k$  is increased:  $k_{900} \approx 82\%$ . This leads to a decrease in Si–C-mixture volume (Fig. 12).

After annealing at 1000°C and 1250°C, an increase in the phase volume and crystallite sizes of  $\beta$ -SiC as well as a decrease in  $k$  due to recrystallization of regions near the Si substrate, are taken place:  $k_{1000} \approx 73\%$  and  $k_{1250} \approx 46\%$ . Si crystallite sizes increased almost 10 times (up to 47 nm).

Probably, there is destruction of defective silicon crystallites and the uniting of their atoms into crystallites with a perfect structure or with the substrate. As can be seen from the diagram, after annealing at 1200°C in the layer  $\text{SiC}_{0.12}$  ~50% of silicon atoms are incorporated into Si crystallites with an average size of 25 nm, 25% of Si atoms is included into  $\beta$ -SiC crystallite with size of 5 nm and 25% is joined with Si substrate. Since the unit cell volume for Si is twice more than the cell volume for SiC, the volume of the surface layer of Si after implantation and annealing of carbon should not change appreciably, and the above relations can be regarded as a volume ratio of phases.



During annealing at 1400°C there is the destruction of most of the silicon crystallites and connection of their atoms to the substrate. The intensity of the lines Si was significantly lower than the intensities of  $\beta$ -SiC lines (Fig. 13). It is assumed that recrystallized Si layer with ingrained in him crystallites of  $\beta$ -SiC and Si on a silicon substrate was obtained.

The X-ray diffraction results are in accordance with the data of Auger electron spectroscopy, whereby the concentration of carbon atoms in a layer is  $N_C/N_{Si} = 0.12/1$  (Fig. 2). Then the maximum possible ratio of atoms, forming part of SiC and Si, will be:  $N_{SiC}/N_{Si} = 0.24/0.88 = 0.27$ . As seen in Figure 11b, the maximum quantity of poly-SiC, obtained at 1250°C, was  $I_{int}(SiC) = 0.040$ , and poly-Si was  $I_{int}(Si) = 0.131$  at 900°C, i.e.,  $I_{int}(SiC)/I_{int}(Si) = 0.040/0.131 = 0.30$ , which is comparable with the data of Auger electron spectroscopy.

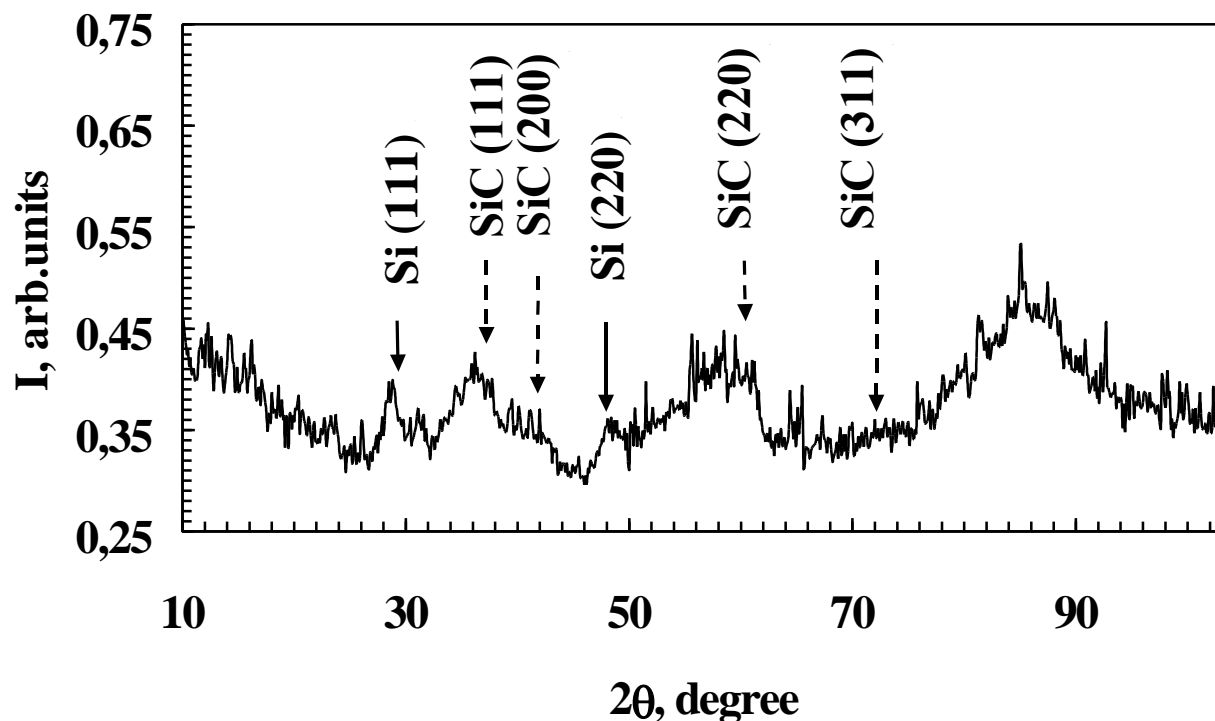
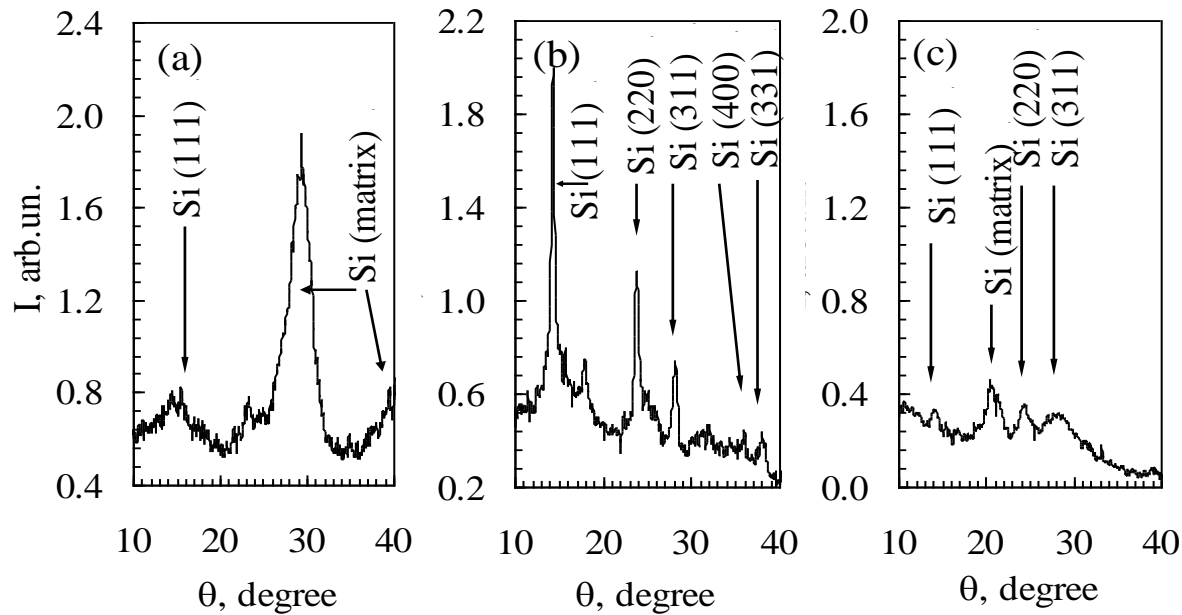


Fig. 13. X-ray diffraction pattern of the  $SiC_{0.12}$  layer after annealing at 1400°C for 30 min.



**Fig. 14.** X-ray diffraction of  $\text{SiC}_{0.03}$  layer after implantation of carbon ions in Si (a) and annealing at  $1100^\circ\text{C}$  (b) and  $1200^\circ\text{C}$  (c) for 30 min.

In  $\text{SiC}_{0.03}$  layer, immediately after the implantation the same broad diffuse line of amorphous silicon  $\text{Si}(111)$  at  $\theta = 14.3^\circ$  is observed (Fig. 14).

Increase of annealing temperature above  $800^\circ\text{C}$  causes narrowing of this line, increasing the number and amplitude of the line intensity which reaches it's maximum at  $1100^\circ\text{C}$ .

In  $\text{SiC}_{0.03}$  layer no lines of polycrystalline silicon carbide in the whole temperature range are observed due to insufficient concentration of the carbon atoms.

Annealing at temperatures above  $1100^\circ\text{C}$  reduces the intensity of Si lines and results their disappearance after annealing at  $1250^\circ\text{C}$  due to recrystallization of the layer.

Temperature ( $^\circ\text{C}$ )	$\varepsilon$ (nm)					
	$\text{SiC}_{0.03}$		$\text{SiC}_{0.12}$		$\text{SiC}_{0.4}$	
	Si	$\beta$ -SiC	Si	$\beta$ -SiC	Si	$\beta$ -SiC
20	2	—	1.1	—	—	—
700	3	—	1.3	—	—	—
800	13	—	2	—	—	—
900	15	—	4.5	2	—	—
1000	17	—	5	3	4	3
1100	20	—	7	3.5	4	3
1150	27	—	12	4	—	—
1200	10	—	25	4.5	—	—
1250	10	—	46	5	9	4.5

**Table 3.** Average size ( $\varepsilon$ ) of Si- and  $\beta$ -SiC crystallites in  $\text{SiC}_x$  layers

In  $\text{SiC}_{0.03}$  layer, immediately after the implantation the same broad diffuse line of amorphous silicon  $\text{Si}(111)$  at  $\theta = 14.3^\circ$  is observed (Fig. 14).

Polycrystalline silicon - increase of annealing temperature above  $800^\circ\text{C}$  causes narrowing of this line, increasing the number and amplitude of the line intensity which reaches it's maximum at  $1100^\circ\text{C}$ .

In  $\text{SiC}_{0.03}$  layer no lines of polycrystalline silicon carbide in the whole temperature range are observed due to insufficient concentration of the carbon atoms.

Annealing at temperatures above  $1100^\circ\text{C}$  reduces the intensity of Si lines and results their disappearance after annealing at  $1250^\circ\text{C}$  due to recrystallization of the layer.

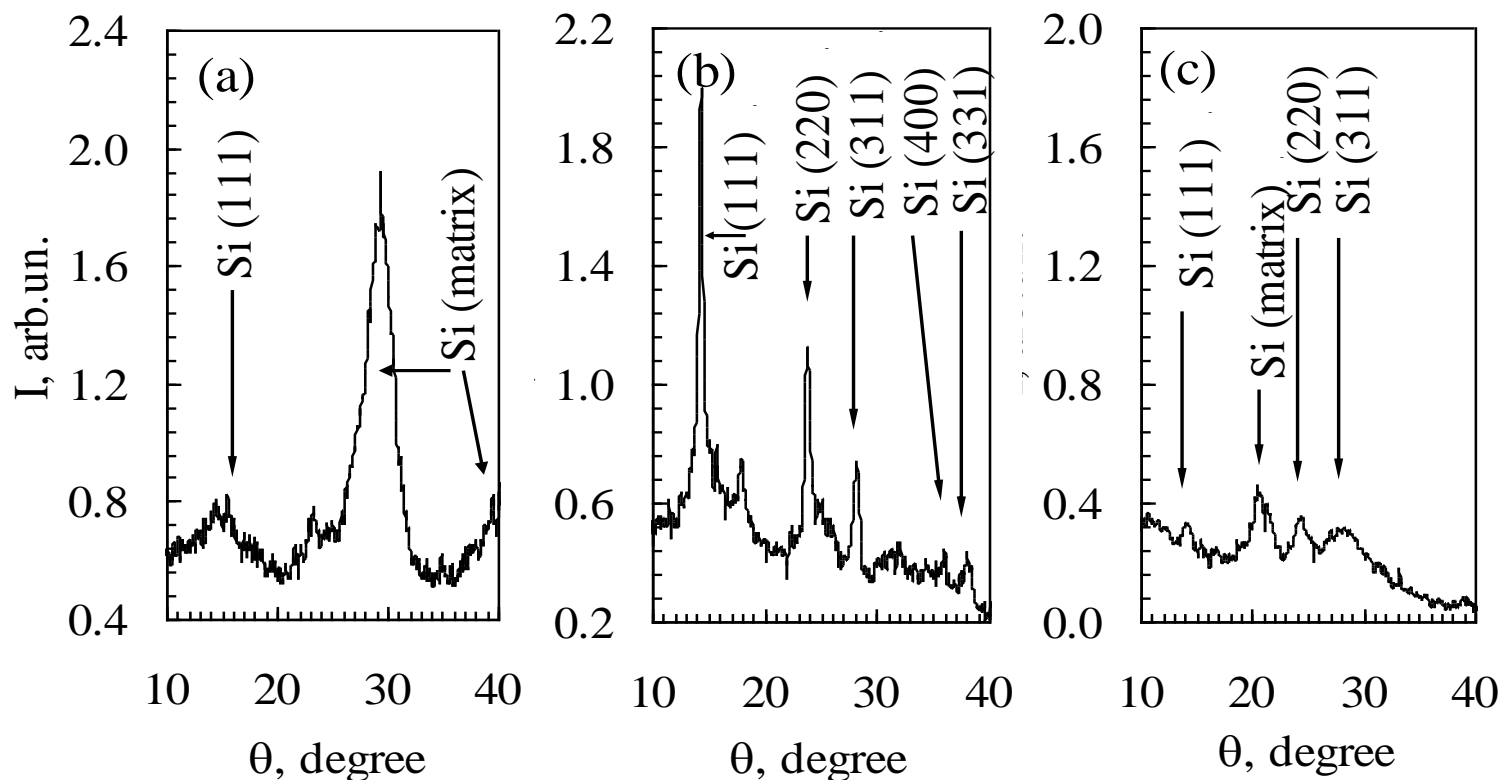


**Fig. 14.** X-ray diffraction of  $\text{SiC}_{0.03}$  layer after implantation of carbon ions in Si (a) and annealing at  $1100^\circ\text{C}$  (b) and  $1200^\circ\text{C}$  (c) for 30 min.

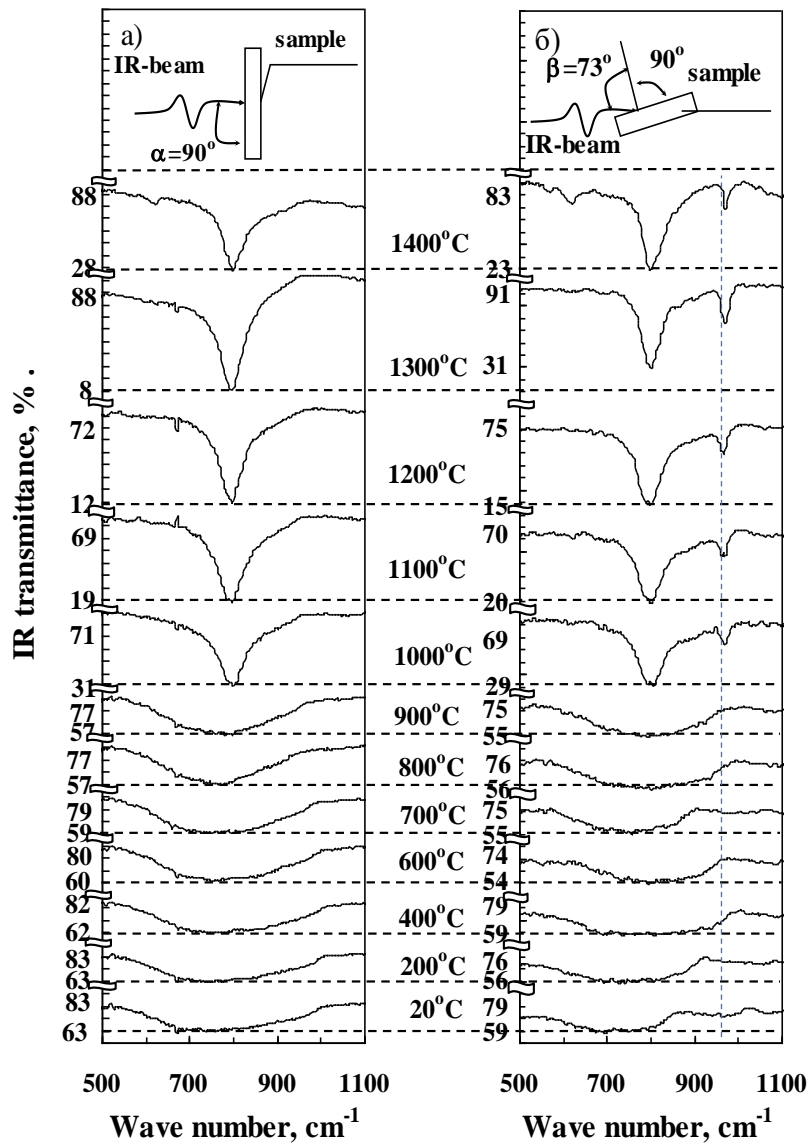


Fig. 18. IR transmission spectra of the SiC<sub>0.7</sub> layer recorded (a) under normal incidence of IR radiation on the sample and (b) at an angle of 73° to the normal to the sample surface.

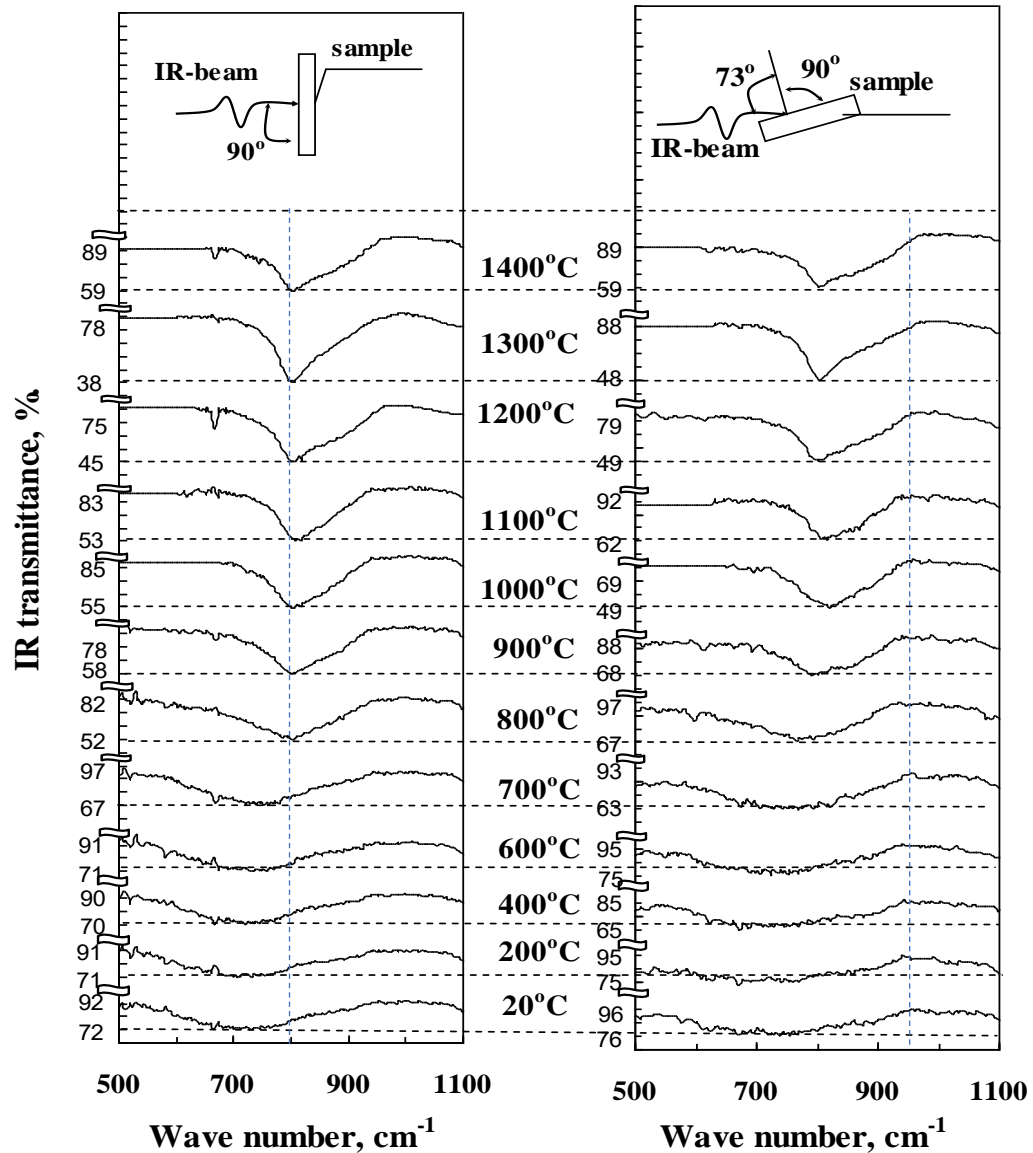


Fig. 19. IR transmission spectra of the SiC<sub>0.4</sub> layer recorded (a) under normal incidence of IR radiation on the sample and (b) at an angle of 73° to the normal to the sample surface.



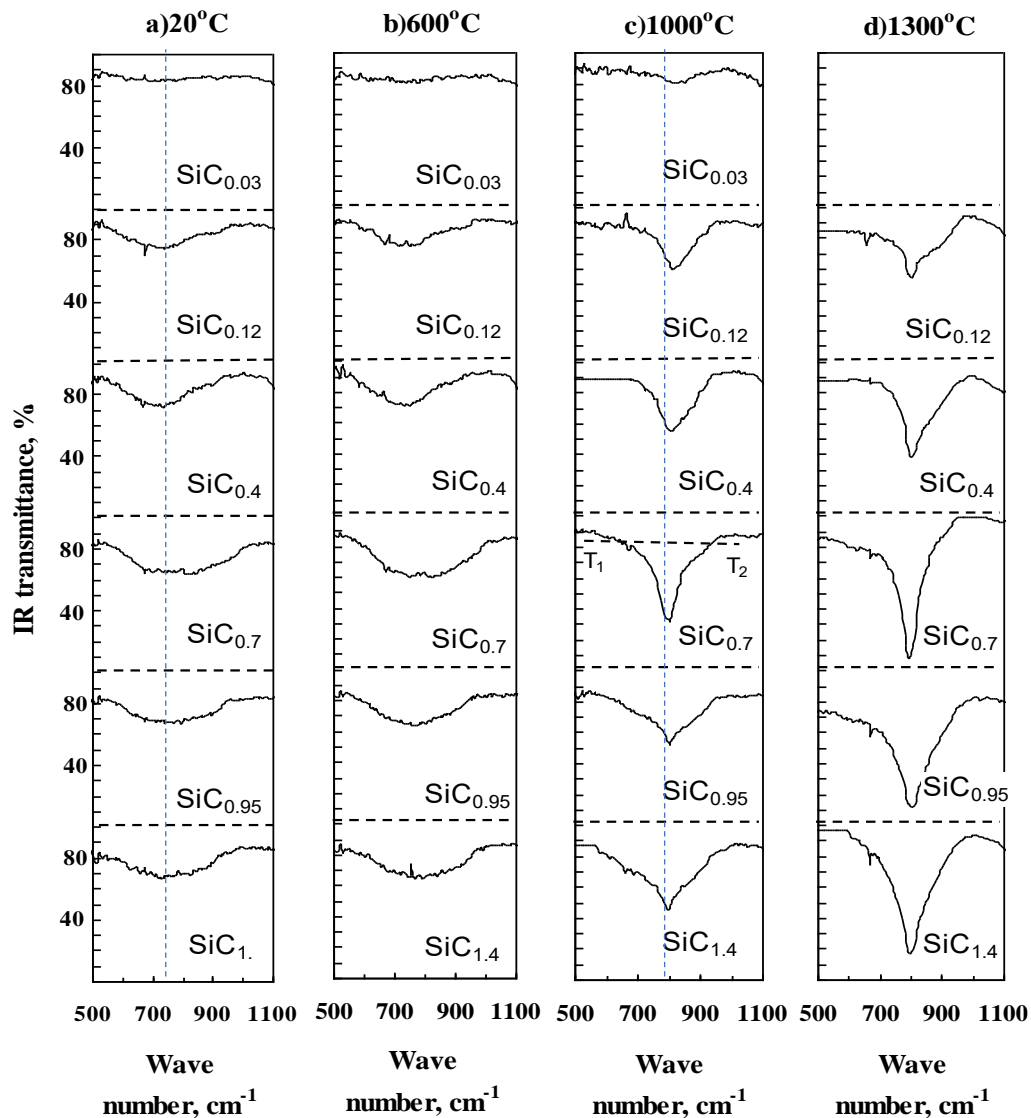
IR transmission spectra of the SiC<sub>x</sub> layers

Fig. 22. IR transmission spectra of the SiC<sub>1.4</sub>, SiC<sub>0.95</sub>, SiC<sub>0.7</sub>, SiC<sub>0.4</sub>, SiC<sub>0.12</sub> and SiC<sub>0.03</sub> layers recorded after implantation of C<sup>12</sup> ions (E = 40, 20, 10, 5 and 3 keV) into Si (a) and annealing for 30 min at temperatures 600°C (b), 1000°C (c) and 1300°C (d).

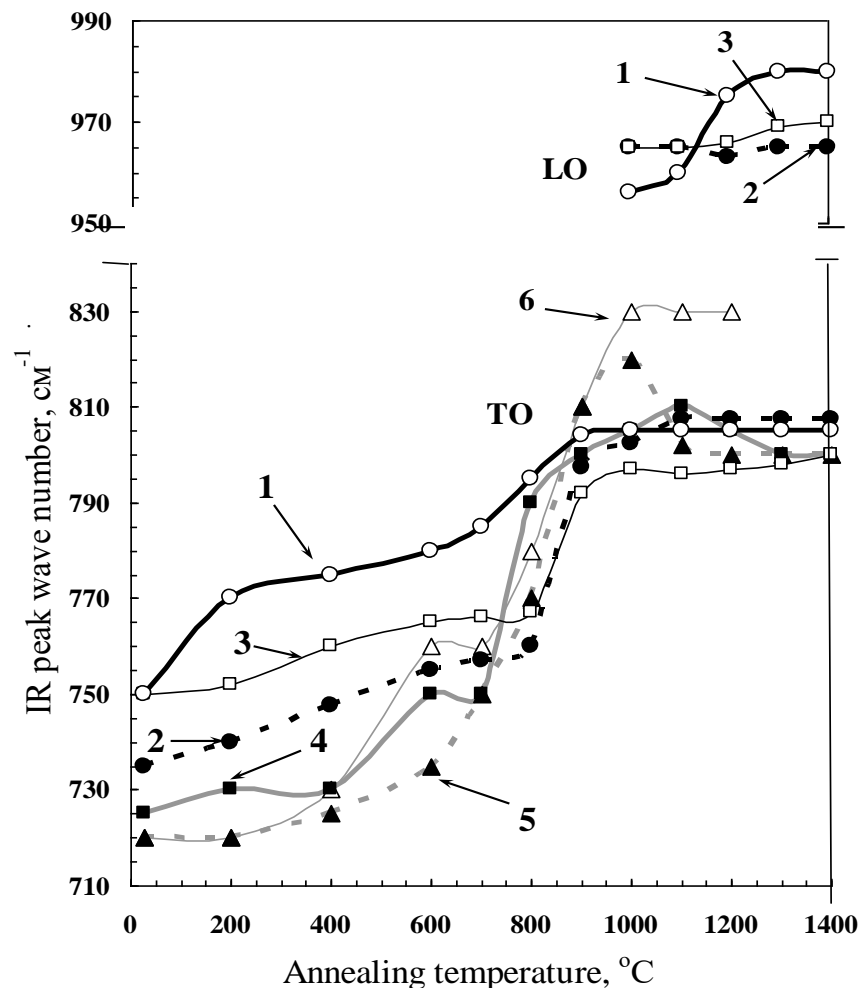


Fig. 23. Wavenumber of the IR transmittance peak for TO- and LO-phonons SiC as a function of the annealing temperature: 1 - SiC<sub>1.4</sub>, 2 - SiC<sub>0.95</sub>, 3 - SiC<sub>0.7</sub>, 4 - SiC<sub>0.4</sub>, 5 - SiC<sub>0.12</sub>, 6 - SiC<sub>0.03</sub>.

# The infrared inactive clusters, chains and a flat net

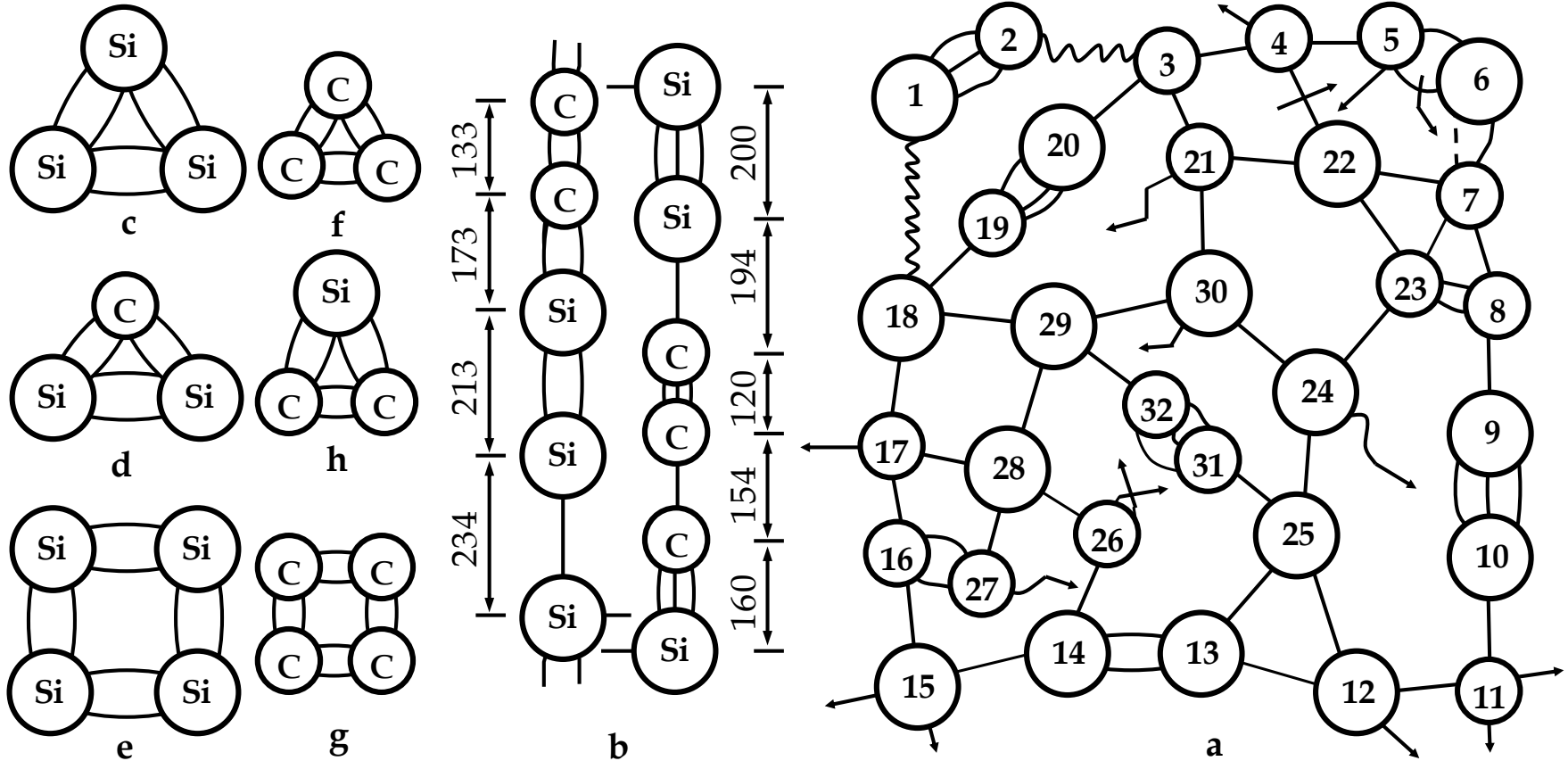


Fig. 24. Possible variants of both the infrared inactive clusters (a-h), chains of them (b) and a flat net of clusters (a) with various types of bonds between the atoms of Si (great circles) and C (small circles).

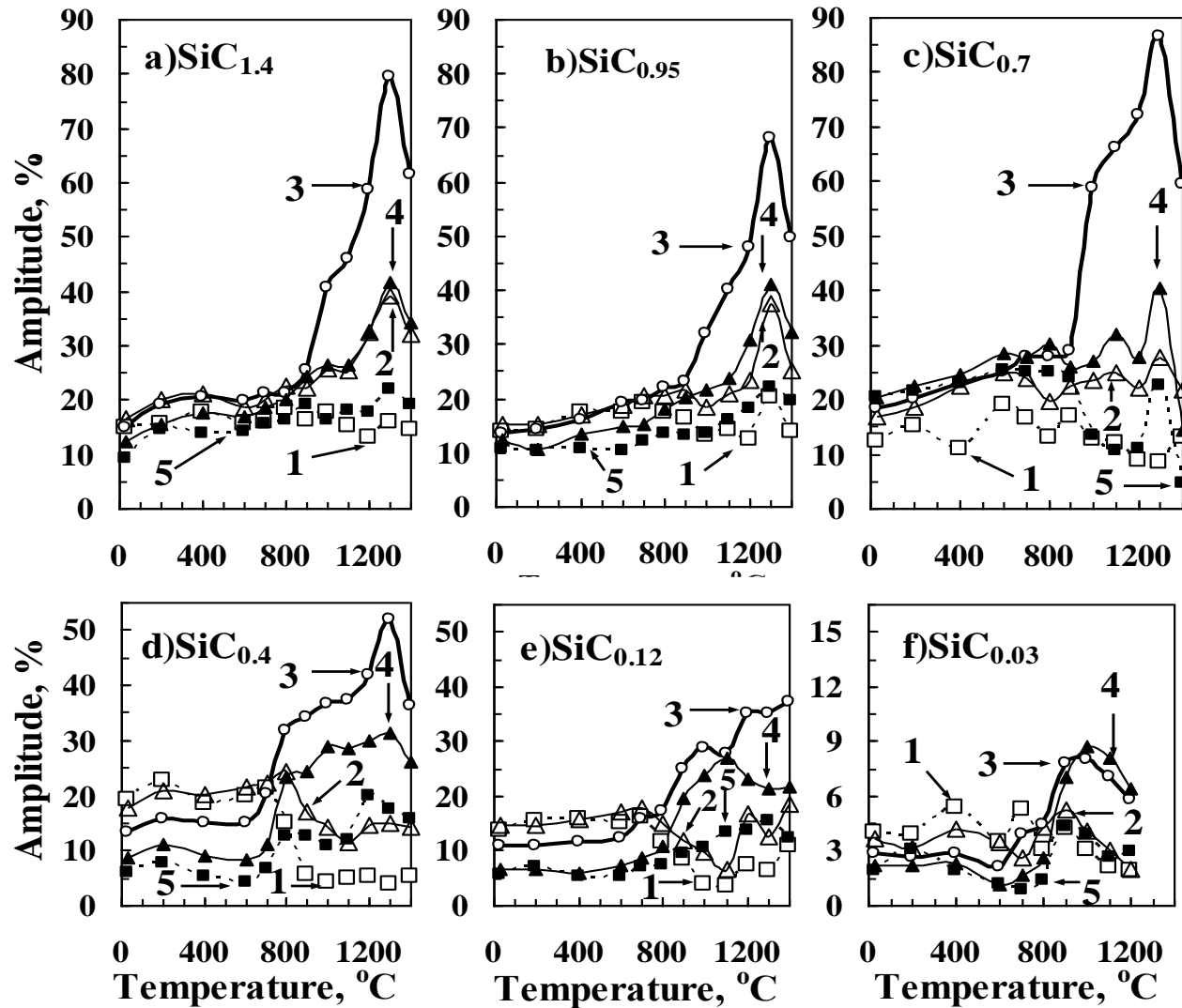


Fig. 25. Effect of the annealing temperature on the IR transmittance amplitude at wavenumbers of (1-□) 700 cm<sup>-1</sup>, (2-Δ) 750 cm<sup>-1</sup>, (3-○) 800 cm<sup>-1</sup>, (4-▲) 850 cm<sup>-1</sup>, and (5-■) 900 cm<sup>-1</sup> under normal incidence of IR radiation on the sample surface:

a) SiC<sub>1.4</sub>; b) SiC<sub>0.95</sub>; c) SiC<sub>0.7</sub>, d) SiC<sub>0.4</sub>, e) SiC<sub>0.12</sub>; f) SiC<sub>0.03</sub>.

# The area under the IR transmittance SiC-peak

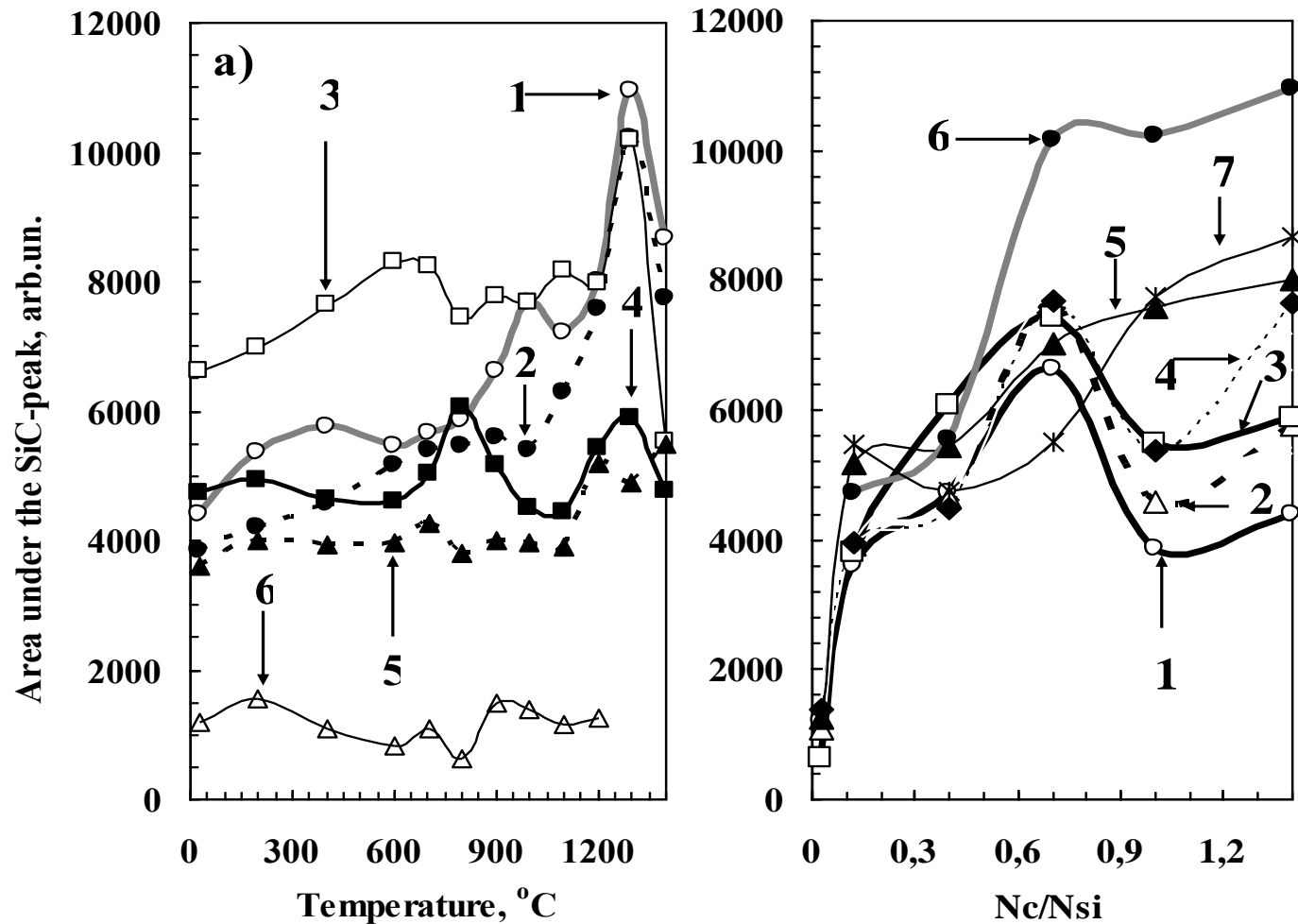
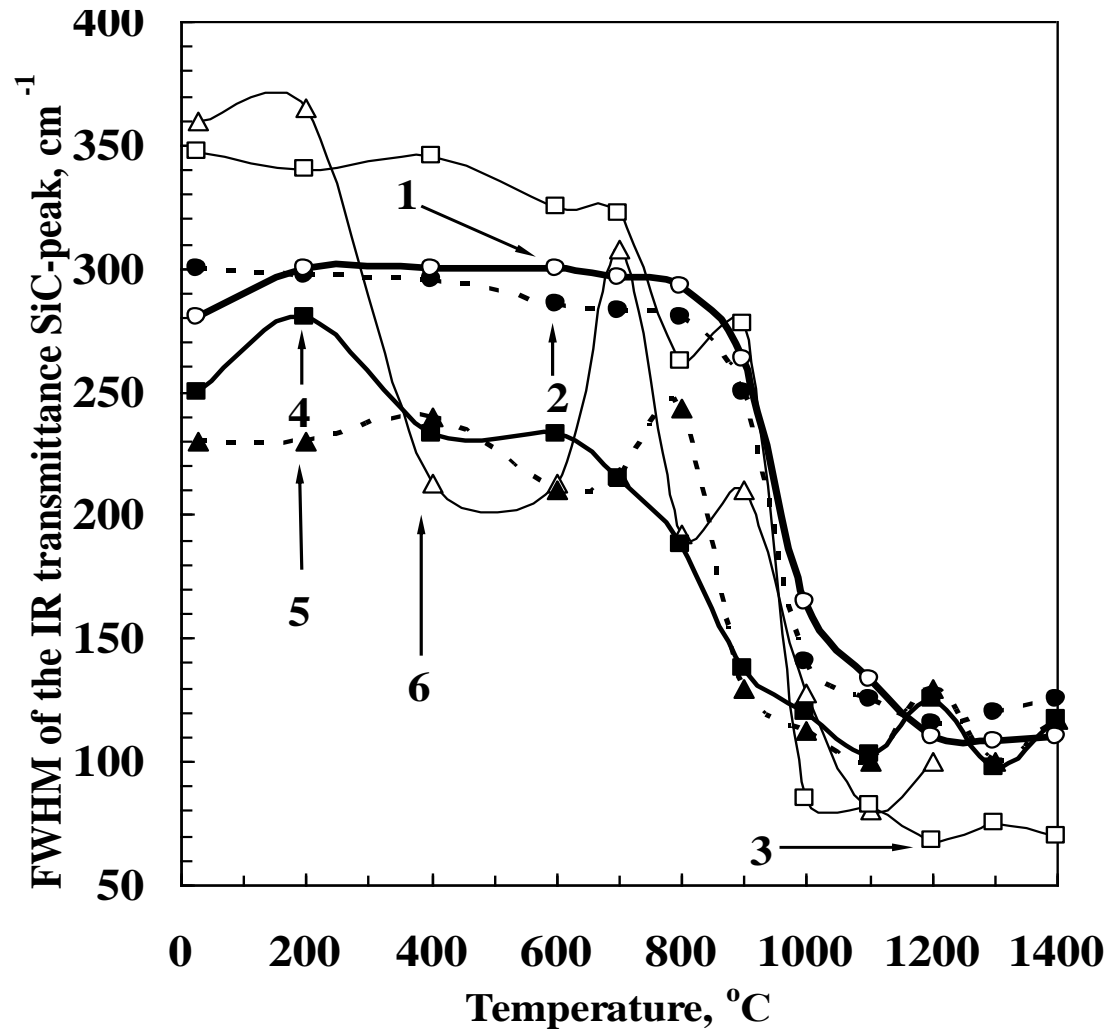


Fig. 26. Effect of the annealing temperature and concentration of carbon on the area under the IR transmittance SiC-peak for TO phonons under normal incidence of IR radiation on the sample surface: a) SiC<sub>1.4</sub> (1), SiC<sub>0.95</sub> (2), SiC<sub>0.7</sub> (3), SiC<sub>0.4</sub> (4), SiC<sub>0.12</sub> (5) и SiC<sub>0.03</sub> (6); б) 27°C (1), 400°C (2), 800°C (3), 1000°C (4), 1200°C (5), 1300°C (6), 1400°C (7).

## The FWHM of the IR transmittance SiC-peak



**Fig. 27.** Effect of the annealing temperature on the FWHM of the IR transmittance SiC-peak for TO phonons under normal incidence of IR radiation on the sample surface:  
 1 –  $\text{SiC}_{1.4}$ , 2 –  $\text{SiC}_{0.95}$ , 3 –  $\text{SiC}_{0.7}$ , 4 –  $\text{SiC}_{0.4}$ , 5 –  $\text{SiC}_{0.12}$ , 6 –  $\text{SiC}_{0.03}$ .



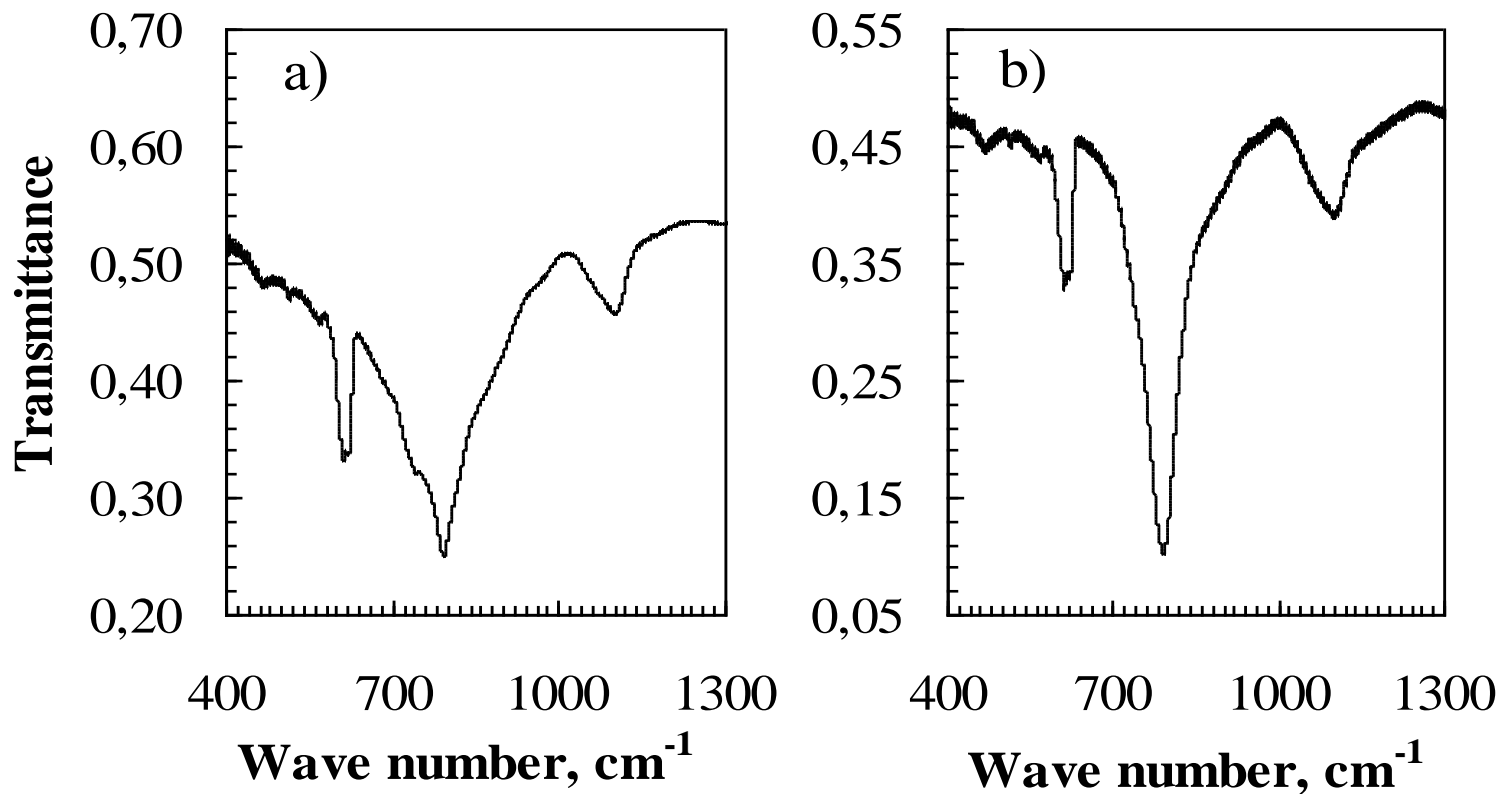


Fig. 28. IR transmission spectra for SiC<sub>0,95</sub> layer after annealing at the temperature 900°C for 30 min (a) and after processing by glow discharge hydrogen plasma for 5 min and annealing at the temperature 900°C for 30 min (b).

## AFM images of the surface of thin SiC<sub>x</sub> film

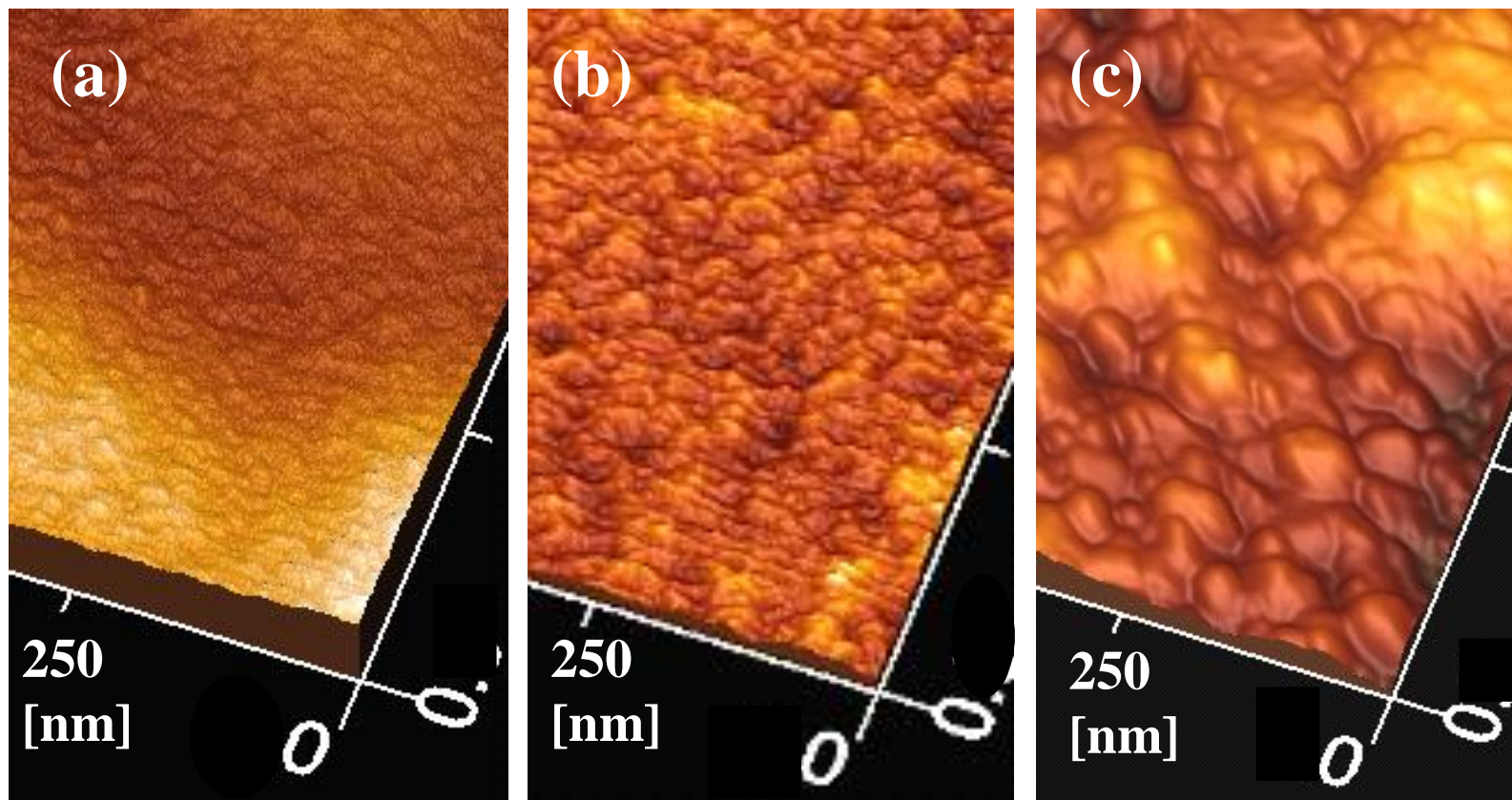


Fig. 29. AFM images from the surface of thin ( $\sim 130$  nm) SiC<sub>0.95</sub> film (a) after multiple implantation and annealing at (b) 800°C and (c) 1400°C.

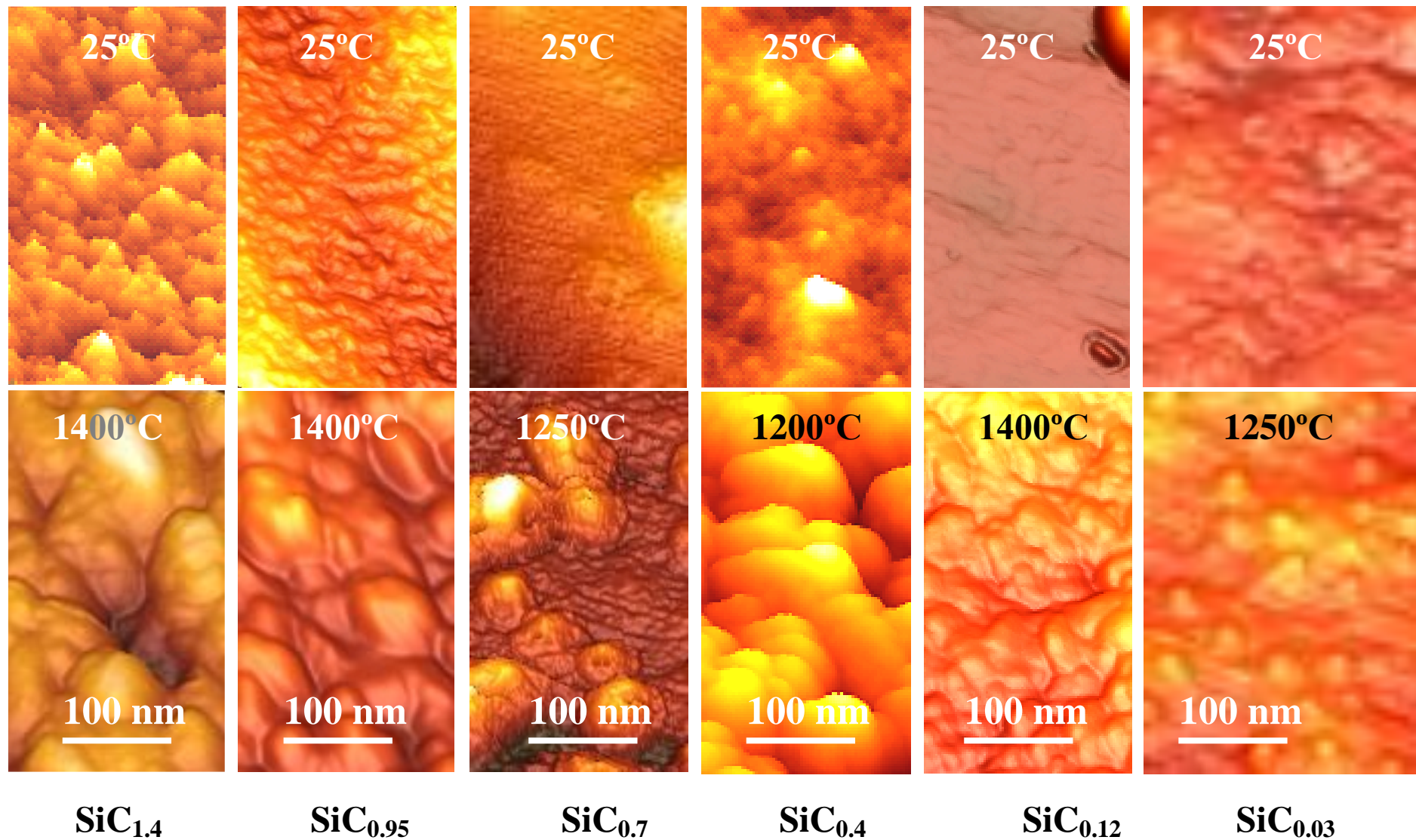


Fig. 30. Atomic force microscopy of the surface of SiC<sub>x</sub> layers with various carbon concentration before and after high temperature annealing



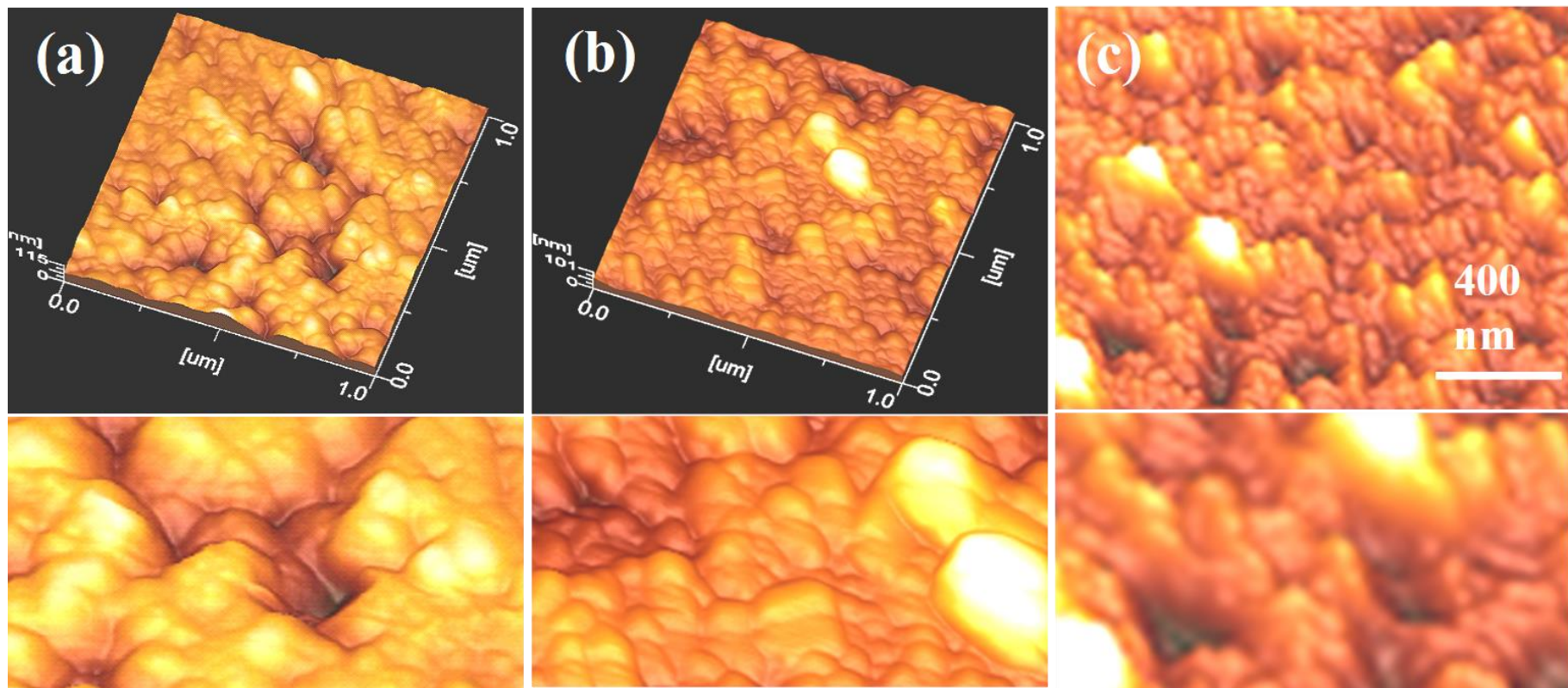


Fig. 31. Atomic force microscopy of SiC<sub>1.4</sub> layers after annealing at the temperature of 1400°C (a) and subsequent processing by glow discharge hydrogen plasma for 5 min (b, c).

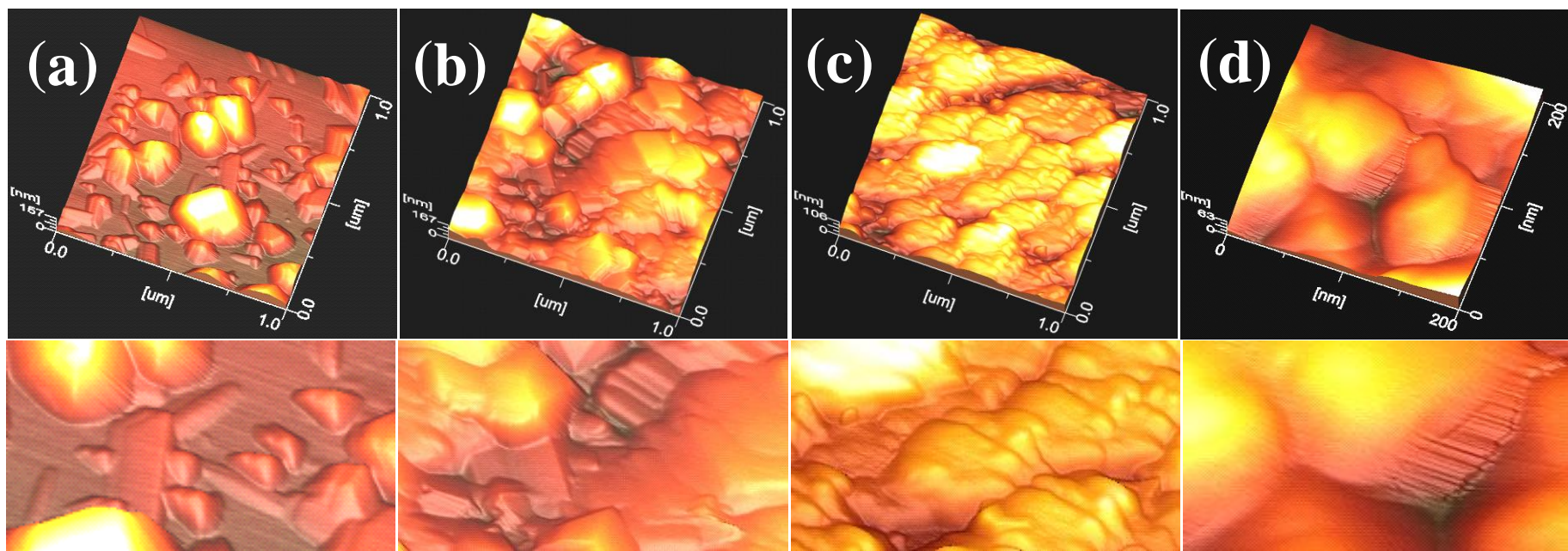


Fig. 32 Atomic force microscopy of SiC<sub>0.95</sub> layer: (a, b) after synthesis and annealing at the temperature of 900°C for 30 min; (c, d) after synthesis, processing by glow discharge hydrogen plasma for 5 min and annealing at 900°C for 30 min.



## Conclusion

1 For  $\text{SiC}_x$  layers, formed by multiple ion implantation in Si of  $^{12}\text{C}^+$  ions with energies 40, 20, 10, 5 and 3 keV, the regularities of influence of the decay of clusters and optically active bonds on the formation of tetrahedral oriented Si–C-bonds, characteristic of crystalline silicon carbide, were revealed.

2 After annealing at  $1200^\circ\text{C}$  of homogeneous  $\text{SiC}_x$  layers, largest sizes of spherical, needle- and plate-type SiC grains up to 400 nm and the largest number of tetrahedral oriented Si–C-bonds are observed for the  $\text{SiC}_{0.7}$  layer, which is due to a low carbon content in the  $\text{SiC}_{0.03}$ ,  $\text{SiC}_{0.12}$  and  $\text{SiC}_{0.4}$  layers, and a high concentration of strong clusters in the  $\text{SiC}_{0.95}$  and  $\text{SiC}_{1.4}$  layers. In the range of  $800\text{--}900^\circ\text{C}$  the most number of tetrahedral Si–C-bonds is characteristic for  $\text{SiC}_{0.4}$  layers.

3. A structural model of  $\text{SiC}_{0.12}$  layer, which shows the changes in phase composition, phase volume and average crystallite size of SiC and Si in the temperature range  $20\text{--}1250^\circ\text{C}$ , is proposed. After annealing at  $1200^\circ\text{C}$ , about 50% of its volume, free from Si–C-clusters, is consisted of Si crystallites with average size  $\sim 25$  nm, 25% of the volume –  $\beta$ -SiC crystallite with size of  $\sim 5$  nm and 25% – the c-Si recrystallized near the transition “film – substrate”.

4. At  $800\text{--}1400^\circ\text{C}$  the surface layers are deformed with the formation of grains with sizes of  $\sim 30\text{--}100$  nm, consisting of crystallites, and the recrystallized at  $1250^\circ\text{C}$  smooth surface of  $\text{SiC}_{0.03}$  layer contains evenly distributed Si:C inclusions in the form of point protrusions with a diameter of  $\sim 20$  nm.

5. The differences of the  $\text{SiC}_{0.03}$ ,  $\text{SiC}_{0.12}$  and  $\text{SiC}_{0.4}$  layers with low carbon concentration from the  $\text{SiC}_{1.4}$ ,  $\text{SiC}_{0.95}$  and  $\text{SiC}_{0.7}$  layers with high carbon concentration are manifested in the absence of LO-phonon peak of SiC in the IR transmission spectra and in a shift at  $1000^\circ\text{C}$  of minimum SiC-peak for TO phonons in the region of wave numbers higher than  $800\text{ cm}^{-1}$  characteristic for the tetrahedral bonds of crystalline SiC, which is caused by small sizes of SiC crystallites ( $\leq 3$  nm).

6. Processing by hydrogen glow discharge plasma (27.12MHz, 12.5W, 6.5Pa,  $100^\circ\text{C}$ , 5 min) of polycrystalline  $\text{SiC}_{1.4}$  layer leads to partial disintegration of  $\beta$ -SiC crystallites in layer and complete decay of Si crystallites in the transition layer “film–substrate” (“SiC–Si”). Processing by plasma and annealing at  $900^\circ\text{C}$  of  $\text{SiC}_{0.95}$  layer has led to the formation of  $\beta$ -SiC crystalline layer, which superior in structure quality the untreated by plasma layer subjected to isochronous annealing in the range  $200\text{--}1400^\circ\text{C}$ . Phenomenon of plasma-induced crystallization is a consequence of the decay of clusters during pre-treatment by glow discharge hydrogen plasma.

# STRUCTURE OF SILICON CARBIDE FILMS, GROWN BY ATOMIC SUBSTITUTION, MAGNETRON SPUTTERING AND ION IMPLANTATION TECHNIQUES IN SILICON

**K.Kh. Nussupov, N.B. Beisenkhanov, D.I. Bakranova**

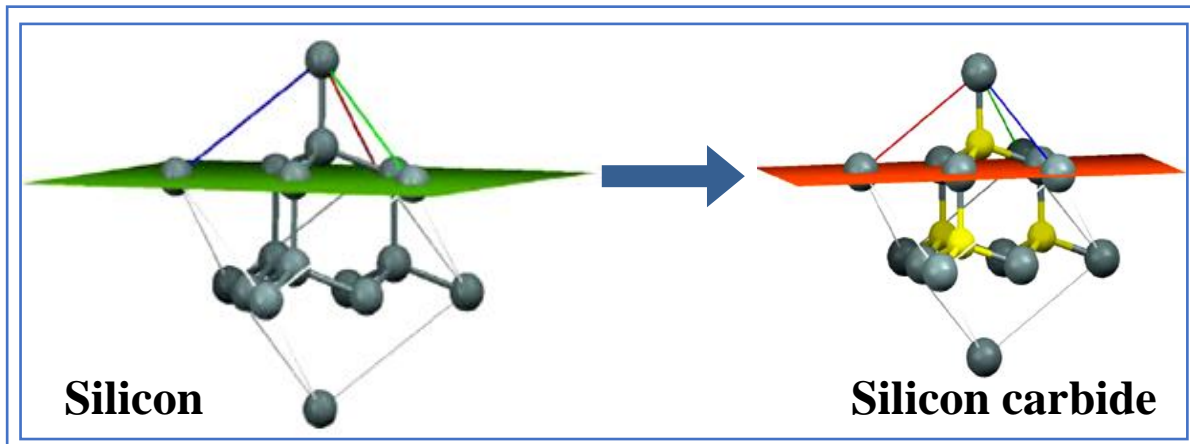
**Kazakh-British Technical University, 050000, Almaty, Kazakhstan**

## **Main publications 2017-2019:**

- 1 Kukushkin S.A., Nussupov K.Kh., Osipov A.V., Beisenkhanov N.B., Bakranova D.I. Structural properties and parameters of epitaxial silicon carbide films, grown by atomic substitution on the high-resistance (111) oriented silicon. *Superlattices and Microstructures*. 111. 2017. 899-911.
- 2 Kukushkin S.A., Nussupov K.Kh., Osipov A.V., Beisenkhanov N.B., Bakranova D.I. X-Ray Reflectometry and Simulation of the Parameters of SiC Epitaxial Films on Si(111), Grown by the Atomic Substitution Method. *Physics of the Solid State*. 59(5). 2017. 1014–1026.
- 3 K.Kh. Nussupov, N.B. Beisenkhanov, D.I. Bakranova, S. Keinbay, A.A. Turakhun, A.A. Sultan. Low-temperature synthesis of  $\alpha$ -SiC nanocrystals. *Physics of the Solid State*. Vol. 61, iss. 12. 2019. P.2473-2479.

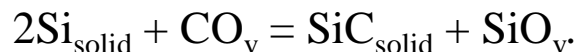
# Mechanism of synthesis of silicon carbide films

Methods for the formation of heterostructures by epitaxial growth lead to satisfactory practical results only if the lattice constants of the substrate and the film material does not differ by more than 5%. The difference in the lattice parameters of silicon carbide (SiC) and single crystalline silicon (Si) is ~19%. Therefore, the growing of highly oriented epitaxial SiC layers on Si substrate is a complex task.

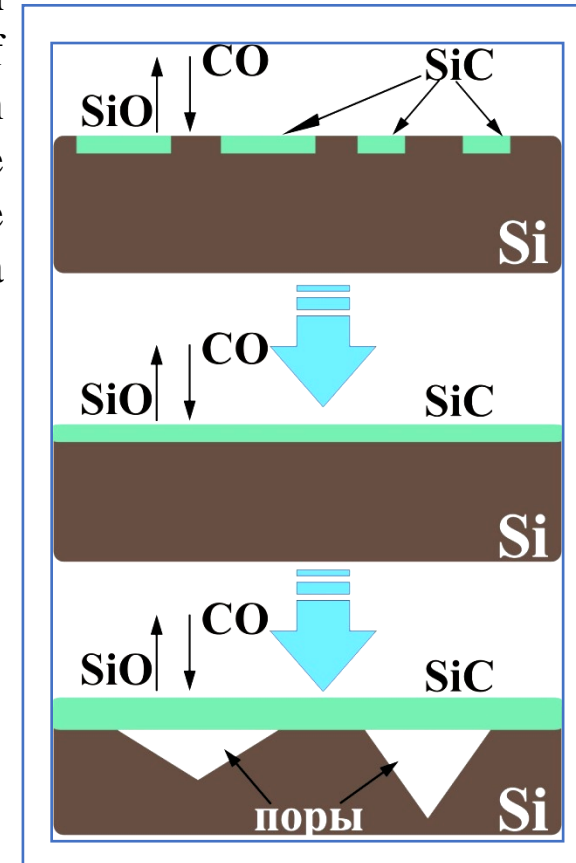


The method of growth of high quality thin SiC films on Si consists of replacing of part of the silicon atoms of the matrix on the carbon atoms to form molecules of silicon carbide.

The process of silicon atoms replacement on the carbon atoms can be realized by using following chemical reaction:

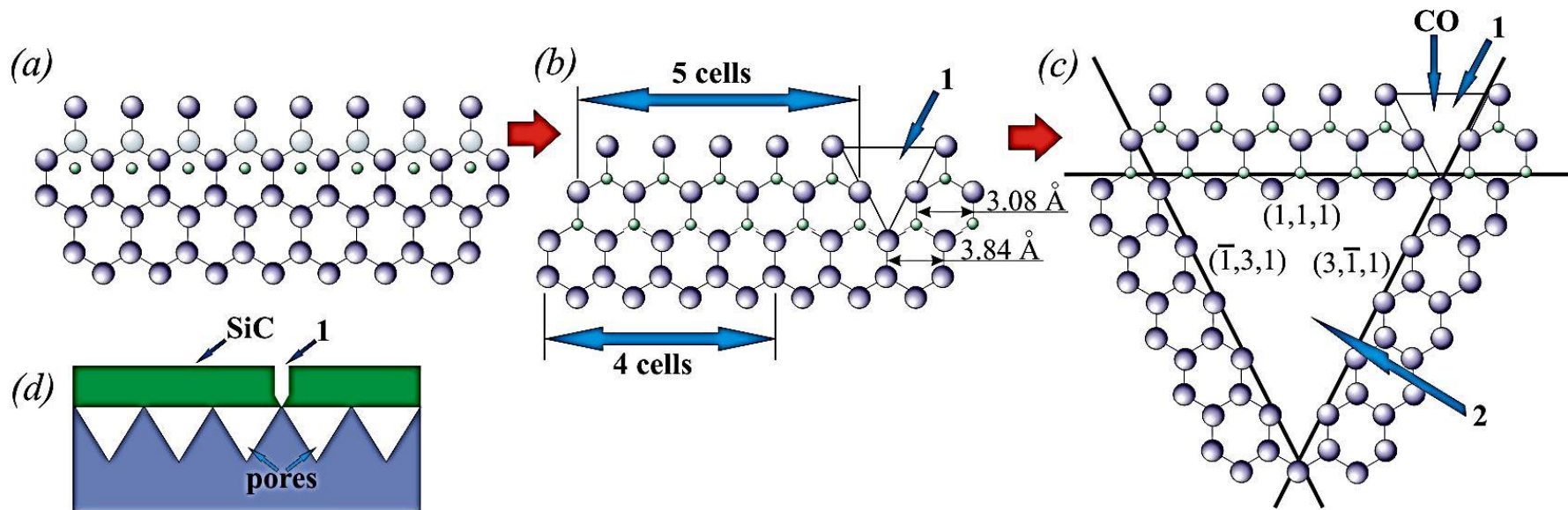


Pores with a size of 1-5 microns at a film thickness of 20-150 nm provide relaxation of the elastic stress.

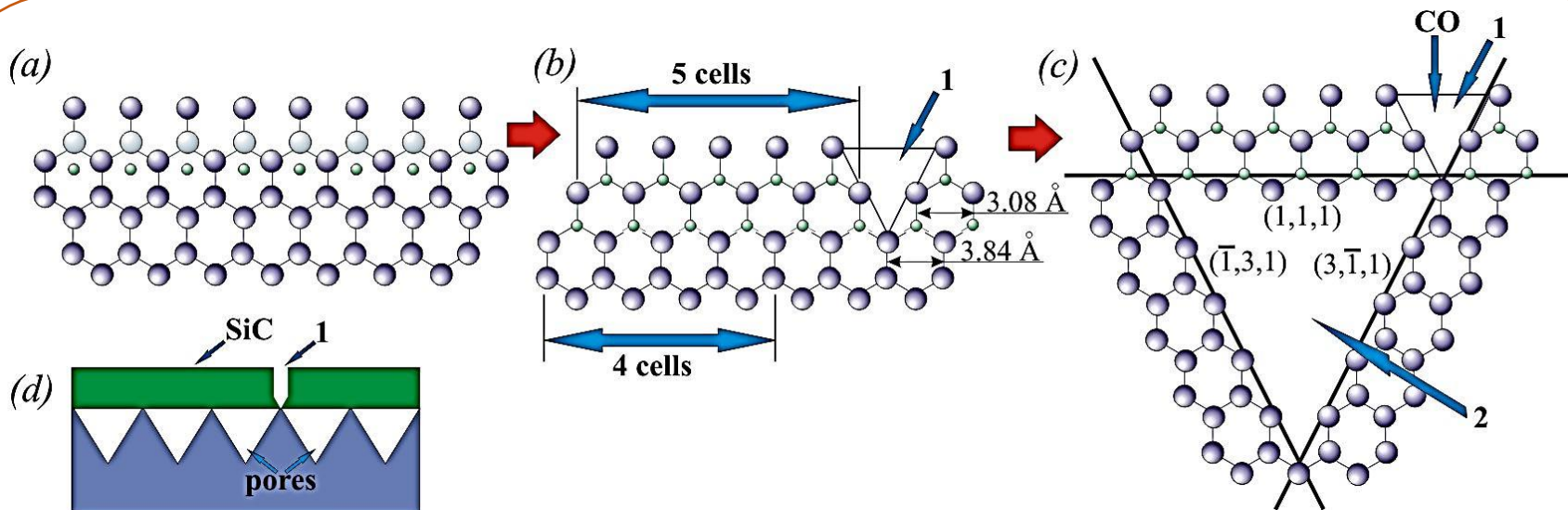


**Schematic representation of SiC film formation process by reaction between the crystalline silicon and carbon monoxide gas**

## Introduction



In the reviews [2,3], the fundamentals of the new method of synthesis of epitaxial SiC thin films on Si, were described [4-6]. It is based on the idea of replacing of some silicon atoms on carbon atoms within the silicon substrate. To implement this approach, preliminarily a carbon atom is introduced in the interstitial position of silicon lattice and, neighboring silicon atom is removed, creating a silicon vacancy (Fig. 1 (a)). An ensemble of dilatation dipoles is formed, which are stable complexes consisting of dilatation centers ( $C-V_{Si}$ ) – carbon atom in the interstitial position and silicon vacancy. These two centers of dilatation elastically interact with each other in a crystal of cubic symmetry.



Synthesis of elastic dipoles is carried out by means of a chemical reaction (1):



If the carbon atoms are displaced from interstitial positions into positions occupied by vacancies (Fig. 1 (b)), a layer of silicon carbide is formed in the upper part of the silicon. Since the lattice parameters (0.43596 nm) in SiC are much smaller than in Si (0.54307 nm), part of the volume occupied by the silicon lattice should be freed and a pore of pyramidal shape is formed below the SiC layer, bounded by (111), (1̄13) and (31̄1) planes (Fig. 1 (c)). For the same reason, contraction pores also form on the surface (Fig. 1 (b) – (d)). The distance between Si atoms along the (111) plane in the projection onto the (112̄) plane is 3.84 Å, and between Si atoms in SiC is 3.08 Å. The distance between the planes of five cells in SiC  $\approx 15.4$  Å almost coincides with the distance between the planes of four cells in Si  $\approx 15.4$  Å.



## Experimental Details

### Preparing of Si samples

<b>№ 1</b>	<b>grinding and polishing</b>	<b>HF:HNO<sub>3</sub> = 1:10</b>	<b>KOH</b>
<b>№ 2</b>	<b>grinding and polishing</b>	<b>-</b>	<b>KOH</b>
<b>№ 3</b>	<b>grinding and polishing</b>	<b>HF:HNO<sub>3</sub> = 1:10</b>	<b>KOH</b>
<b>№ 4</b>	<b>grinding and polishing</b>	<b>HF:HNO<sub>3</sub> = 1:10</b>	<b>KOH</b>

### Growth conditions of the silicon carbide film

<b>№</b>	<b>Temperature, °C</b>	<b>Pressure, Pa</b>	<b>Growth time, min</b>
<b>1</b>	<b>1250</b>	<b>264</b>	<b>15</b>
<b>2</b>	<b>1250</b>	<b>264</b>	<b>15</b>
<b>3</b>	<b>1330</b>	<b>395</b>	<b>7</b>
<b>4</b>	<b>1330</b>	<b>395</b>	<b>7</b>

Two batches of n-type single crystalline (111) oriented Si samples with a resistivity in range of 1987–3165 Ohm·cm, with a diameter of 20 mm and 1300 μm thick, for the synthesis of single crystalline SiC films, were used. Samples were subjected to plane-parallel double-sided grinding and polishing till gaining the high gloss and the thickness of 1100 μm.

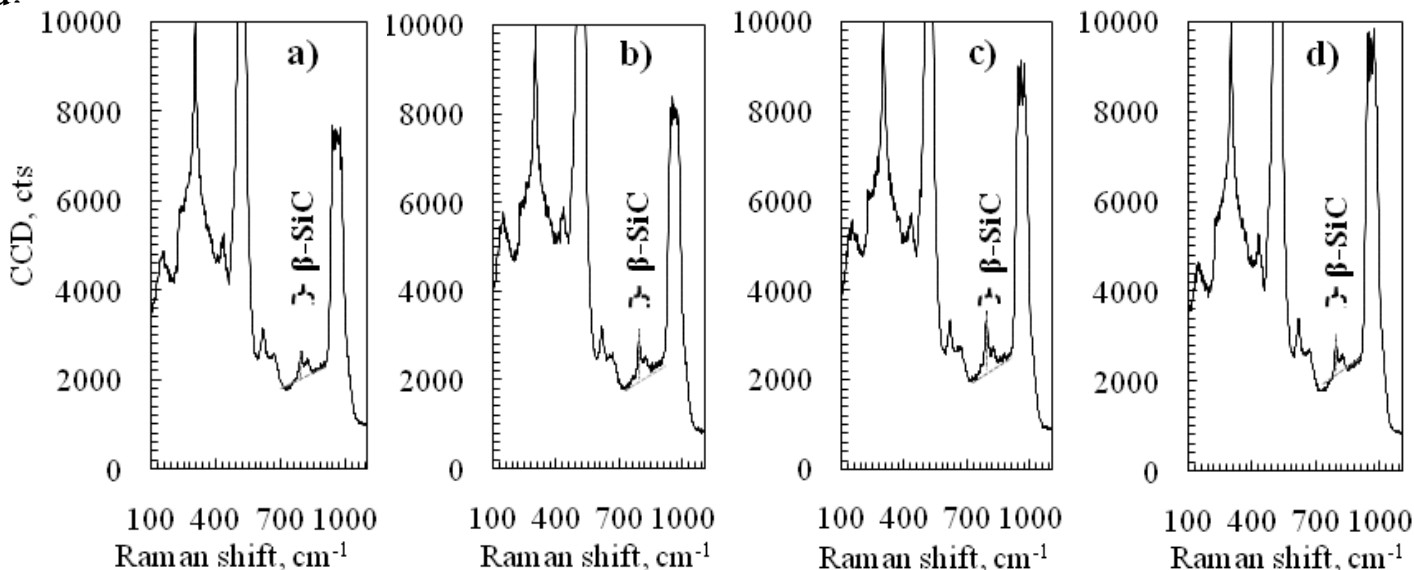
Then samples Nos. 1, 3 and 4 (except sample No. 2) were etched in acid mixture HF: HNO<sub>3</sub> (in a ratio of 1:10) up to a thickness of 870 μm. Further, all samples Nos. 1-4 were etched in an alkaline KOH solution. Thereafter, all samples were covered with a layer of hydrogen (were hydrogenated) in order to prevent the silicon oxide formation.

Synthesis of SiC films was carried out in the special installation [3,6], in gas mixture of CO and SiH<sub>4</sub>. The SiC films synthesis was carried out on the samples Nos. 1 and 2 for 15 min at the temperature of 1250°C and the pressure of the main gas CO 264 Pa, and on the samples Nos. 3 and 4 – for 7 min, 1330°C and 395 Pa. CO gas consumption during the synthesis of all films was 12 sccm, and SiH<sub>4</sub> – 0.25 sccm.

## Studies of Raman spectra

In Raman spectra of films Nos. 1 – 4 (Fig.2 (a) – (d)), in addition to modes of crystalline Si substrate ( $\sim 303$ ,  $519.7$  and  $960$   $\text{cm}^{-1}$  [16, 17]), broad peaks appear at  $730$ - $860$   $\text{cm}^{-1}$  with the center in TO mode of 3C-SiC at  $\sim 796$   $\text{cm}^{-1}$  [18,19], consisting of two components at  $792.6 \pm 0.3$   $\text{cm}^{-1}$  and  $822.7 \pm 1.1$   $\text{cm}^{-1}$ . Location of maximum at  $792.6 \pm 0.3$   $\text{cm}^{-1}$  suggests an overlay of TO modes of 3C-SiC ( $\sim 796$   $\text{cm}^{-1}$ ) and 6H-SiC ( $\sim 788$   $\text{cm}^{-1}$ ) [18]. At the foot of this peak, the overlay of small TO peaks of 4H-SiC ( $\sim 764$   $\text{cm}^{-1}$ ) or 6H-SiC ( $\sim 766$   $\text{cm}^{-1}$ ) is observed. The peak at  $822.7$   $\text{cm}^{-1}$  indicates the presence of a phase, for analysis of which additional studies are required.

**Fig. 2.** The Raman spectra of crystalline SiC films on silicon substrates, synthesized by atoms substitution in the crystal lattice of silicon. Samples (a) No.1, (b) No.2, (c) No. 3 and (d) No.4.



The area  $S$  of the double SiC peak for samples No. 1, 2, 3 and 4 are equal to the values of 26591, 34275, 39776 and 33858 a.u. and CCD amplitude – 680, 1160, 1400 and 960 cts, respectively. The highest content of crystalline SiC phases is assumed in films No.2 and No.3.

### 3.2 Studies by atomic force microscopy and profilometry

AFM studies of surface microstructure of the film No.1 on areas  $1 \times 1 \mu\text{m}$  (Fig. 4 (a)) more clearly shows that the film surface has a pyramidal structure and is composed of high-quality crystals of sizes  $\sim 100 \times 100 \text{ nm}$ , having a clear fragmentation with height fluctuations up to 26 nm, formed for 15 minutes of synthesis at adding of  $\text{SiH}_4$  into CO gas. Surface of the film No. 2 (Fig. 4 (b)) has a step-like structure with the height fluctuations up to 38 nm and more distinct fragmentation of high-quality crystals of sizes  $\sim 200 \times 150 \text{ nm}$ . SiC films Nos. 3 (Fig. 4 (c)) and 4 (Fig. 4 (d)) have indistinct grain fragmentation with smaller height variations up to 21-22 nm. Higher pressure of gases (395 Pa) and temperature of process ( $1330^\circ\text{C}$ ) allow to assume supersaturation by carbon atoms of films and their nonequilibrium fast growth with a formation of needle crystals or whiskers (Fig. 4 (d)). It may promote the formation of strong carbon clusters that prevent the formation of crystals with clear fragmentation [11,13,14,20].

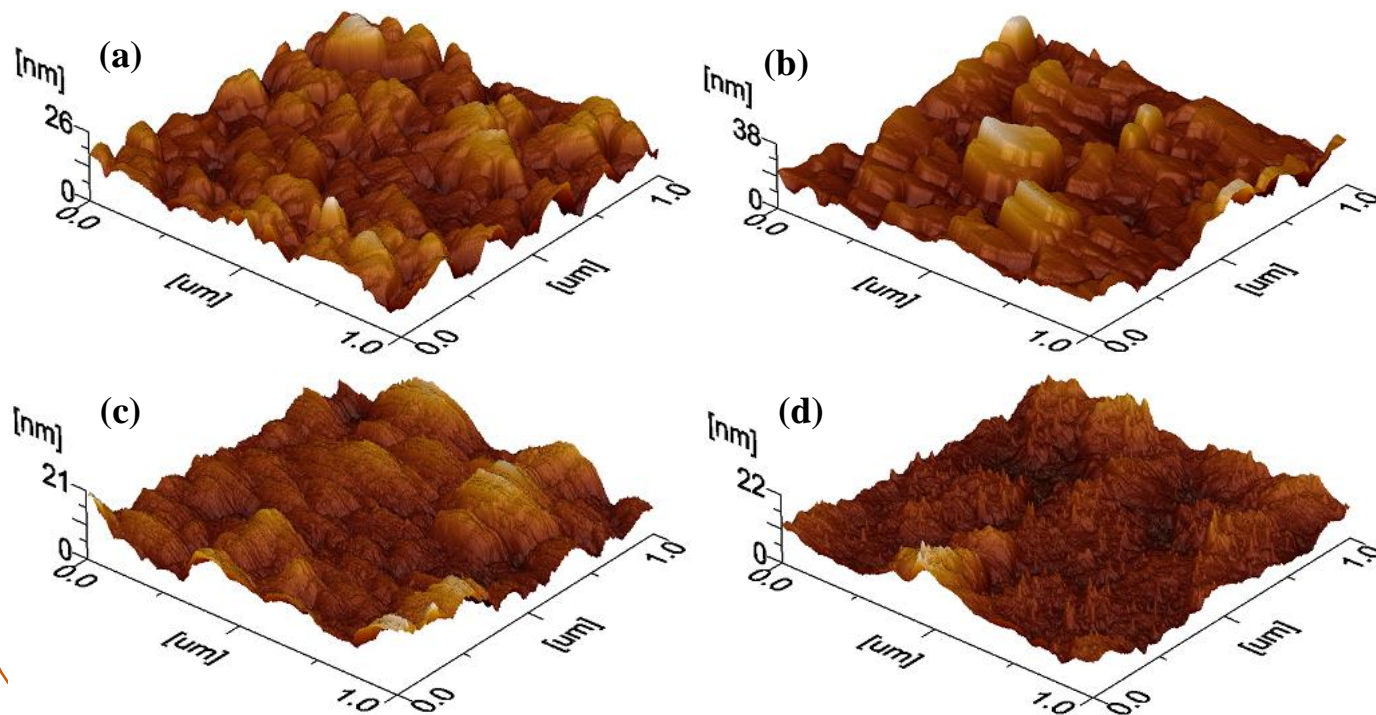


**Fig. 4.** Topography of the surfaces of the SiC films of Nos. 1 – 4, synthesized by atoms substitution in the silicon lattice. Samples (a) No.1, (b) No.2, (c) No. 3 and (d) No.4.

### 3.2 Studies by atomic force microscopy and profilometry

Average roughness  $R_a$  of films Nos. 1 – 4 on the microregions  $200 \times 200$  nm were:  $R_{a1} = 1.58$  nm;  $R_{a2} = 6.19$  nm;  $R_{a3} = 2.95$  nm;  $R_{a4} = 1.77$  nm. Lower roughness of films Nos. 1, 3 and 4 is due to the fact that the initial surface of these samples is not only polished, like the surface of sample No. 2, but also etched into HF:  $\text{HNO}_3$ . However, as shown the studies on profilometer NewView 6000, on macroregions of SiC surface with area  $701 \times 526$   $\mu\text{m}$  (Fig. 5 (a)) or  $350 \times 263$   $\mu\text{m}$  (Fig. 5 (b)), the treatment of sample No. 1 in acid mixture lead to an increase of the average surface roughness from  $R_a = 5.684$  nm (Fig. 5 (b)) up to  $R_a = 34.918$  nm (Fig. 5 (a)) due to the formation of etch pits. These data do not contradict with the data of AFM for the surface microregions, since the surface curve of sample No.2 on small regions is less smooth (Fig. 5 (b)).

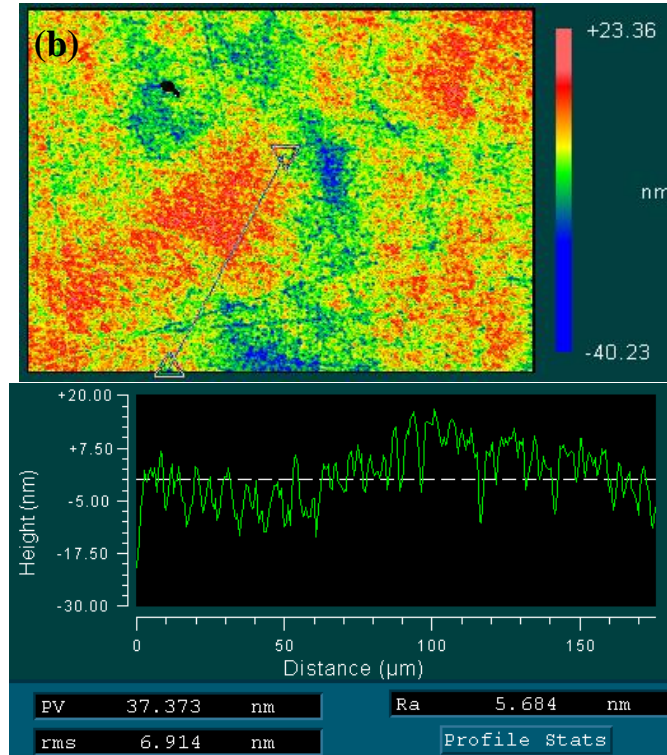
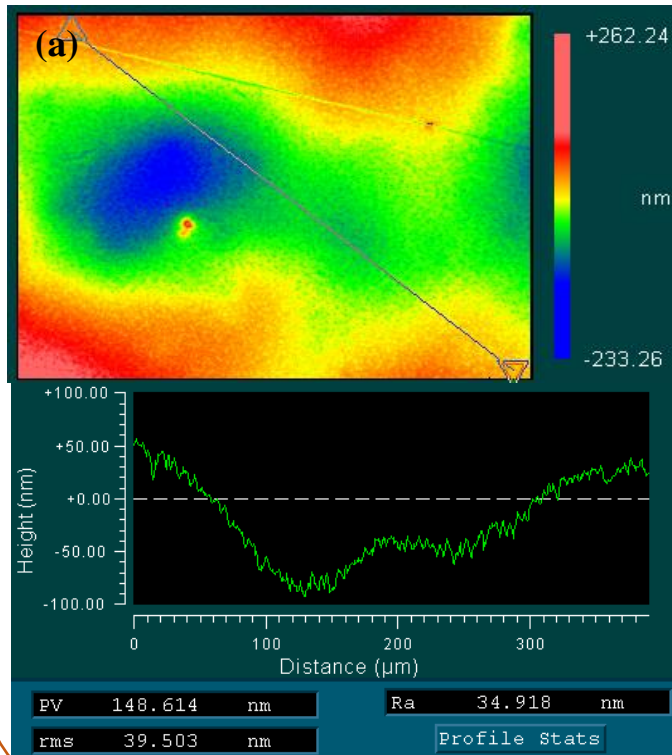
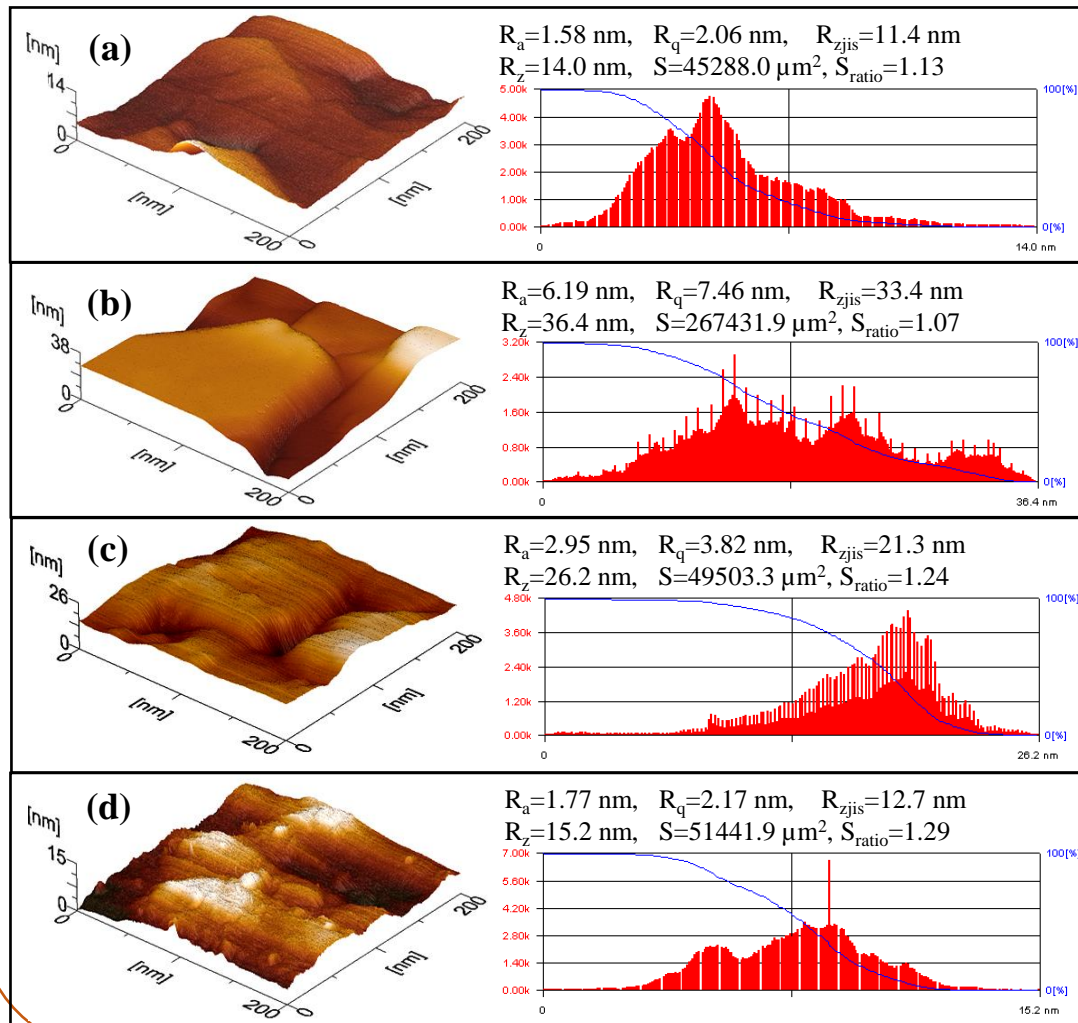


**Fig. 5.** The surface profile and roughness of (a) SiC sample No. 1 (region  $701 \times 526$   $\mu\text{m}$ ) after polishing and chemical etching in acid mixture HF :  $\text{HNO}_3$  (in proportion 1 : 10) for 15 minutes and (b) SiC sample No. 2 (region  $350 \times 263$   $\mu\text{m}$ ) without chemical etching



## 3.2 Studies by atomic force microscopy and profilometry

As shown by AFM data (Fig. 3), on the surface of samples No. 1, 3, 4 and on the lateral faces in the lower part of protrusions on the surface of sample No. 2, a "visualization" of planes ( $\bar{1}10$ ) is observed along which, according to [2], lie dilatation dipoles. Substitution of part of silicon atoms by carbon atoms leads to parallel discontinuities on the surface and the formation of contraction pores in form of nano-cracks. The supply of  $\text{SiH}_4$  gas leads to partial healing of nano-cracks and the



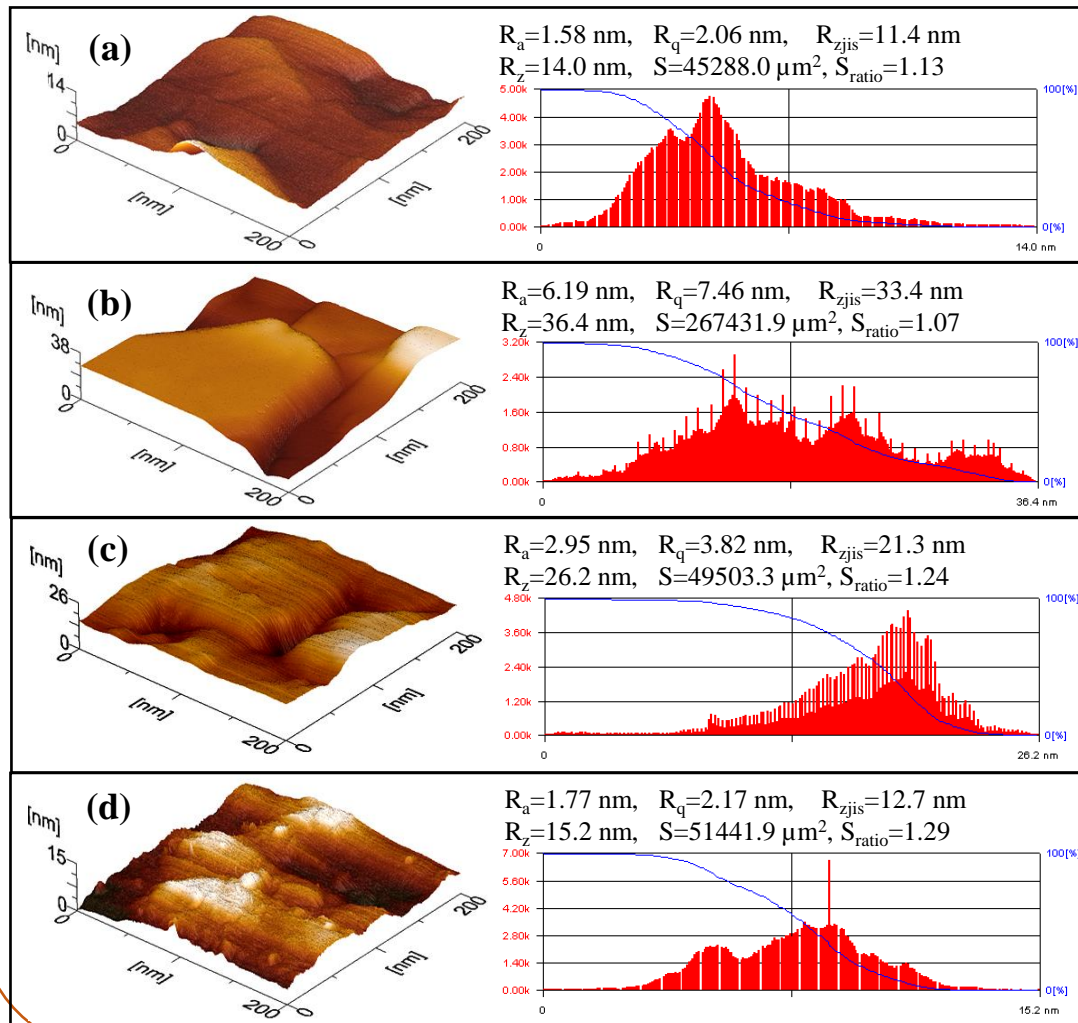
formation of "scars" on the surface. "Stacks" of layers perpendicular to the surface, like stacks of playing cards or ribbons exposed on their edges, are formed. This layered structure partially comes onto the surface.

**Fig. 3.** Topography and surface roughness of SiC films (a) No.1, (b) No.2, (c) No. 3, (d) No.4:  $R_a$  – average roughness;  $R_{zjis}$  – average roughness of 10 points;  $R_z$  – difference between the maximum and minimum height;  $R_q$  – square root of arithmetic mean roughness squares,  $S$  – net surface area,  $S_{ratio}$  – ratio of  $S$  to flat surface  $S_0$ ; right shows histograms of height distribution (axis of abscissa – height in nm, axis of ordinate –  $k$ -frequency of height values repetition).



## 3.2 Studies by atomic force microscopy and profilometry

The SiC layers of various polytypes may be present in "stacks" of layers, as show the Raman spectroscopy data. The higher the synthesis temperature and the larger was etched the original Si surface, the better these planes are visualized [2]. Indeed, after prolonged etching and removal of the damaged layer, the silicon surface becomes uniform and continuous, in which, in the process of substitution of atoms, the elastic forces at accumulation forms long cracks, as knife in the



watermelon crust. The planes ( $\bar{1}10$ ) more clearly appeared on the surface of etched samples Nos. 1, 3, 4, as compared with sample No. 2 (Fig. 3).

**Fig. 3.** Topography and surface roughness of SiC films (a) No.1, (b) No.2, (c) No. 3, (d) No.4:  $R_a$  – average roughness;  $R_{zjis}$  – average roughness of 10 points;  $R_z$  – difference between the maximum and minimum height;  $R_q$  – square root of arithmetic mean roughness squares,  $S$  – net surface area,  $S_{ratio}$  – ratio of  $S$  to flat surface  $S_0$ ; right shows histograms of height distribution (axis of abscissa – height in nm, axis of ordinate –  $k$ -frequency of height values repetition).

### 3.3 Studies by electron diffraction

Fig. 6 shows the electron diffraction patterns of the SiC films Nos. 1 – 4, obtained in two azimuth directions: [110] and [112]. Point reflections testify that the (111) oriented 3C-SiC layer lies on the surface of Si samples Nos. 1 – 4, and the direction [111] of this layer is perpendicular to the substrate surface. SiC films are epitaxial and do not contain twins on the surface. No rings corresponding to polycrystalline phases of silicon carbide are observed in the patterns.

The surface of samples Nos. 1 and 2 has a reconstruction  $3\times 3$  along the [112] direction [21,22]. Strands, corresponding to the reconstructed surface, are indicated by the arrows.

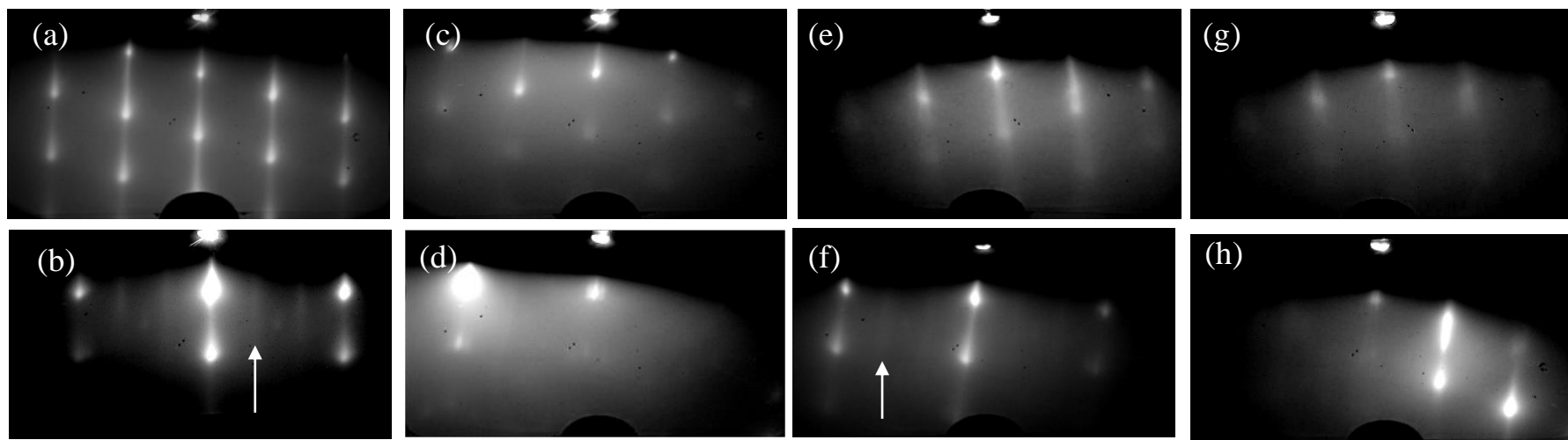


**Fig. 6.** SiC films electron diffraction patterns from samples No. 1, taken in the azimuth (a) [110] and (b) [112]; No. 2, taken in the azimuth (c) [110] and (d) [112]; No. 3, taken in azimuths (e) [110] and (f) [112]; No. 4, taken in the azimuth (g) [110] and (h) [112].

### 3.4 Studies by photographic X-ray diffraction

Fig. 7 shows that X-ray diffraction patterns of SiC films contain almost all known lines of  $\beta$ -SiC due to a high perfection degree of SiC nanocrystals structure. X-ray diffraction technique analyses the surface layers with thickness of more than  $1\ \mu\text{m}$ . In contrast, electron diffraction analyses the layers of  $\sim 15\ \text{nm}$  thick. This implies that SiC surface layer has a single crystalline structure (section 3.3), and SiC nanocrystals can be arranged both on the interface "SiC film - Si substrate" [3], and inside Si substrate, covering the inner surface of pores.

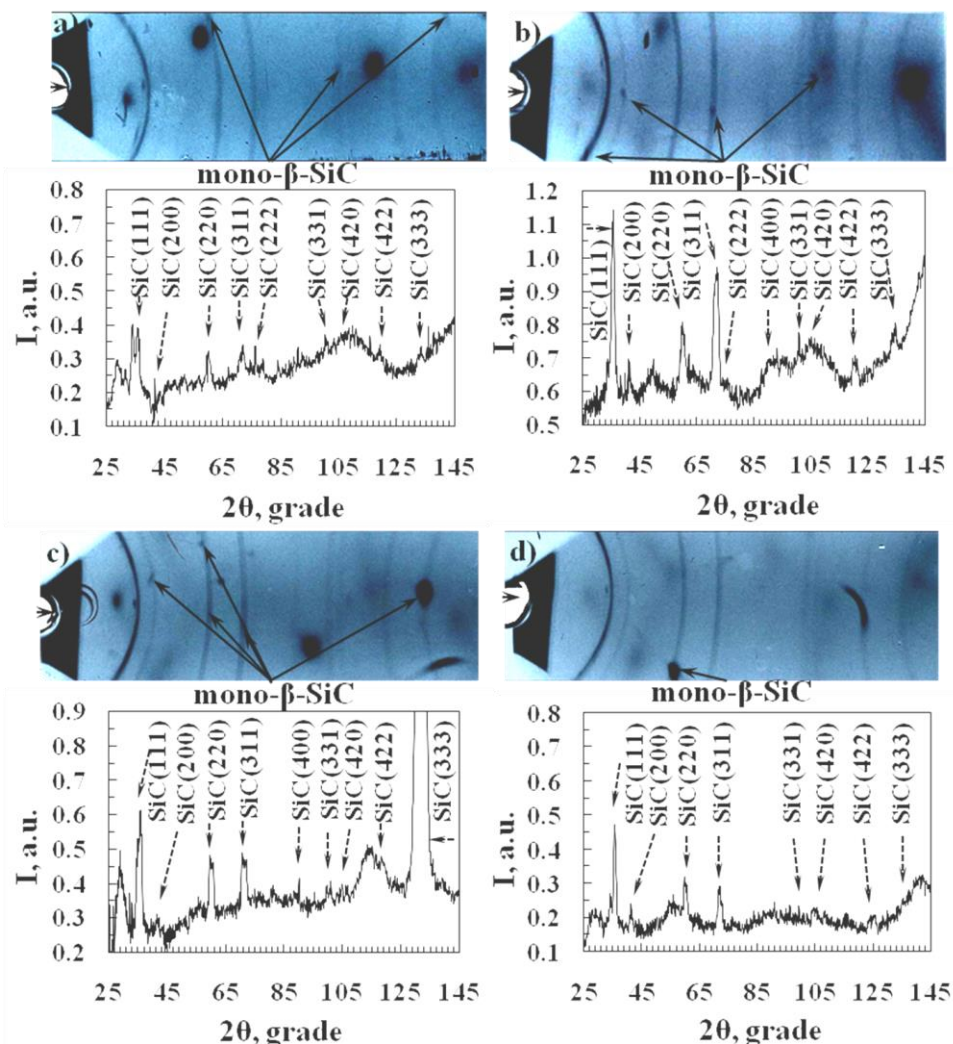


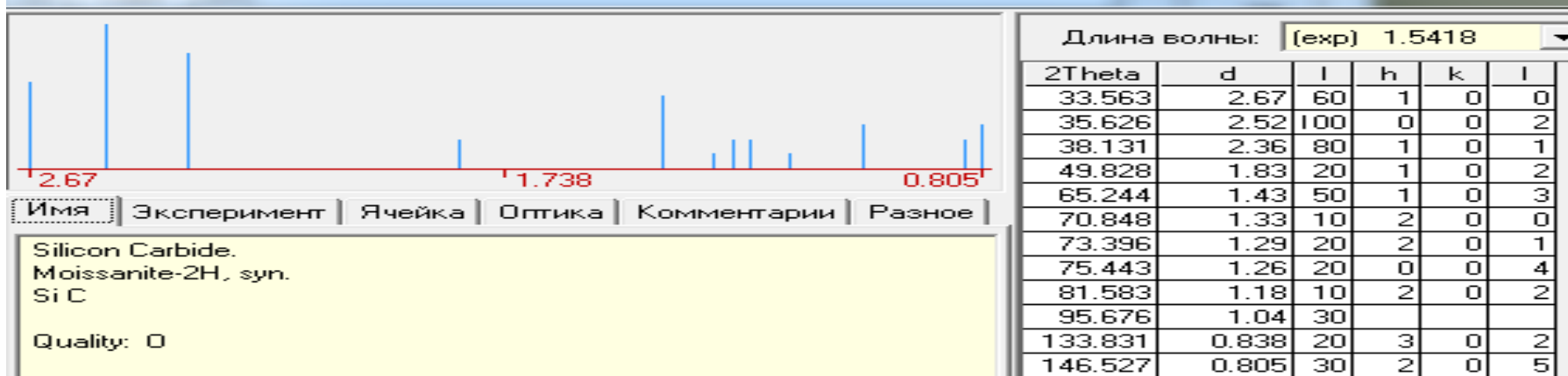
**Fig. 7.** The X-ray diffraction patterns of thin silicon carbide films and the X-ray reflection intensity  $I(2\theta)$  for samples (a) No. 1, (b) No. 2, (c) No. 3, (d) No. 4.



29 - 1129



19 - 1138





The overlay of individual reflexes of large SiC crystals on some lines of nanocrystalline  $\beta$ -SiC phase is observed. Using the *Clark and Zimmer* method, the sizes of  $\beta$ -SiC large crystals were determined. According to this method, changes in the reflexes sizes on the diffraction patterns from 0.20 to 1.20 mm correspond to a linear change in grain sizes from 10 to 85  $\mu\text{m}$ .

The SiC large crystal sizes were equal for samples:

№1 – 85×110  $\mu\text{m}$  in (220) plane, 85×120  $\mu\text{m}$  in (331) plane;

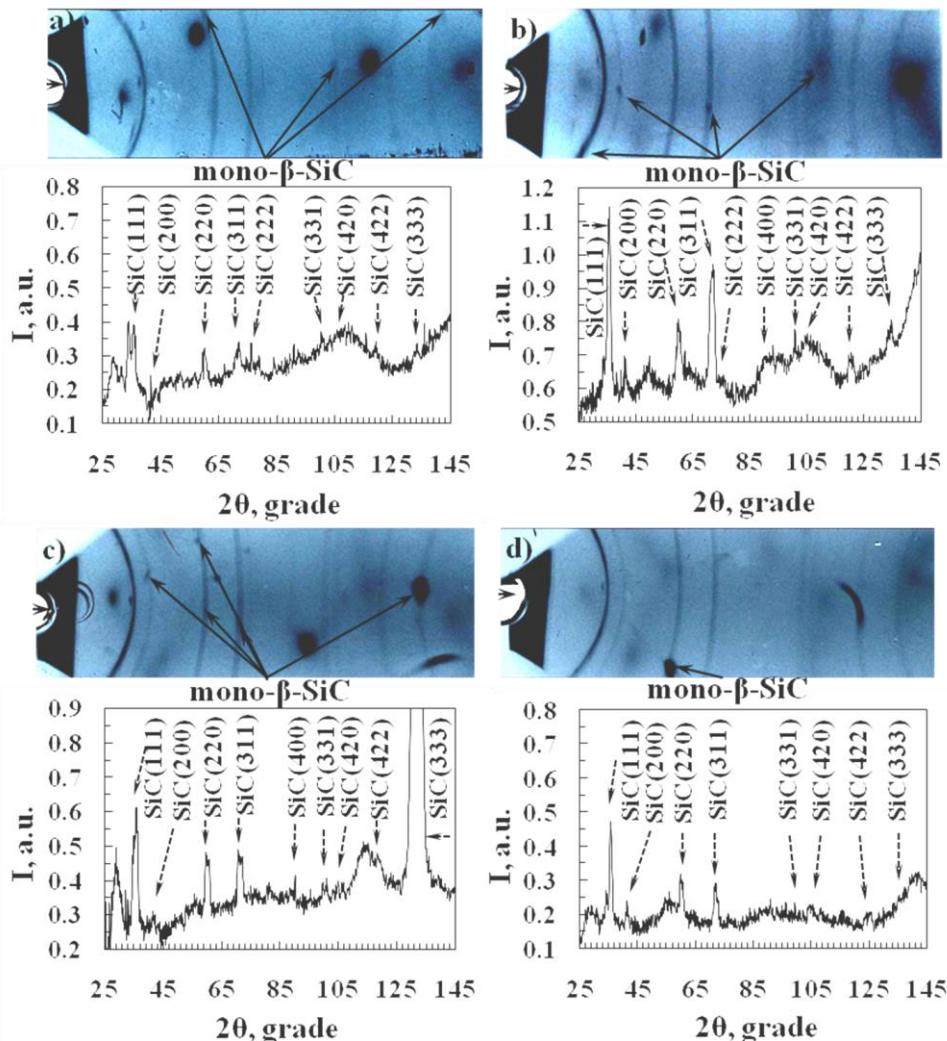
№2 – 130×35  $\mu\text{m}$  in (111) plane, 70×60  $\mu\text{m}$  in (200) plane, 85×70  $\mu\text{m}$  in (311) plane and 60×85  $\mu\text{m}$  in (420) plane;

№3 – 265×220  $\mu\text{m}$  in (333) plane;

№4 – 180×180  $\mu\text{m}$  in (220) plane.

In diffraction patterns of samples №3 and №4, a reflex in plane (333) or (220), comparable in size to Si substrate reflex or the beam size, is observed. These reflexes indicate the presence of  $\beta$ -SiC single-crystal layer. Sample №2 has a highest perfection degree and volume of the nanocrystalline  $\beta$ -SiC phase.

## Photographic X-ray diffraction





## Photographic X-ray diffraction

Average sizes of  $\beta$ -SiC nanocrystals were determined with Jones method by using Scherrer formula:

$$\varepsilon = \frac{R\lambda}{\beta \cdot \cos \theta}$$

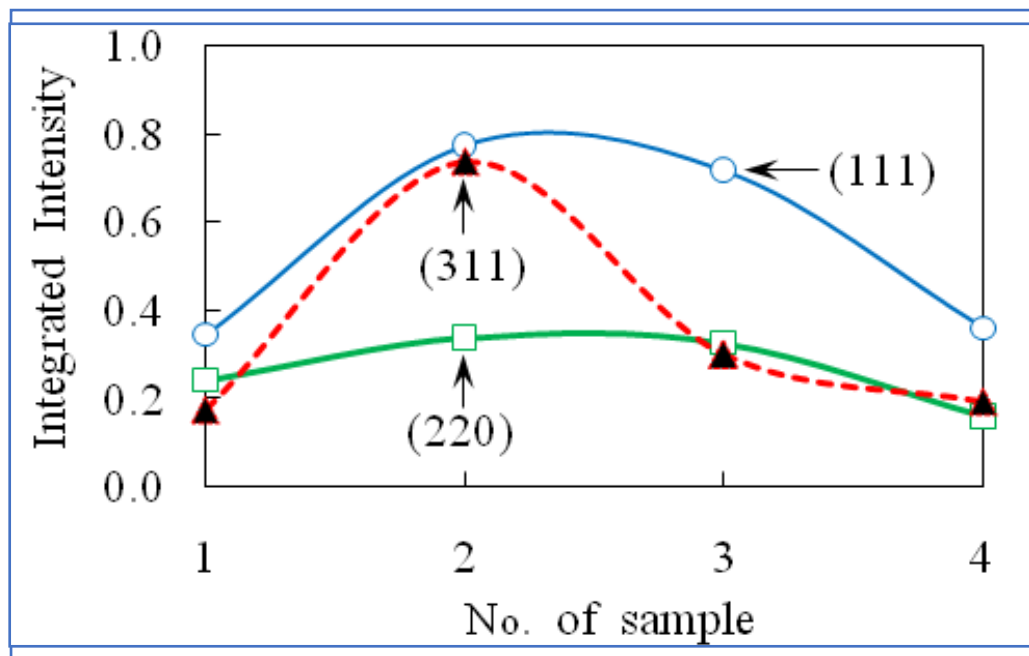
where  $\varepsilon$  is the average size (nm);  $R = 2.86$  cm is the camera radius;  $\lambda = 0.1540$  nm is the  $\text{CuK}_\alpha$ -radiation wavelength. X-ray line broadening  $\beta$  is defined by expression  $\beta = \sqrt{\beta_s \beta_w}$  where  $\beta_s = B - b$ ,  $\beta_w = \sqrt{B^2 - b^2}$ ,  $B$  is a half-width of X-ray line adjusted for doublet  $\text{CuK}_\alpha$  line,  $b$  is an instrumental component of  $B$ .

The average sizes of SiC nanocrystals in the (111), (220) and (311) planes were equal for samples: №1 – 3-7 nm; №2 – 3-4.5 nm; №3 – 2.6-3.7 nm; №4 – 4.4-6.2 nm, respectively. These SiC nanocrystals can become nuclei for the formation of large SiC crystals.

## Photographic X-ray diffraction

The sum of the integrated intensities of three (111), (220) and (311) lines for the samples №1-4 was 0.76, 1.84, 1.34 and 0.71, respectively, which indicates the intensive formation of SiC nanocrystals in samples № 2 and 3. The intensity of (311) line for samples №1, 3 and 4 is approximately half the intensity of (111) line. In contrast, a high value of integrated intensity of (311) line is characteristic for sample №2, indicating a 2-fold increase in the quantity of SiC nanocrystals oriented to reflection by (311) plane system. It presupposes the presence in the structure of sample №2 of a specific feature that is absent in other samples.

The substrate of sample №2 was not processed in an acid mixture HF: HNO<sub>3</sub> = 1 : 10 and retained many scratches and microcracks in the subsurface layer. Microcracks promote to the penetration of CO gas into the interior of the single crystal and the formation of SiC nanocrystals with a preferential orientation in the (311) direction.



**The integrated intensity of the (111), (220) and (311) lines for samples № 1 – 4.**

## 3.5 Studies by ellipsometry

Fig. 9 (a) – (d) show the dependences of the real  $\varepsilon_1$  and imaginary  $\varepsilon_2$  parts of the dielectric permittivity of SiC films for samples Nos. 1–4. According to the ellipsometric spectra, the SiC layer thicknesses are approximately equal to 95 nm for samples Nos. 1 and 2, 110 nm for sample No. 3, and 117 nm for sample No. 4. Using ellipsometric model was calculated [27] that the sample No. 1 contains about 8% Si vacancies, the sample No. 2 – only 5%, No. 3 and 4 – about 6.5%. In Si volume, sample No. 4 contains ~50% pores from the whole film volume.

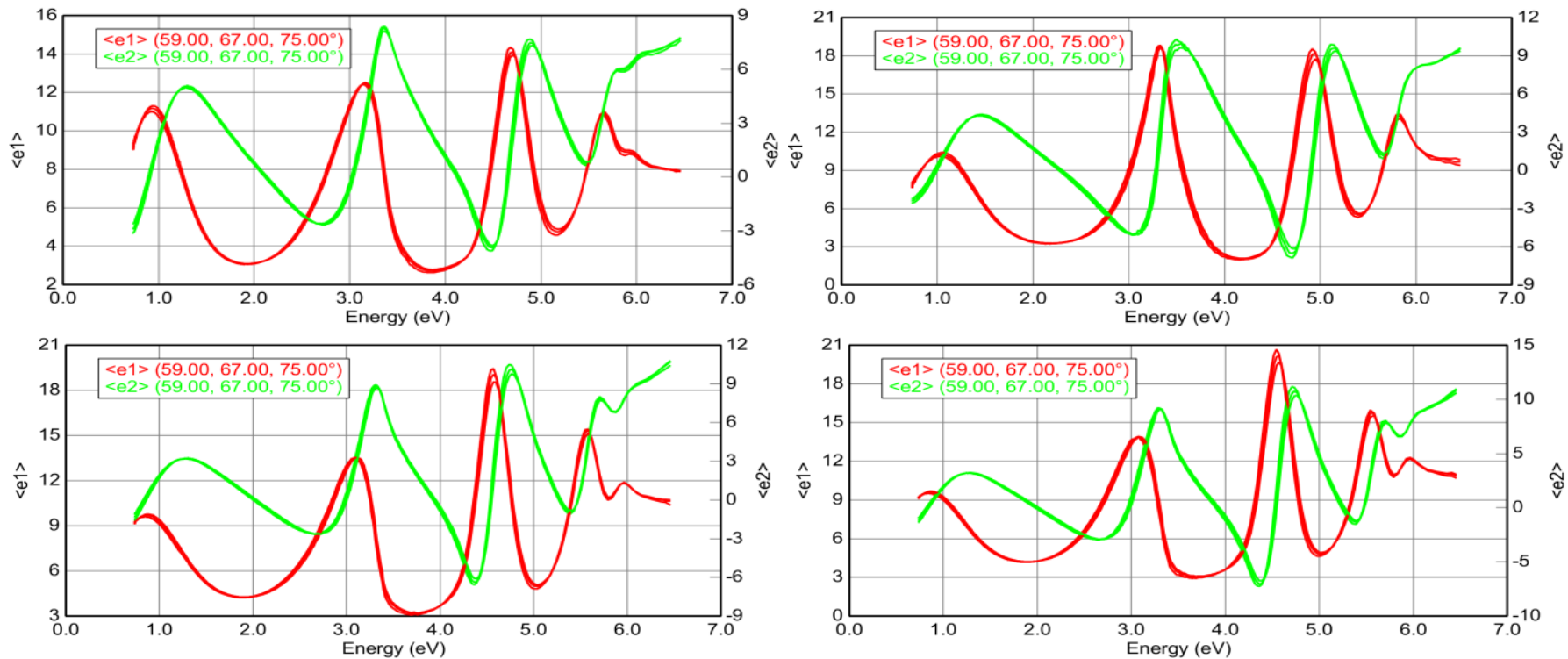
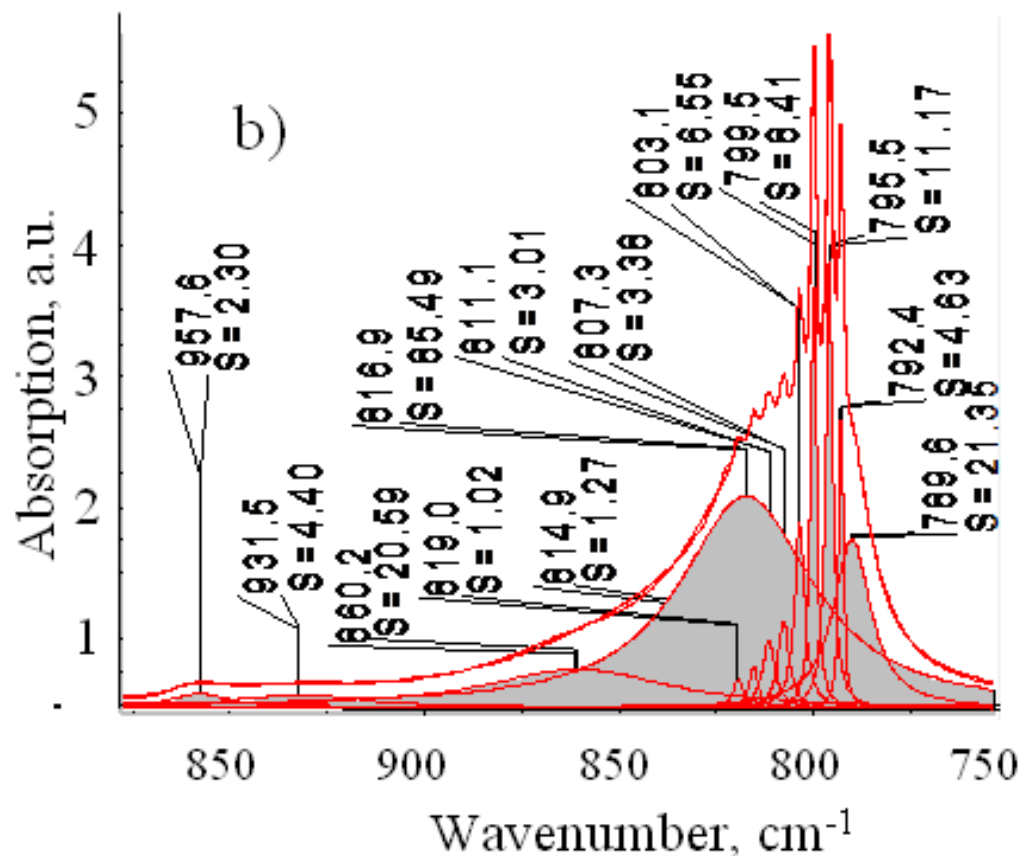


Fig. 9. Dependences of real  $\varepsilon_1$  and imaginary  $\varepsilon_2$  parts of the dielectric permittivity of SiC/Si(111) films from the photon energy for samples (a) No. 1, (b) No. 2, (c) No. 3 and (d) No. 4.

### 3.6 Studies by IR spectroscopy

IR absorption spectra of SiC films were received. SiC peak was decomposed into components (Fig. 10), their area and position in the spectrum were determined. Intense peaks at  $795.7\text{ cm}^{-1}$ ,  $795.5\text{ cm}^{-1}$ ,  $795.7\text{ cm}^{-1}$ ,  $796.0\text{ cm}^{-1}$  are observed in the IR spectra of samples Nos. 1, 2, 3 and 4, attributed to the single crystalline 3C-SiC phase.

The theoretical values of the infrared absorption peaks for the cubic, hexagonal and orthorhombic modifications are as follows:  $795.9\text{ cm}^{-1}$  for  $\beta$ -SiC (3C-SiC),  $799.5\text{ cm}^{-1}$  for 2H-SiC,  $797.6\text{ cm}^{-1}$  for 4H-SiC,  $797.0\text{ cm}^{-1}$  for 6H-SiC,  $797.5\text{ cm}^{-1}$  for 15R-SiC [28].



**Fig.10.** Mathematical decomposition of IR absorption spectrum of SiC films (a) No. 1 and (b) No.2 synthesized at the temperature of  $1250\text{ }^{\circ}\text{C}$  and the pressure of  $264\text{ Pa}$ ; SiC films (c) No. 3 and (d) No. 4 synthesized at  $1330\text{ }^{\circ}\text{C}$  and  $395\text{ Pa}$  (S – area of components)



### 3.6 Studies by IR spectroscopy

So, it can be affirmed that single crystalline cubic polytype 3C-SiC as the main crystalline phase of silicon carbide in the samples Nos. 1–4 is presented. The peaks corresponding to values  $799.1 \text{ cm}^{-1}$  (sample No. 1),  $799.5 \text{ cm}^{-1}$  (No. 2),  $799.7 \text{ cm}^{-1}$  (No. 3) and  $799.4 \text{ cm}^{-1}$  (No. 4) indicate the presence of a rare hexagonal phase 2H-SiC. It should be noted that the peaks of 3C-SiC and 2H-SiC are narrow (Fig. 10). This clearly indicates the crystalline perfection of SiC layers of different polytypes.

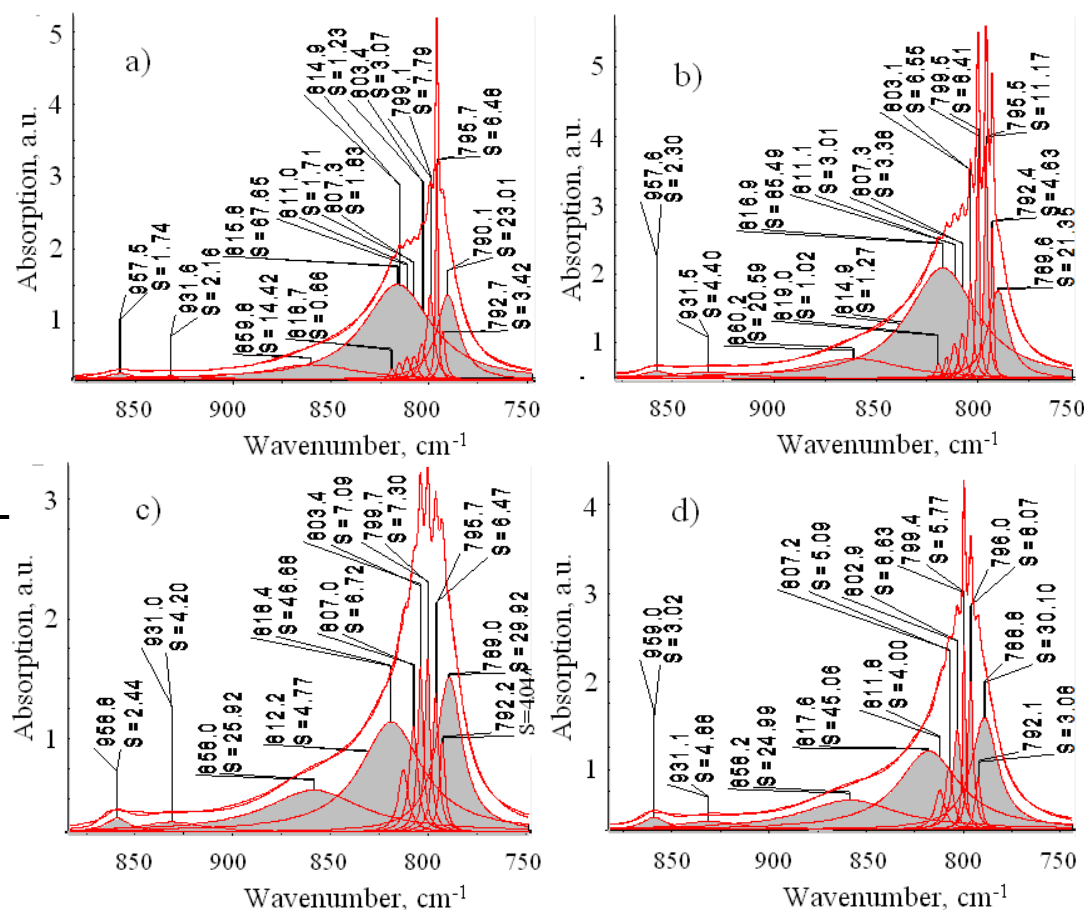
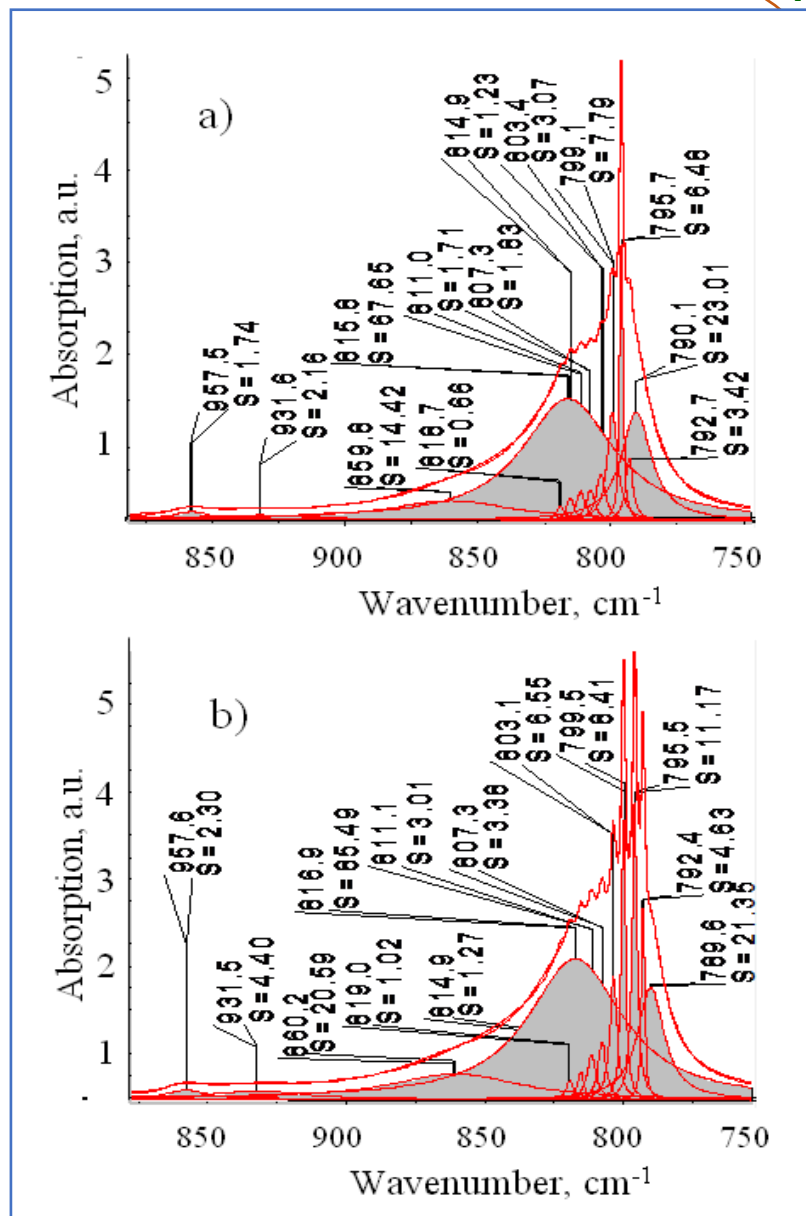


**Fig.10.** Mathematical decomposition of IR absorption spectrum of SiC films (a) No. 1 and (b) No.2 synthesized at the temperature of  $1250 \text{ }^{\circ}\text{C}$  and the pressure of  $264 \text{ Pa}$ ; SiC films (c) No. 3 and (d) No. 4 synthesized at  $1330 \text{ }^{\circ}\text{C}$  and  $395 \text{ Pa}$  ( $S$  – area of components)

# IR spectroscopy

In spectra of samples № 1-4, components with maxima at  $790.1\text{ cm}^{-1}$ ,  $789.6\text{ cm}^{-1}$ ,  $789.0\text{ cm}^{-1}$  and  $788.8\text{ cm}^{-1}$ , respectively, were attributed to Si–C-bonds in defective nanocrystals. Indeed, at the study of amorphous ion synthesized layers of SiC, the position of the SiC-peak was within  $700\text{--}760\text{ cm}^{-1}$ . After annealing ( $900\text{ }^{\circ}\text{C}$ ), the peak is shifted to  $\sim 795\text{--}800\text{ cm}^{-1}$ , narrows and increases its amplitude, indicating the prevalence of the tetrahedral oriented Si-C-bonds of polycrystalline SiC.

The sample №1 has a series of narrow peaks with frequencies  $803.4\text{ cm}^{-1}$ ,  $807.3\text{ cm}^{-1}$ ,  $811.0\text{ cm}^{-1}$ ,  $814.9\text{ cm}^{-1}$ ,  $818.7\text{ cm}^{-1}$ , which could appear due to the absorption by small nanocrystals. Indeed, H. Mutschke et.al note that a broad peak in the region  $11.3\text{ }\mu\text{m}$  ( $\sim 885\text{ cm}^{-1}$ ) was interpreted by various authors as the emission of small SiC particles between the frequencies of transverse ( $\sim 795\text{ cm}^{-1}$ ) and longitudinal ( $\sim 960\text{ cm}^{-1}$ ) optical phonons. So, sharp peaks in the range  $803\text{--}819\text{ cm}^{-1}$  may indicate the presence of groups of small SiC nanocrystals that differ in size.



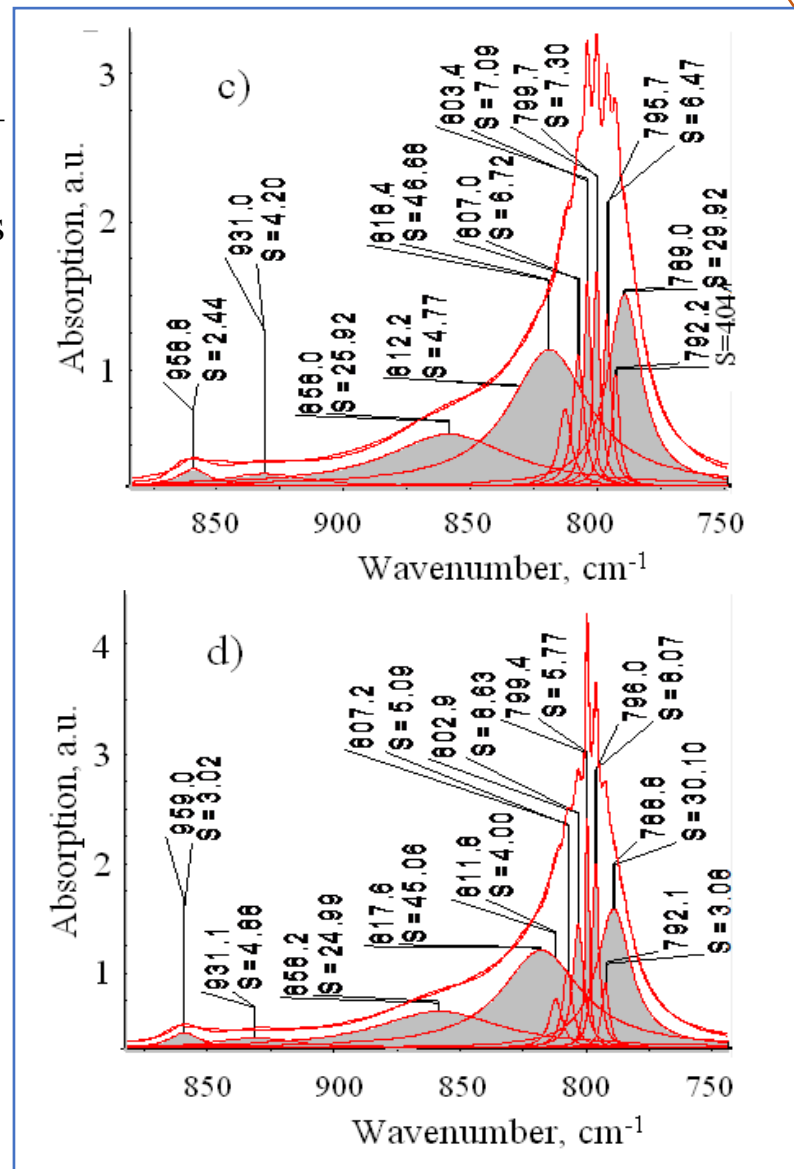
**Mathematical decomposition of IR absorption spectrum of SiC films (a) №1 and (b) №2 synthesized at the T of  $1250\text{ }^{\circ}\text{C}$  and the P of  $264\text{ Pa}$ ; (S – area of components)**

# IR spectroscopy

There is also a Gaussian peak with a maximum at frequency of  $815.8 \text{ cm}^{-1}$ , which can be attributed to Si-C-bonds on the surface of very small SiC nanocrystals of wide range sizes with the prevalence of nanocrystals absorbing at  $815.8 \text{ cm}^{-1}$ . These nanocrystals can be arranged on the both interface "SiC film-substrate" and inside the silicon substrate, covering the inner surface of the pores. Sample №2 shows a similar structure with small shift of component maxima.

For films №3 and №4 grown at  $1330^\circ\text{C}$  and  $395 \text{ Pa}$  of CO gas, some of the components, which maxima exceeds  $803 \text{ cm}^{-1}$ , became broader and have large areas, and, conversely, a broad peak at  $\sim 818 \text{ cm}^{-1}$  has a smaller area. This indicates an influence of synthesis condition on the formation of groups of the SiC nanocrystals of different sizes. Range  $818\text{--}959 \text{ cm}^{-1}$  can be attributed to a shorter Si-C-bonds between atoms in SiC nanocrystals and nanoclusters.

The peak with maximum in range  $957.5 \text{ cm}^{-1} - 959.0 \text{ cm}^{-1}$  is presented in spectra of all samples, and corresponds to the mechanical bond of the elastic dilatation dipole oscillation energy ( $\text{C-V}_{\text{Si}}$ ).



**Mathematical decomposition of IR absorption spectrum of SiC films (c) №3 and (d) №4 synthesized at  $1330^\circ\text{C}$  and  $395 \text{ Pa}$  (S – area of components)**

**IR spectroscopy.** The S areas of thirteen SiC peak components at wave numbers  $w$  for the IR spectra of SiC №1-4 films subjected to mathematical decomposition.

№	SiC №1			SiC №2			SiC №3			SiC №4		
T, °C	1250°C, 264 Па			1250°C, 264 Па			1330°C, 395 Па			1330°C, 395 Па		
Parameter	$w$ , cm <sup>-1</sup>	S, a.u.	S, %	$w$ , cm <sup>-1</sup>	S, a.u.	S, %	$w$ , cm <sup>-1</sup>	S, a.u.	S, %	$w$ , cm <sup>-1</sup>	S, a.u.	S, %
The SiC peak components	957.5	1.74	1.29	957.6	2.30	1.33	958.8	2.44	1.68	959.0	3.02	2.12
	931.6	2.16	1.60	931.5	4.40	2.54	931.0	4.20	2.89	931.1	4.88	3.42
	859.8	14.42	10.67	860.2	20.59	11.85	858.0	25.92	17.81	858.2	24.99	17.51
	818.7	0.66	0.49	819.0	1.02	0.59	-	-	-	-	-	-
	815.8	67.65	50.05	816.9	85.49	49.25	818.4	46.68	32.07	817.6	45.06	31.58
	814.9	1.23	0.91	814.9	1.27	0.73	-	-	-	-	-	-
	811.0	1.71	1.27	811.1	3.01	1.73	812.2	4.77	3.28	811.8	4.00	2.80
	807.3	1.83	1.35	807.3	3.38	1.95	807.0	6.72	4.62	807.2	5.09	3.57
	803.4	3.07	2.27	803.1	6.55	3.77	803.4	7.09	4.87	802.9	8.63	6.05
	799.1	7.79	5.76	799.5	8.41	4.85	799.7	7.30	5.02	799.4	5.77	4.04
	795.7	6.48	4.79	795.5	11.17	6.44	795.7	6.47	4.45	796.0	8.07	5.66
	792.7	3.42	2.53	792.4	4.63	2.67	792.2	4.04	2.78	792.1	3.08	2.16
	790.1	23.01	17.02	789.6	21.35	12.30	789.0	29.92	20.56	788.8	30.10	21.09
ΣS	135.17	100.0	ΣS	173.57	100.0	ΣS	145.55	100.0	ΣS	142.69	100.0	

**The SiC peak of sample No. 2 has maximum area S = 173 a.u.** The substrate of sample №2 was not processed in an acid mixture HF: HNO<sub>3</sub> = 1 : 10 and retained many scratches and microcracks in the subsurface layer. Microcracks promote to the penetration of CO gas into the interior of the single crystal and the formation of SiC nanocrystals.

# IR spectroscopy

**Basing on the areas of the SiC peak components for films №1–4, the volumes (%) of SiC crystalline phase and cluster structures were determined.**

Nos.	Types of bonds	SiC №1	SiC №2	SiC №3	SiC №4
A	Close to the tetrahedral Si-C-bond of the crystalline phase, %	13.09	13.95	12.24	11.86
B	Shortened Si-C-bond on the surface of nanocrystals, %	56.34	58.03	44.84	44.00
C	Extended Si-C bond in small defective nanocrystals, %	17.02	12.30	20.56	21.09
D	Shortened Si-C- bonds between atoms in nanoclusters, %	13.55	15.72	22.37	23.05
A+B	Crystalline phase, %	69.42	71.98	57.07	55.86
C+D	Clusters and small defective nanocrystals, %	30.58	28.02	42.93	44.14
	Total, %	100.0	100.0	100.0	100.0

The proportion of the crystalline phase of silicon carbide, reflecting the degree of crystallinity of the film, was in the range of 55 – 72 %.

It has been established that the highest content of crystalline phases of SiC and the most perfect structure are characteristic of film № 2.



## X-ray reflectometry

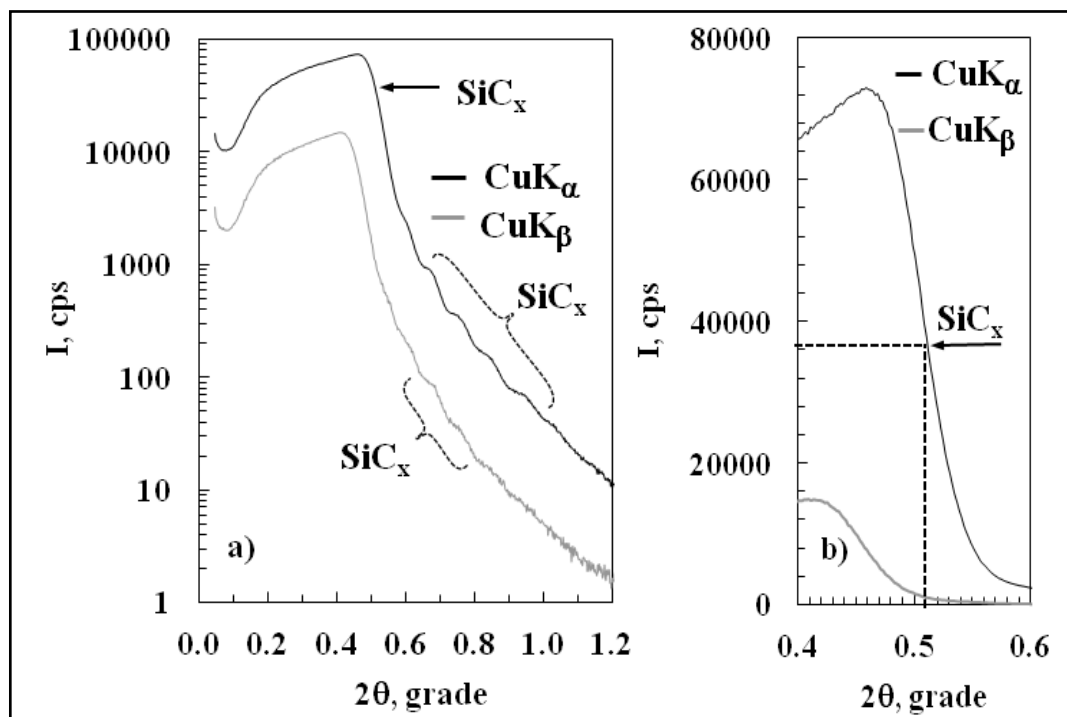
All of samples Nos. 1 – 4 by X-ray reflectometry was measured (Fig. 11). Because of the blurred interface "film-substrate", maxima had low amplitude, making it difficult to analyze the SiC layers. For all samples, except sample № 2, the intensity oscillations attributed to the interference of X-ray reflections in SiC<sub>x</sub> layer, where  $x = N_C/N_{Si}$  is the ratio of concentrations of carbon and silicon atoms [14], were found. If  $x = 1$ , i.e. SiC<sub>x</sub> = SiC<sub>1</sub>, it is a stoichiometric silicon carbide. If  $x = 0$ , i.e. SiC<sub>x</sub> = SiC<sub>0</sub> = Si, then the substance is pure silicon.

**Table 5 - Determination of the density of the SiC<sub>x</sub> layer of sample № 1 according to Henke program**

Film	$I_{\max}$ , c <sup>-1</sup>	$I_{\max}/2$ , c <sup>-1</sup>	$2\theta_c$ , grade	$\theta_c$ , grade	$\theta_c$ , mrad	$\rho$ , g/cm <sup>3</sup>
SiC <sub>x</sub>	72926	36463	0,511	0,2555	4,459	3,069

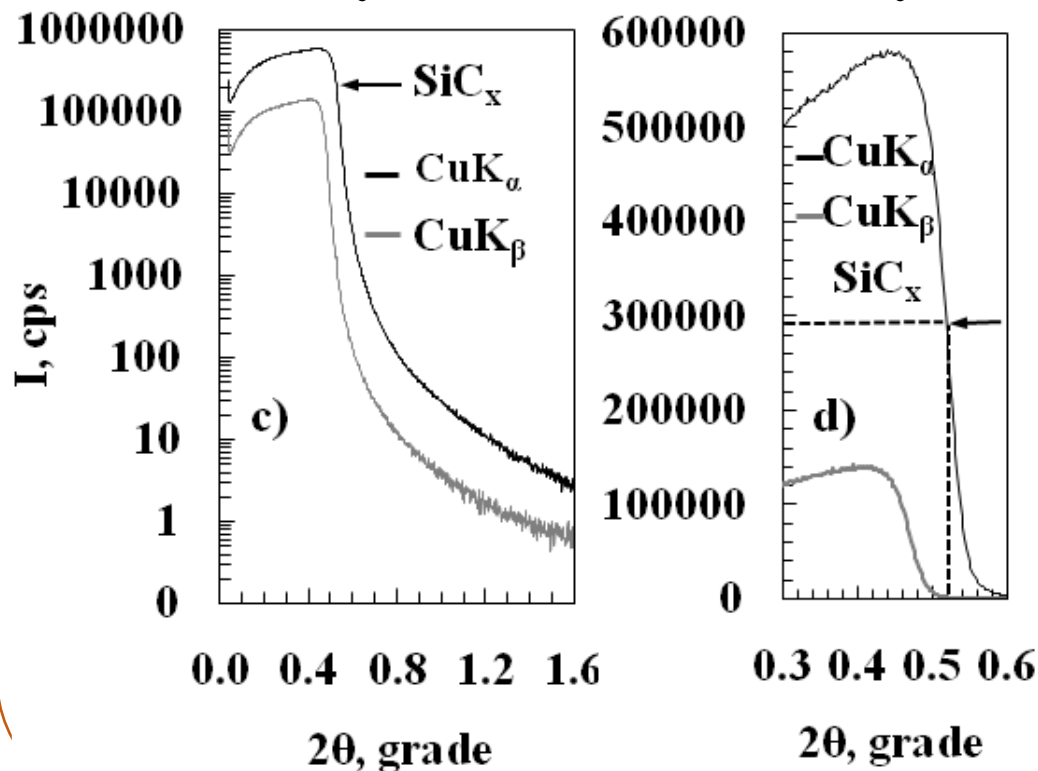
For reflectogram of sample № 1, the main reflection peak with intensity  $I_1 = 72926$  pulses is observed at angle  $2\theta = 0.458^\circ$ . Angle of total external reflection was determined as an angle where intensity of reflection is equal to half of the main peak  $I = I_1/2 = 36463$  pulses, i.e.  $2\theta_c = 0.511^\circ$  (Fig. 11 (b)), or  $\theta_c = 0.2555^\circ = 4.459$  mrad, which corresponds to  $\rho = 3.069$  g/cm<sup>3</sup>.

**Fig.11a,b. X-ray reflectometry using two spectral lines CuK<sub>α</sub> (0.154 nm) and CuK<sub>β</sub> (0.139 nm) for Si<sub>y</sub>C film of samples № 1, in (a) logarithmic and (b) natural scales.**



## X-ray reflectometry

At reflectogram of sample № 2, the intensity oscillations (Fig. 11 (c)) are absent. The increase of main peak intensity by 8 times ( $I_2 = 581448$  pulses) caused by decrease in average roughness on large areas of irradiated surface, as was shown in section 3.2. The angle of total external reflection corresponding to  $I_2/2 = 290724$  pulses is equal to  $2\theta_c = 0.519^\circ$  (Fig. 11 (d)), or  $\theta_c = 0.25965^\circ = \mathbf{4.532 \text{ mrad}}$ . In reflectogram of samples №3 and 4, the intensity oscillations again revealed (Fig. 11 (e), (g)). The main reflection peak has intensity  $I_3 = 147030$  pulses. Angle of total external reflection was  $2\theta_c = 0.525^\circ$  (Fig. 11 (f)), or  $\theta_c = 0.2625^\circ = \mathbf{4.581 \text{ mrad}}$ . Main reflection peak for sample No. 4 (Fig. 11 (g)) has intensity  $I_4 = 97629$  pulses;  $2\theta_c = 0.529^\circ$  (Fig. 11 (h)), or  $\theta_c = 0.2647^\circ = \mathbf{4.620 \text{ mrad}}$ .



Henke program [33] allows determining the density of the film from value of the critical angle  $\theta_s$ . For  $\text{SiC}_x$  film on sample No. 1 was found, that the value  $\theta_c = 4.459 \text{ mrad}$  corresponds to the density value  $\mathbf{3.069 \text{ g/cm}^3}$ . The density of  $\text{SiC}_x$  layer on the sample № 2 was  $\mathbf{3.17 \text{ g/cm}^3}$ , on the sample № 3 –  $\mathbf{3.233 \text{ g/cm}^3}$ , on the sample № 4 –  $\mathbf{3.29 \text{ g/cm}^3}$ , respectively.

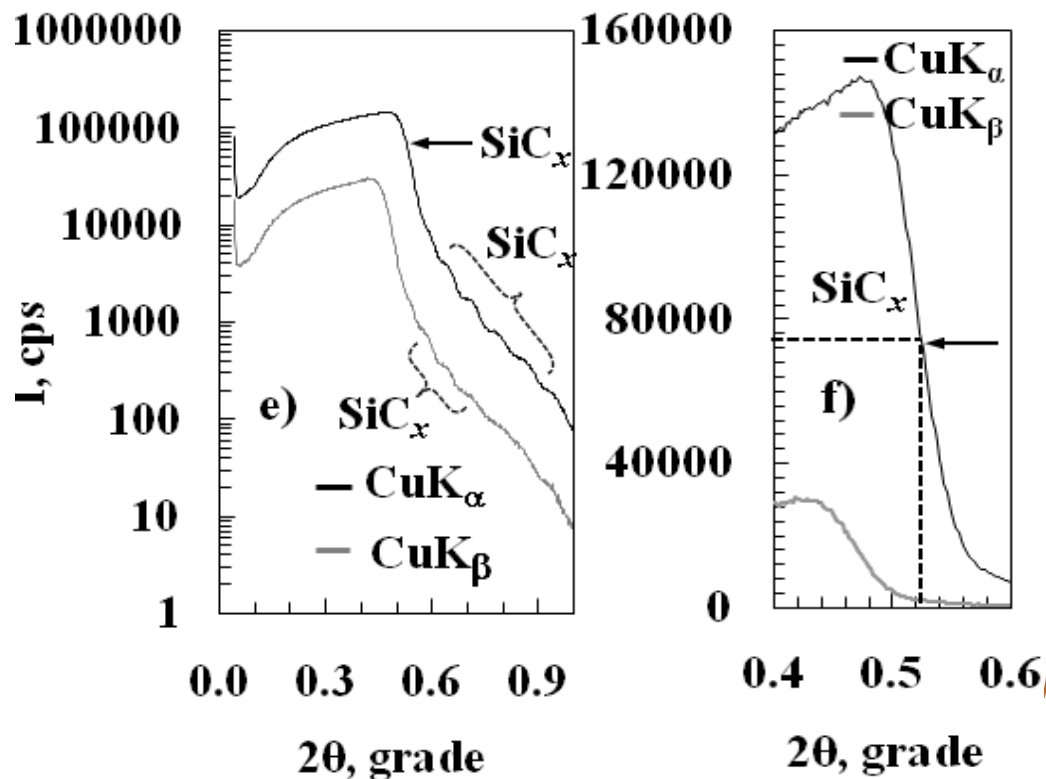
Fig. 11c,d. X-ray reflectometry using two spectral lines  $\text{CuK}_\alpha$  (0.154 nm) and  $\text{CuK}_\beta$  (0.139 nm) for  $\text{Si}_y\text{C}$  film of samples № 2, in (c) logarithmic and (d) natural scales.

## X-ray reflectometry

Basing on these data, the composition of  $\text{SiC}_x$  layer is defined. The process of Si atoms substitution onto C atoms in the silicon substrate takes place in several stages, during which the intermediate phases are formed containing silicon vacancy and carbon atom in the Si interstitial space. These phases have less dense crystal lattice than the  $\text{SiC}$ . In this regard, the composition determination of layers by the density measurement can lead to ambiguous or even incorrect results. Therefore, ellipsometry method is attracted for determination of the  $\text{SiC}$  layers composition. Thickness of the  $\text{SiC}$  layers approximately is: № 1 – 95.0 nm, № 2 – 95.0 nm, № 3 – 110 nm, № 4 – 117 nm. Samples Nos. 1 – 4 contain 5 - 8% of Si vacancies. These data allow suggesting that the low value of the density of the sample No.1 is associated

to a high concentration of silicon vacancies. At their excessively high concentration, carbon may be present as the second phase. Thus, in the case of  $\text{SiC}$  film, containing Si vacancies, should instead of formula  $\text{SiC}_x$  be write formula  $\text{Si}_y\text{C}$  ( $y = N_{\text{Si}}/N_{\text{C}}$ ), in which the variable value is the content of silicon.

Fig. 11e,f. X-ray reflectometry using two spectral lines  $\text{CuK}_\alpha$  (0.154 nm) and  $\text{CuK}_\beta$  (0.139 nm) for  $\text{Si}_y\text{C}$  film of samples № 2, in (c) logarithmic and (d) natural scales.



## X-ray reflectometry

The composition of  $\text{Si}_y\text{C}$  layers can be approximately determined from the proportion (3):

$$\frac{y - y_1}{\rho_y - \rho_1} = \frac{y_2 - y_1}{\rho_2 - \rho_1} \quad (3)$$

where  $\rho_2 = 3.21 \text{ g/cm}^3$  is the density of stoichiometric SiC layer,  $y_1 = 0$ ,  $y_2 = 1$ ,  $\rho_y = 3.069 \text{ g/cm}^3$ , and  $\rho_1 = 2.23 \text{ g/cm}^3$  is the graphite density. Hence  $y = y_1 + (y_2 - y_1)(\rho_y - \rho_1)/(\rho_2 - \rho_1) = 0.856$ , i.e. on 100 carbon atoms accounted 86 silicon atoms and  $\text{Si}_y\text{C} = \text{Si}_{0.856}\text{C}$ . The formula  $\text{Si}_{0.856}\text{C}$  can be rewrite through percentage ratios between Si and C atoms –  $\text{Si}_z\text{C}_{1-z}$ . Coefficients  $y$  and  $z$  are interrelated by expression  $\text{Si}_y\text{C}_1 = \text{Si}_{1-z}\text{C}_z$ . Hence  $y/1 = (1-z)/z \rightarrow 1-z = yz, \rightarrow 1 = z(1+y) \rightarrow z = 1/(1+y)$ . Then  $\text{Si}_y\text{C} = \text{Si}_{1-z}\text{C}_z = \text{Si}_{1-1/(1+y)}\text{C}_{1/(1+y)}$ , and:

$$\text{Si}_y\text{C} = \text{Si}_{y/(1+y)}\text{C}_{1/(1+y)}, \quad (4)$$

Hence we have,  $\text{Si}_{0.856}\text{C} = \text{Si}_{0.46}\text{C}_{0.54}$ , i.e. content of Si and C atoms in the sample № 1 is 46% and 54%, respectively. For film  $\text{Si}_y\text{C}$  of sample № 2 with density  $\rho_x = 3.17 \text{ g/cm}^3$ , we obtain the composition  $\text{Si}_{0.96}\text{C} = \text{Si}_{0.49}\text{C}_{0.51}$ , which is very close to stoichiometric composition.

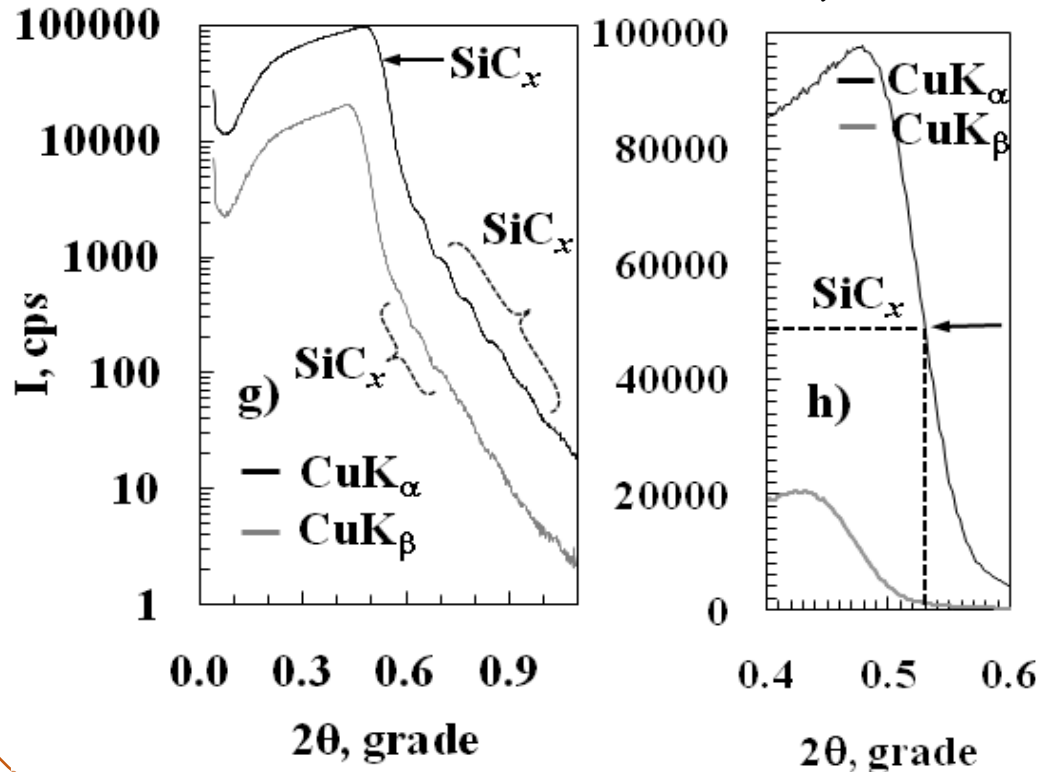


Fig. 11g,h. X-ray reflectometry using two spectral lines  $\text{CuK}\alpha$  (0.154 nm) and  $\text{CuK}\beta$  (0.139 nm) for  $\text{Si}_y\text{C}$  film of samples № 2, in (c) logarithmic and (d) natural scales.

## X-ray reflectometry

Density values of the films Nos. 3 and 4 are greater than density of stoichiometric SiC (3.21 g/cm<sup>3</sup>) and suggest the presence of more dense structures, such as carbon in a diamond condition (3.51 g/cm<sup>3</sup>) or in strong carbon clusters, containing multiple bonds and having a high density [11,35].

The layer composition is written in the form Si<sub>y</sub>C, where Si<sub>1</sub>C corresponds to stoichiometric silicon carbide, and Si<sub>0</sub>C = C – to diamond. From proportion similar to (3), where  $y_1 = 1$ ,  $y_2 = 0$ ,  $\rho_2 = 3.51$  g/cm<sup>3</sup>,  $\rho_1 = 3.21$  g/cm<sup>3</sup>,  $\rho_y = 3.233$  g/cm<sup>3</sup>, for sample No. 3 was obtained the value of  $y = y_1 + (y_2 - y_1)(\rho_y - \rho_1)/(\rho_2 - \rho_1) = 0.923$  and the composition of the film Si<sub>y</sub>C = Si<sub>0.923</sub>C. Since the density of the layer is high (3.233 g/cm<sup>3</sup>), then the concentration of silicon vacancies in the upper part of the film is low. On average, 8 excess carbon atoms account for 92 SiC molecules.

Accordingly (4), composition of layer No. 3 can be written: Si<sub>0.923</sub>C = Si<sub>0.480</sub>C<sub>0.520</sub>. Similar formula for sample No. 4 will look Si<sub>0.733</sub>C = Si<sub>0.423</sub>C<sub>0.577</sub>. The presence of carbon nanoclusters can be also expected in this sample.

To evaluate the thickness of Si<sub>y</sub>C film № 1, we used the formula  $2d \cdot \sin\theta = \lambda$ , where  $\lambda$  is the wavelength of the CuK<sub>α</sub> (0.154 nm) and CuK<sub>β</sub> (0.139 nm) radiation, and  $2\theta = (0.998 - 0.644)/4 = 0.0885^\circ = 1.545$  mrad is the average distance between the peak minima (Fig. 11). For small  $\theta$  angles,  $\sin\theta \approx \theta$ , so  $d = \lambda/2\theta$  nm. The Si<sub>y</sub>C layer thickness of the sample № 1 was ~ 99.8 nm, and by two peaks of CuK<sub>β</sub>-radiation ~ 98.5 nm. Thickness of the film on the sample № 2 was not determined due to the absence of oscillations (Fig. 11 (c)). The Si<sub>y</sub>C layer thickness of sample № 3 was equal to 122.7 nm (CuK<sub>α</sub>) and 124.6 nm (CuK<sub>β</sub>), i.e. ~124 nm. Thickness of Si<sub>y</sub>C layer of sample № 4 was evaluated ~115 nm.



## X-ray reflectometry

Mathematical simulation and analysis of the microscopic structure of film layers was carried out by using the Release program [10]. This made it possible to obtain model theoretical curves (Fig. 12) and compare them with the experimental X-ray reflectometry curves. The results of the SiC layers structure simulation are shown in Fig. 13. The curves coincide if SiC films Nos. 1 – 4 consist of five layers of different thickness, density and composition.

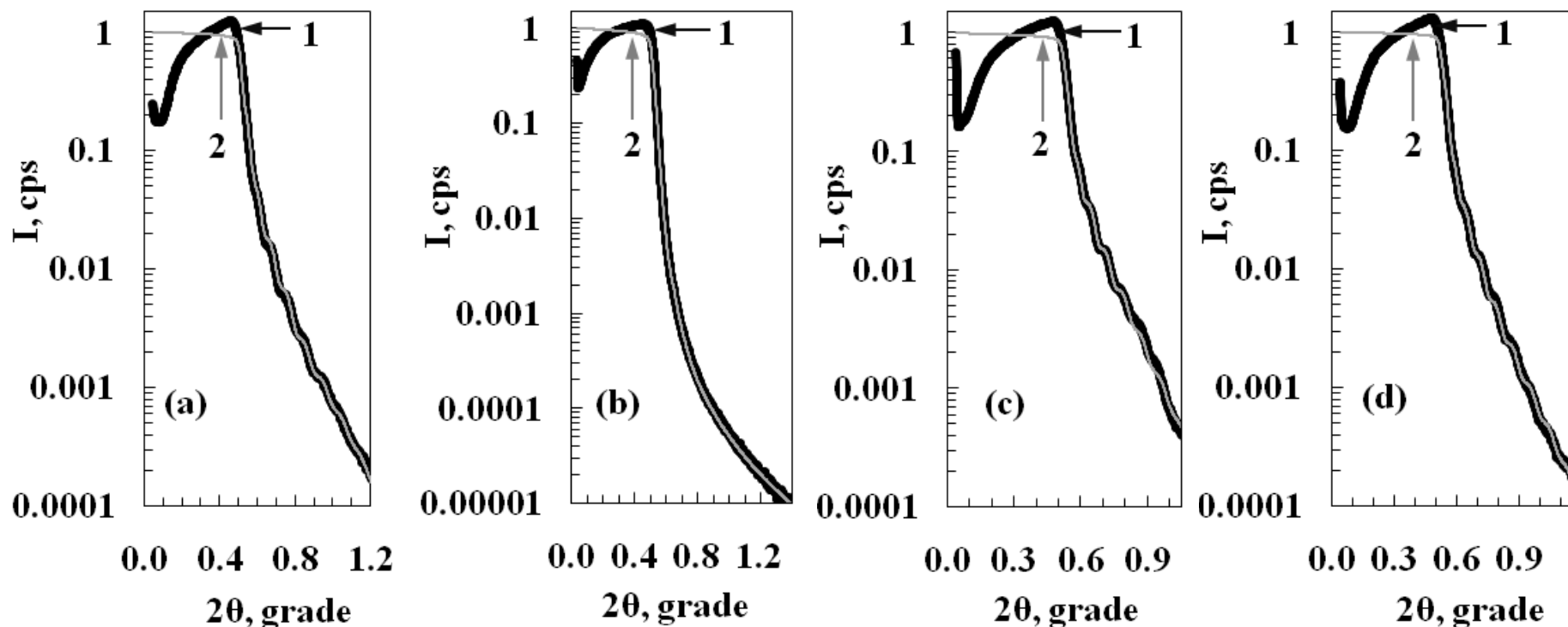


**Fig. 12.** Simulation of the X-ray reflectometry data by the Release program of the multilayer system  $\text{Si}_y\text{C}$  for samples (a) No. 1, (b) No. 2, (c) No. 3, (d) No. 4: 1 – experimental curve, 2 – theoretical curve.

## X-ray reflectometry

The thin SiC layer 1 in all samples, except sample No. 2, has a low density and is may be enriched by carbon and silicon vacancies, through which the X-ray passes under grazing angle. The low average density of this layer may be due to the etch pits. The surface of sample №2, which was not pre-treated with etching acids, is the closest in composition to SiC. Layer 2 has the highest density and is closest in composition to SiC. Carbon content decreases in the layers 3 and 4. The density of these layers also decreases, being values below  $3.21 \text{ g/cm}^3$ , so the composition of layers is determined in the same way as for the films № 1 and 2.

<b>layer 1: SiC+Si<sub>vac</sub>(1.58 nm, 7.0 nm, 0.5 g/cm<sup>3</sup>)</b>	<b>layer 1: SiC+Si<sub>vac</sub>(6.19 nm, 3.0 nm, 2.91 g/cm<sup>3</sup>)</b>
<b>layer 2: Si<sub>0.86</sub>C(1.05nm, 25 nm, 3.07 g/cm<sup>3</sup>)</b>	<b>layer 2: Si<sub>0.96</sub>C(0 nm, 25 nm, 3.17 g/cm<sup>3</sup>)</b>
<b>layer 3: Si<sub>0.77</sub>C(2.0 nm, 30 nm, 2.98 g/cm<sup>3</sup>)</b>	<b>layer 3: Si<sub>0.69</sub>C(4.0 nm, 30 nm, 2.91 g/cm<sup>3</sup>)</b>
<b>layer 4: Si<sub>0.74</sub>C(2.0 nm, 7.5 nm, 2.95 g/cm<sup>3</sup>)</b>	<b>layer 4: Si<sub>0.65</sub>C(4.0 nm, 10.0 nm, 2.87 g/cm<sup>3</sup>)</b>
<b>layer 5: Si + voids (9.0 nm, 14 nm, 2.1 g/cm<sup>3</sup>)</b>	<b>layer 5: Si + voids (9.0 nm, 15 nm, 2.0 g/cm<sup>3</sup>)</b>
<b>(a) substrate: Si (1.5 nm, ∞, 2.33 g/cm<sup>3</sup>)</b>	<b>(b) substrate: Si (4.0 nm, ∞, 2.33 g/cm<sup>3</sup>)</b>
<b>layer 1: SiC+Si<sub>vac</sub>(2.95 nm, 9.4 nm, 0.6 g/cm<sup>3</sup>)</b>	<b>layer 1: SiC+Si<sub>vac</sub>(1.77 nm, 7.3 nm, 0.4 g/cm<sup>3</sup>)</b>
<b>layer 2: Si<sub>0.92</sub>C (1.0 nm, 34 nm, 3.23 g/cm<sup>3</sup>)</b>	<b>layer 2: Si<sub>0.73</sub>C (1.17 nm, 30 nm, 3.29 g/cm<sup>3</sup>)</b>
<b>layer 3: Si<sub>0.80</sub>C(5.0 nm, 27 nm, 3.01 g/cm<sup>3</sup>)</b>	<b>layer 3: Si<sub>0.84</sub>C(4.0 nm, 37 nm, 3.05 g/cm<sup>3</sup>)</b>
<b>layer 4: Si<sub>0.63</sub>C(4.0 nm, 10.0 nm, 2.85 g/cm<sup>3</sup>)</b>	<b>layer 4: Si<sub>0.69</sub>C(4.0 nm, 6.0 nm, 2.91 g/cm<sup>3</sup>)</b>
<b>layer 5: Si + voids (9.5 nm, 15 nm, 2.0 g/cm<sup>3</sup>)</b>	<b>layer 5: Si + voids(9.0 nm, 14 nm, 2.11 g/cm<sup>3</sup>)</b>
<b>(c) substrate: Si (1.6 nm, ∞, 2.33 g/cm<sup>3</sup>)</b>	<b>(d) substrate: Si (1.4 nm, ∞, 2.33 g/cm<sup>3</sup>)</b>

**Fig. 13.** Model of multilayer structure of samples (a) No. 1, (b) No. 2, (c) No. 3, (d) No. 4, calculated on basis of experimental data using the Release program [10]; the values of the layer surface roughness (nm), thickness (nm) and density ( $\text{g/cm}^3$ ) are given in parentheses.

## X-ray reflectometry

The fifth layer of low density is porous silicon covered with the SiC film [2]. As synthesis temperature increases, the thickness and density of the layer 2 + layer 3 zone (films Nos. 3 and 4) increases. In sample No. 4, intensive carburizing processes led to a decrease the proportion of silicon atoms and an intensive release of carbon into nanoclusters of increased density in layer 2. This caused an intensive formation of SiC in the layer adjacent to substrate. This can be accompanied by intensive pore formation, as evidenced by ellipsometry data.

layer 1: SiC+Si <sub>vac</sub> (1.58 nm, 7.0 nm, 0.5 g/cm <sup>3</sup> )
layer 2: Si <sub>0.86</sub> C(1.05nm, 25 nm, 3.07 g/cm <sup>3</sup> )
layer 3: Si <sub>0.77</sub> C(2.0 nm, 30 nm, 2.98 g/cm <sup>3</sup> )
layer 4: Si <sub>0.74</sub> C(2.0 nm, 7.5 nm, 2.95 g/cm <sup>3</sup> )
layer 5: Si + voids (9.0 nm, 14 nm, 2.1 g/cm <sup>3</sup> )
(a) substrate: Si (1.5 nm, ∞, 2.33 g/cm <sup>3</sup> )

layer 1: SiC+Si <sub>vac</sub> (6.19 nm, 3.0 nm, 2.91 g/cm <sup>3</sup> )
layer 2: Si <sub>0.96</sub> C(0 nm, 25 nm, 3.17 g/cm <sup>3</sup> )
layer 3: Si <sub>0.69</sub> C(4.0 nm, 30 nm, 2.91 g/cm <sup>3</sup> )
layer 4: Si <sub>0.65</sub> C(4.0 nm, 10.0 nm, 2.87 g/cm <sup>3</sup> )
layer 5: Si + voids (9.0 nm, 15 nm, 2.0 g/cm <sup>3</sup> )
(b) substrate: Si (4.0 nm, ∞, 2.33 g/cm <sup>3</sup> )

layer 1: SiC+Si <sub>vac</sub> (2.95 nm, 9.4 nm, 0.6 g/cm <sup>3</sup> )
layer 2: Si <sub>0.92</sub> C (1.0 nm, 34 nm, 3.23 g/cm <sup>3</sup> )
layer 3: Si <sub>0.80</sub> C(5.0 nm, 27 nm, 3.01 g/cm <sup>3</sup> )
layer 4: Si <sub>0.63</sub> C(4.0 nm, 10.0 nm, 2.85 g/cm <sup>3</sup> )
layer 5: Si + voids (9.5 nm, 15 nm, 2.0 g/cm <sup>3</sup> )
(c) substrate: Si (1.6 nm, ∞, 2.33 g/cm <sup>3</sup> )

layer 1: SiC+Si <sub>vac</sub> (1.77 nm, 7.3 nm, 0.4 g/cm <sup>3</sup> )
layer 2: Si <sub>0.73</sub> C (1.17 nm, 30 nm, 3.29 g/cm <sup>3</sup> )
layer 3: Si <sub>0.84</sub> C(4.0 nm, 37 nm, 3.05 g/cm <sup>3</sup> )
layer 4: Si <sub>0.69</sub> C(4.0 nm, 6.0 nm, 2.91 g/cm <sup>3</sup> )
layer 5: Si + voids(9.0 nm, 14 nm, 2.11 g/cm <sup>3</sup> )
(d) substrate: Si (1.4 nm, ∞, 2.33 g/cm <sup>3</sup> )

## X-ray reflectometry

The theoretical and experimental curves coincide (Fig. 12), if the average roughnesses of the surface of the grown SiC films Nos. 1-4 coincide with the atomic force microscopy data for the average roughness of the areas with sizes of  $200 \times 200$  nm. Film No. 2 has the most perfect structure and composition closest to the stoichiometric  $\text{Si}_{0.959}\text{C} = \text{Si}_{0.49}\text{C}_{0.51}$ .

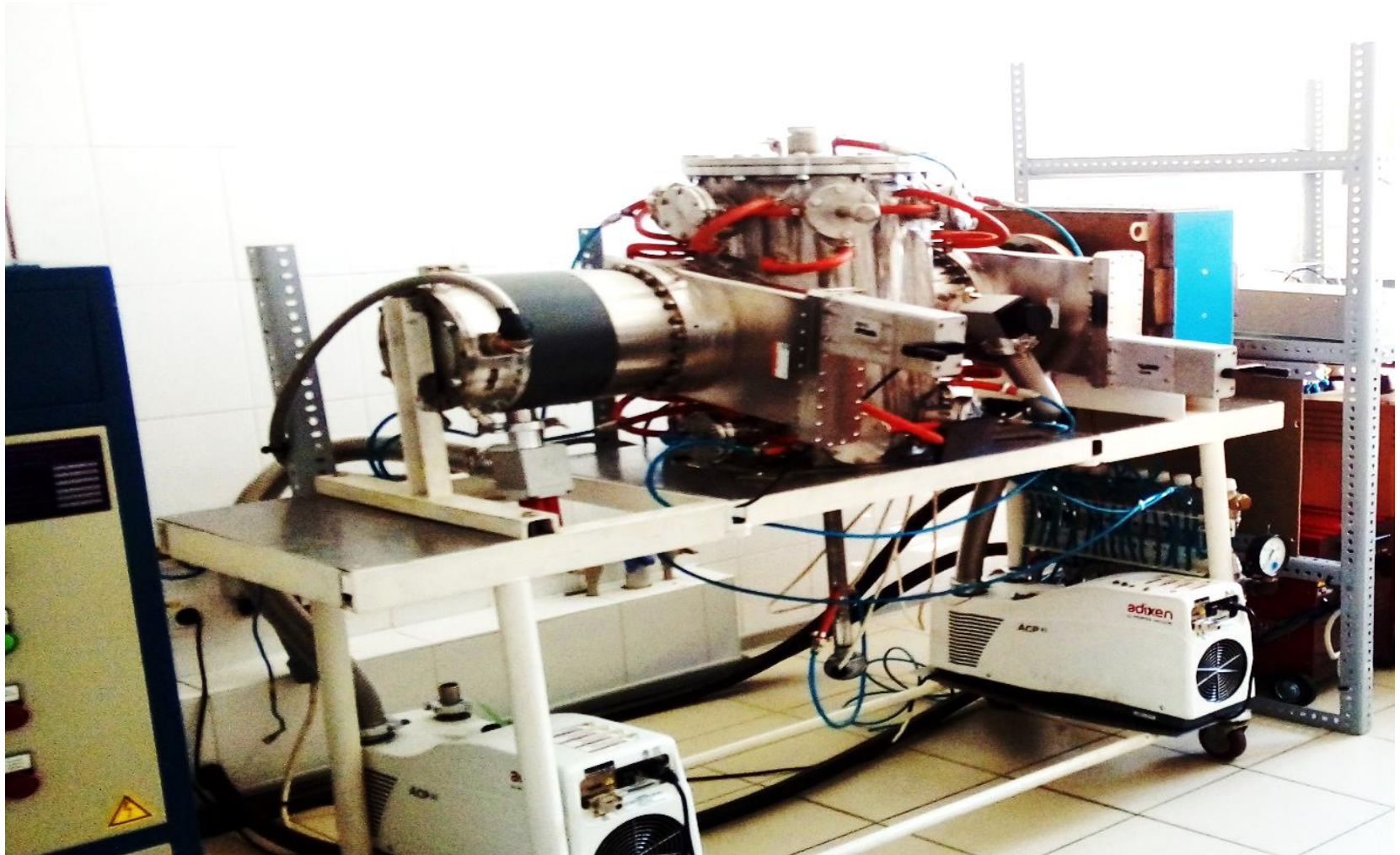
layer 1: $\text{SiC} + \text{Si}_{\text{vac}}$ (1.58 nm, 7.0 nm, 0.5 g/cm <sup>3</sup> )
layer 2: $\text{Si}_{0.86}\text{C}$ (1.05 nm, 25 nm, 3.07 g/cm <sup>3</sup> )
layer 3: $\text{Si}_{0.77}\text{C}$ (2.0 nm, 30 nm, 2.98 g/cm <sup>3</sup> )
layer 4: $\text{Si}_{0.74}\text{C}$ (2.0 nm, 7.5 nm, 2.95 g/cm <sup>3</sup> )
layer 5: Si + voids (9.0 nm, 14 nm, 2.1 g/cm <sup>3</sup> )
(a) substrate: Si (1.5 nm, $\infty$ , 2.33 g/cm <sup>3</sup> )

layer 1: $\text{SiC} + \text{Si}_{\text{vac}}$ (6.19 nm, 3.0 nm, 2.91 g/cm <sup>3</sup> )
layer 2: $\text{Si}_{0.96}\text{C}$ (0 nm, 25 nm, 3.17 g/cm <sup>3</sup> )
layer 3: $\text{Si}_{0.69}\text{C}$ (4.0 nm, 30 nm, 2.91 g/cm <sup>3</sup> )
layer 4: $\text{Si}_{0.65}\text{C}$ (4.0 nm, 10.0 nm, 2.87 g/cm <sup>3</sup> )
layer 5: Si + voids (9.0 nm, 15 nm, 2.0 g/cm <sup>3</sup> )
(b) substrate: Si (4.0 nm, $\infty$ , 2.33 g/cm <sup>3</sup> )

layer 1: $\text{SiC} + \text{Si}_{\text{vac}}$ (2.95 nm, 9.4 nm, 0.6 g/cm <sup>3</sup> )
layer 2: $\text{Si}_{0.92}\text{C}$ (1.0 nm, 34 nm, 3.23 g/cm <sup>3</sup> )
layer 3: $\text{Si}_{0.80}\text{C}$ (5.0 nm, 27 nm, 3.01 g/cm <sup>3</sup> )
layer 4: $\text{Si}_{0.63}\text{C}$ (4.0 nm, 10.0 nm, 2.85 g/cm <sup>3</sup> )
layer 5: Si + voids (9.5 nm, 15 nm, 2.0 g/cm <sup>3</sup> )
(c) substrate: Si (1.6 nm, $\infty$ , 2.33 g/cm <sup>3</sup> )

layer 1: $\text{SiC} + \text{Si}_{\text{vac}}$ (1.77 nm, 7.3 nm, 0.4 g/cm <sup>3</sup> )
layer 2: $\text{Si}_{0.73}\text{C}$ (1.17 nm, 30 nm, 3.29 g/cm <sup>3</sup> )
layer 3: $\text{Si}_{0.84}\text{C}$ (4.0 nm, 37 nm, 3.05 g/cm <sup>3</sup> )
layer 4: $\text{Si}_{0.69}\text{C}$ (4.0 nm, 6.0 nm, 2.91 g/cm <sup>3</sup> )
layer 5: Si + voids (9.0 nm, 14 nm, 2.11 g/cm <sup>3</sup> )
(d) substrate: Si (1.4 nm, $\infty$ , 2.33 g/cm <sup>3</sup> )

To synthesize epitaxial SiC films, we used polished single-crystal silicon wafers of the (100) orientation, 7–7–0.3 mm in size and with a resistivity of 4–5 Ohm·cm [7, 10]. The synthesis of SiC films was carried out in a special electric furnace [11] at a temperature of 1250 °C and 1350°C for 20 minutes in a CO gas flow at a pressure of 0.8 Pa.





## Synthesis of SiC films by the atom substitution method

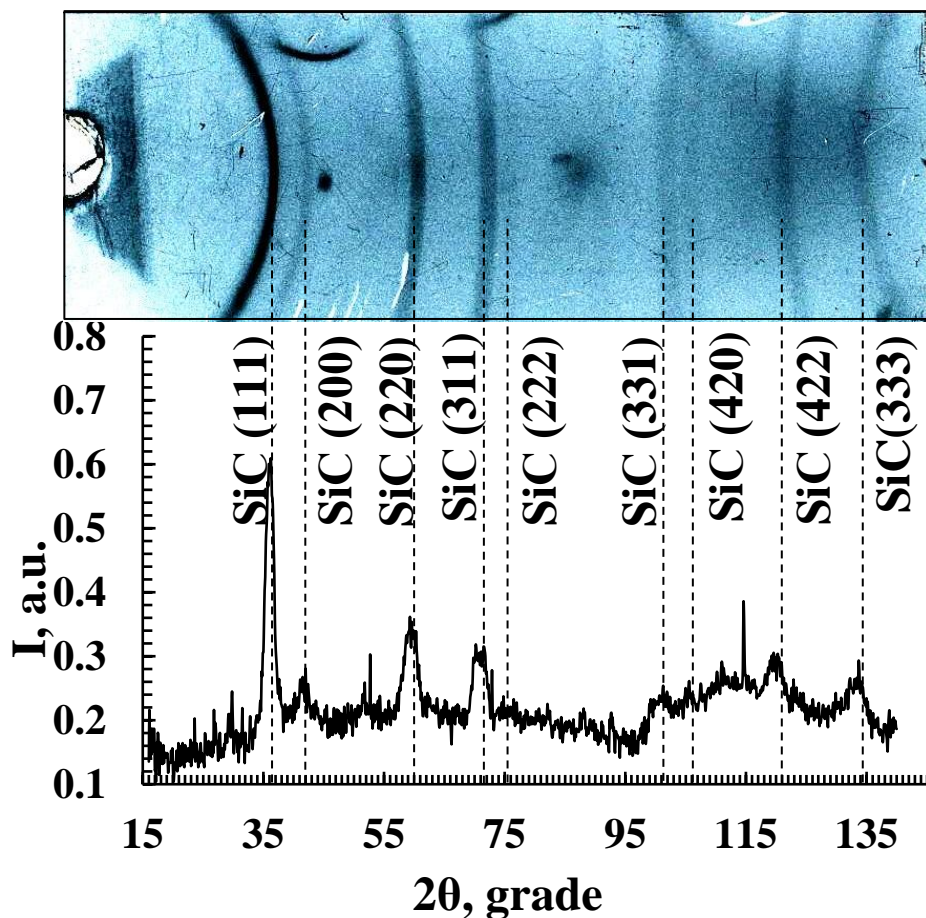
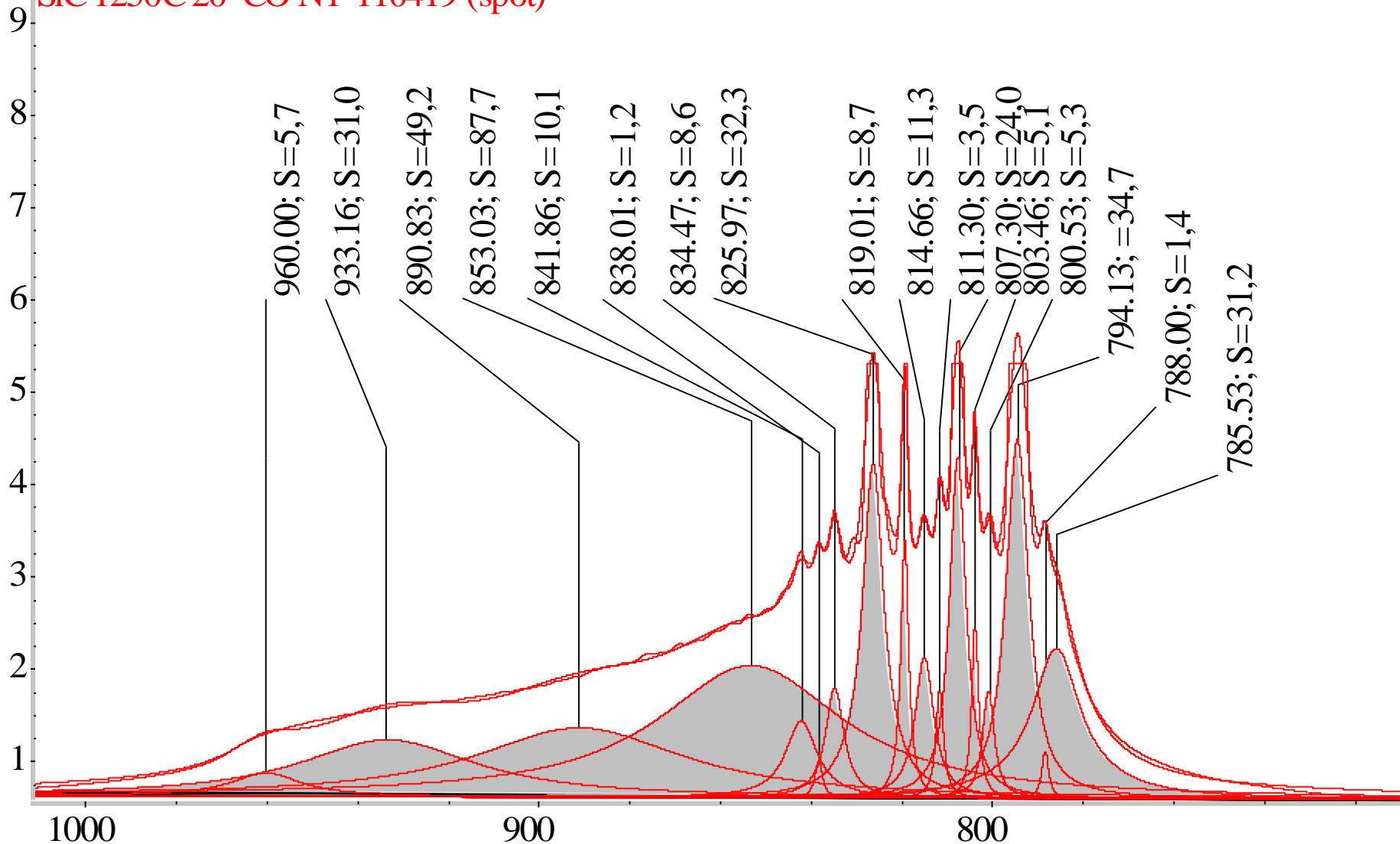


Fig. 3. X-ray diffraction pattern of SiC film synthesized by the method of atom substitution in a silicon lattice at a temperature of  $1250^\circ\text{C}$  for 20 min at a CO gas pressure of 0.8 Pa.

The synthesis of SiC films by the method of atom substitution, recently carried out **in a new facility developed by prof. Nussupov K.Kh.** [26] ( $1250^\circ\text{C}$ , 20 min, CO 0.8 Pa).

Fig. 3 shows that the X-ray patterns of SiC films contain almost all known  $\beta$ -SiC lines. This indicates a high degree of perfection of the structure of SiC nanocrystals formed at a temperature of  $1250^\circ\text{C}$ . The X-ray lines have a uniform intensity, except for the (220) line, which has a reflection of the increased intensity of the single crystal.





The decomposition of IR-spectrum shows a very small content of amorphous SiC (components at 785 and 788  $\text{cm}^{-1}$ ), the presence of  $\beta$ -SiC layer (components at 795  $\text{cm}^{-1}$ ), SiC crystallites of various sizes ( a number of peaks between 800-900  $\text{cm}^{-1}$ ) and dilatation dipoles (component at 957  $\text{cm}^{-1}$ ). The components in the spectrum with maxima at 785.5  $\text{cm}^{-1}$  and 788.0  $\text{cm}^{-1}$  were assigned to Si-C bonds in highly defective deformed nanocrystals.

The IR spectrum contains a number of narrow peaks with wavenumbers  $803.4\text{ cm}^{-1}$ ,  $807.3\text{ cm}^{-1}$ ,  $811.3\text{ cm}^{-1}$ ,  $814.6\text{ cm}^{-1}$ ,  $819.0\text{ cm}^{-1}$ ,  $825.9\text{ cm}^{-1}$ ,  $834.5\text{ cm}^{-1}$ ,  $838.0\text{ cm}^{-1}$ ,  $841.8\text{ cm}^{-1}$ , which could appear due to absorption by small nanocrystals of different sizes.

Indeed, H. Mutschke et.al [12], analyzing the studies on the emission of small SiC particles with a diameter of  $0.3\text{--}3\text{ }\mu\text{m}$  in space objects, note that a broad peak in the  $11.3\text{ }\mu\text{m}$  region ( $\sim 885\text{ cm}^{-1}$ ) was interpreted by various authors as the emission of small SiC particles between the frequencies of transverse ( $\sim 795\text{ cm}^{-1}$ ) and longitudinal ( $\sim 960\text{ cm}^{-1}$ ) optical phonons.

In addition, there are also broad Gaussian peaks with maxima at wave numbers  $853.0\text{ cm}^{-1}$  and  $890.8\text{ cm}^{-1}$  (39%), which can be attributed to Si-C bonds on the surface of nuclei of very small SiC nanocrystals of a wide range of sizes with the domination of nanocrystals absorbing at  $853\text{ cm}^{-1}$  [7, 10, 12].

Silicon carbide nanocrystals and their nuclei can be located both at the “SiC film - Si substrate” interface, and inside the silicon substrate, covering the inner surface of the pores [9, 13]. In general, the crystalline phase of silicon carbide, including the nuclei of small nanocrystals, is estimated to combine carbon and silicon atoms, forming 80.3% of the Si-C bonds of the silicon carbide film.

The peak with a maximum at  $933.1\text{ cm}^{-1}$  (8.8%) can be attributed to shortened Si – C bonds in silicon carbide clusters. The peak with a maximum in the region of  $960\text{ cm}^{-1}$  (1.6%), observed earlier in [9, 13, 17], corresponds to a special mechanical connection between the vibration energy of an elastic dilatation dipole ( $C - V_{\text{Si}}$ ).

It was found that an increase in the synthesis temperature by the method of atomic substitution from 1250°C to 1350°C leads to an increase in IR absorption and an expansion of the interval of the appearance of narrow peaks of various intensities up to 730 - 960 cm<sup>-1</sup>, and this is due to an increase in the amount of optically active Si-C-bonds, an increase in the total volume of silicon carbide, as well as the formation of structural elements in the form of spatially limited amorphous structures (730–790 cm<sup>-1</sup>), nano- and microcrystallites of silicon carbide of various sizes and polytypes (795–902 cm<sup>-1</sup>).

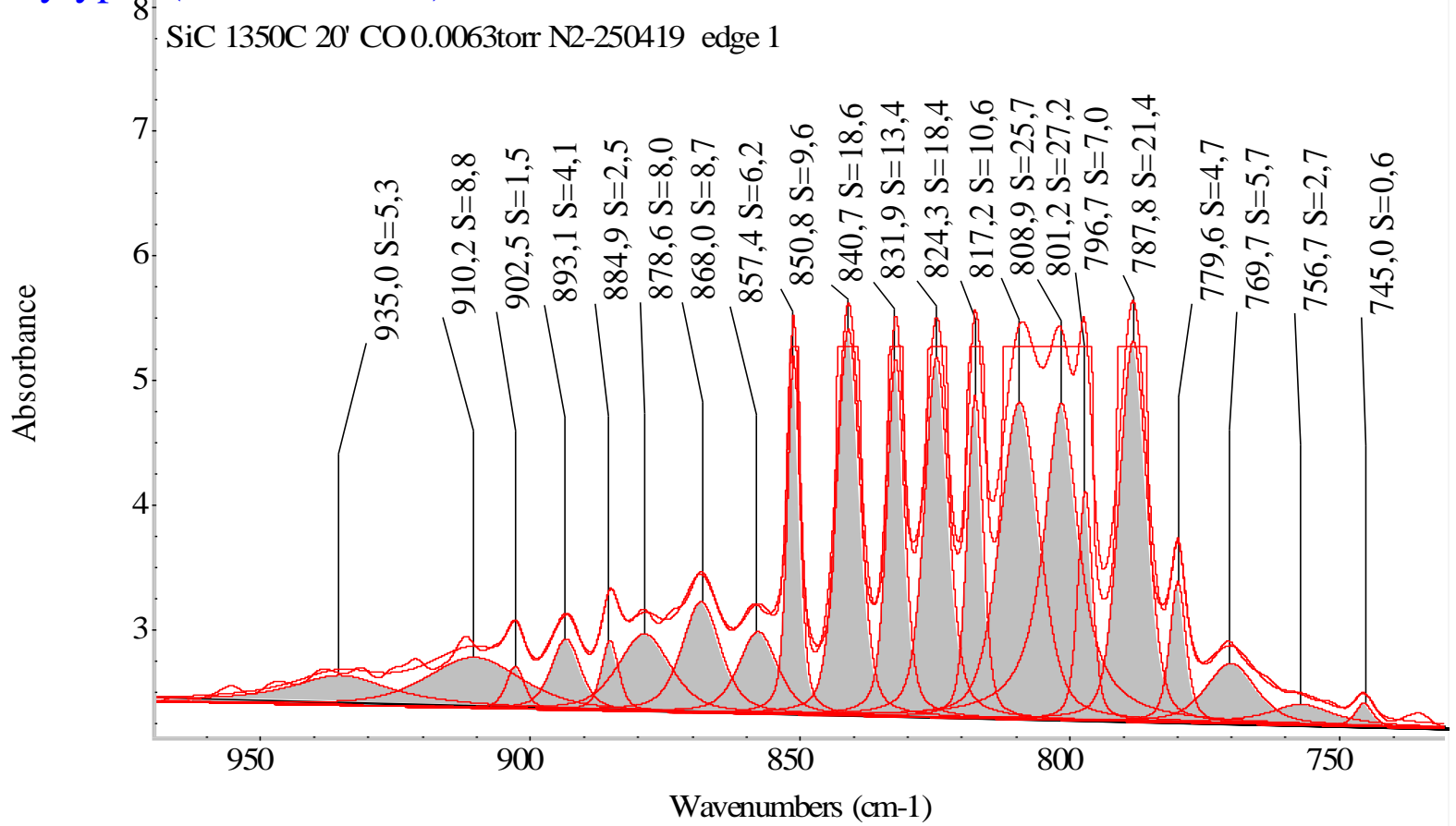


Figure 5 - Decomposition of the IR absorption spectrum of a SiC film synthesized in CO gas at a temperature of 1350°C and a pressure of 0.8 Pa for 20 min by the method of atomic substitution



It was found that the difference between the synthesis of SiC films by the method of atomic substitution at a temperature of 1350°C in a CO gas atmosphere (0.8 Pa, 20 min) is the formation of SiC nanocrystals of various polytypes, including  $\beta$ -SiC, 6H-SiC, 15R-SiC, as well as phases of tridymite  $\text{SiO}_2$ . Another structural feature of the films is the presence of  $\beta$ -SiC, 6H-SiC,  $\text{SiO}_2$  microcrystallites, and  $\beta$ -SiC and 6H-SiC single crystal layers.

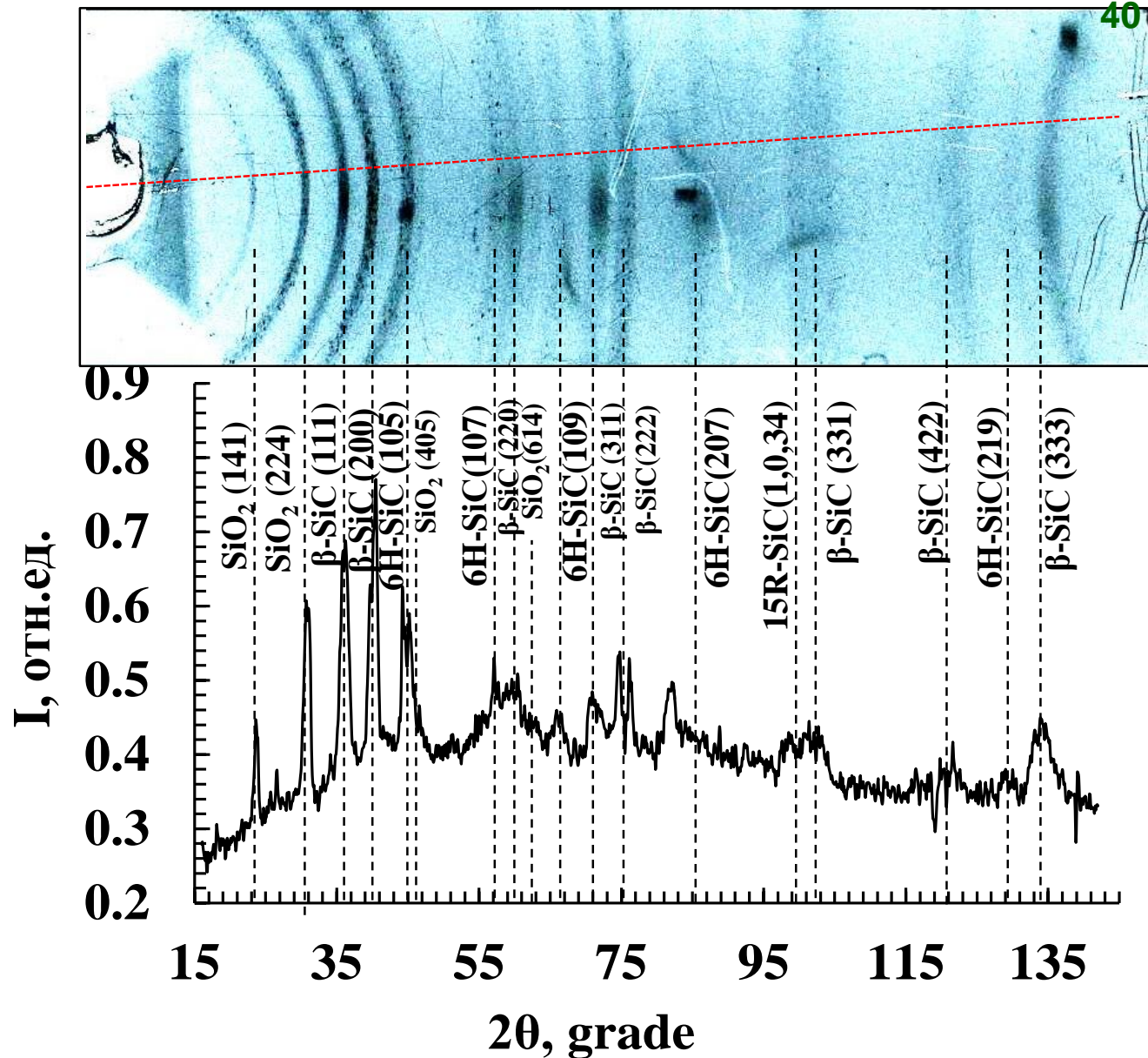


Fig.12 - Debyeogram and intensity of X-ray reflections  $I(2\theta)$  of a thin silicon carbide film synthesized at a temperature of 1350°C and a pressure of 0.8 Pa for 20 minutes by the atomic substitution method



## **Silicon Carbide Synthesized by rf Magnetron Sputtering in the Composition of a Double Layer Antireflection Coating SiC/MgF<sub>2</sub>**

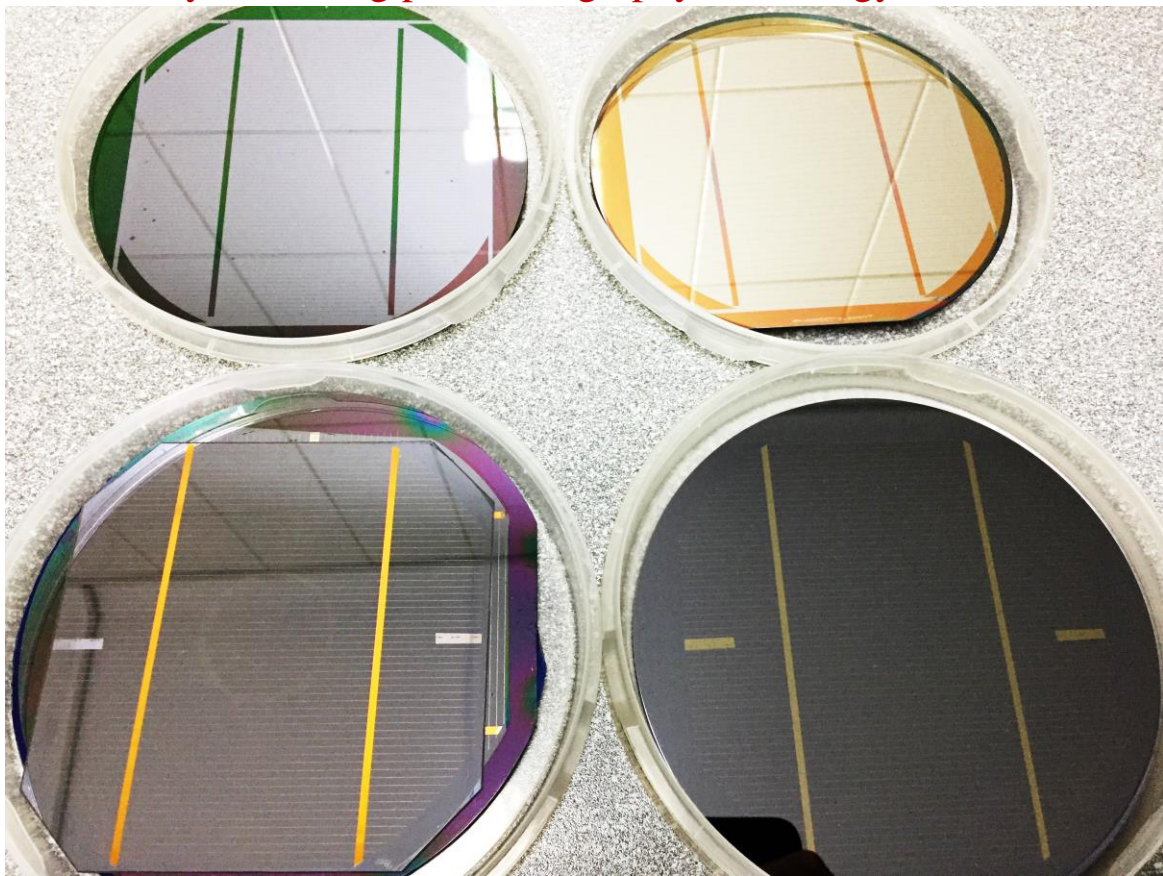
K.Kh. Nussupov, N.B. Beisenkhanov\*, S. Keiinbay, A.T. Sultanov

In Kazakh-British Technical University (Almaty, Kazakhstan) the technology of solar cells is developed using the methods of magnetron sputtering, electron beam evaporation and photolithography process.





Stages of the technological route for the creation of a solar cell contact system using photolithography technology



Solar Tree with a power of 0.5 kW



Fisherman's equipment

Mini power plant on the roof of KBTU

SEZ PIT ALATAU

Solar energy has the highest potential for development.

The top priorities - the increase the efficiency and reduce the cost of solar cells.

The most effective way: optimization of antireflection and passivation coatings.

The most effective are double layer coatings  $\text{ZnS/MgF}_2$  and  $\text{TiO}_2/\text{SiO}_2$ . These gradient structures show excellent results in reducing reflection.

Disadvantages of antireflection coatings:  $\text{ZnS/MgF}_2$  deposition requires heating silicon substrates for proper film adhesion.

Universal coatings can perform both passivating and antireflection functions.

Silicon carbide can be used as a passivation layer for silicon solar cells.

Silicon carbide films can reduce the reflection up to 3%.

SiC films formed by the CVD method using poisonous gas monosilane and high temperatures of the substrate, negatively affects the lifetime of minority carriers.

In this work, an antireflection double layer  $\text{SiC/MgF}_2$  are synthesized by RF magnetron sputtering.



## Material and methods

MAGNA TM-200-1 device - RF 13.56 MHz magnetron sputtering, Ar 0.4 Pa, SiC target.  
Substrates: c-Si (p-type, (100) orientation,  $\sim 400 \mu\text{m}$  of thickness) and sapphire.

The first group of SiC films: the power of 100, 150, 200, 250 W, for 1800 seconds.

X-ray reflectometry in the  $\theta$ - $2\theta$  mode: to determine the thickness of the SiC films.

GenX software: theoretical curve was fitted to the measured curves to determine density, thickness and roughness. Then, the deposition rate of the films was calculated.

SCOUT software: refractive index and extinction coefficient were calculated by fitting theoretical and experimental reflection and transmission curves of films on the sapphire.

Lumerical FDTD and SCOUT software: by simulation the most effective combination of antireflection coating SiC/MgF<sub>2</sub> was calculated.



Upgraded the  
TM-200-01  
MAGNA  
installation for  
deposition of  
nanostructures  
by magnetron  
sputtering



Modern X-ray  
reflectometer  
Complexray C6  
to determine the  
thickness,  
density and  
roughness of  
the films

The second group of SiC films - 50 nm thickness.

The powers - 100, 150, 200, 250 W, but the time varied to achieve of 50 nm thickness.

Nicolet iS50 (400-4000  $\text{cm}^{-1}$ ) - for IR spectroscopy studies of SiC films.

Evolution 300 UV-VIS spectrophotometer (300-1100 nm) – to measure the transmission and reflection spectra.

ELU TM-5 – for deposition of  $\text{MgF}_2$  films on SiC surface by e-beam evaporation of pure  $\text{MgF}_2$  grains simultaneously on SiC films and c-Si substrate.

Voltage between the electron gun and the crucible - 6 kV,

the current through the filament - 6 mA, the deposition time - 280 seconds,

the substrate rotation - 5 rad/s; the deposition rate increased from 0.25 to 0.8 nm/s.



Infrared FTIR spectrometer  
Nicolet iS50 FT-IR with  
Raman prefix

Spectrophotometer Evolution-  
300 to measure transparency,  
reflection and absorption



Electron-beam unit "ELU TM-5"  
for deposition of antireflective  
coatings on silicon solar cells



Anti-reflective coating is required to reduce optical loss caused by the reflection of light from the surface of solar cells. Since silicon has a high refractive index  $n = 3.9$ , about 35% of the incident light is reflected from its surface. The reflection reduction strategy is based on an idea proposed by Lord Rayleigh in 1879 [27]. The essence of this method is the use of gradient structures with a decreasing refractive index from the substrate ( $n_{sub}$ ) to the medium ( $n_{air}$ ).

The choice of materials for antireflection coatings is based on the principles of quarter-wave films and the determination of the optimal values of the refractive index  $n$  of the gradient structure. In quarter-wave antireflection coatings of thickness  $d$ , satisfying the condition  $nd = \lambda/4$ , the intensity of the reflected rays is canceled out at normal incidence.

Using the expression  $n^2 = n_{air} \cdot n_{sub}$  for a single layer coating, as well as the expressions  $n_2^2 = n_1 \cdot n_{sub}$  and  $n_1^2 = n_{air} \cdot n_2$  for a double layer system substrate/layer2/layer1/air, it is easy to obtain the optimal refractive indices:

$n_1 = \sqrt[3]{n_{air}^2 \times n_{sub}}$  and  $n_2 = \sqrt[3]{n_{air} \times n_{sub}^2}$ . If  $n_{air} \approx 1$  and  $n_{sub} \approx 3.9$ , then the upper layer should have a refractive index  $n_1 \approx 1.57$ , which, in the range of 300-1100 nm, approximately corresponds to  $MgF_2$  ( $n = 1.42-1.44$ ) [30]. The lower layer should have a refractive index  $n_2 \approx 2.47$ , which is comparable to the refractive indices of SiC ( $n = 2.60- 2.73$ ) [30].

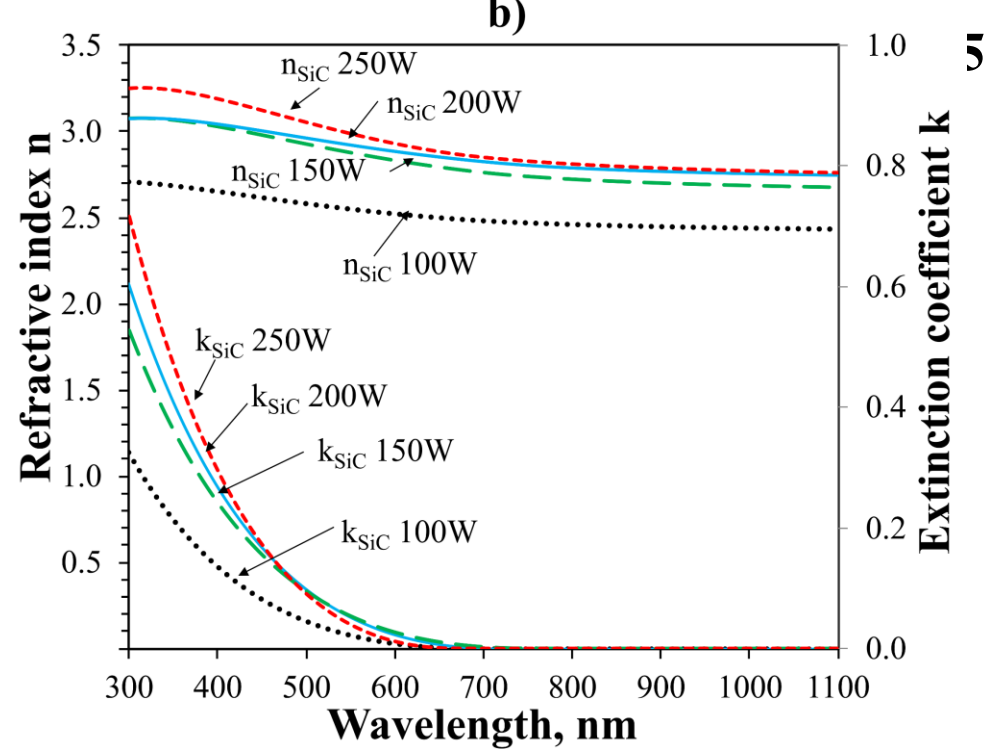
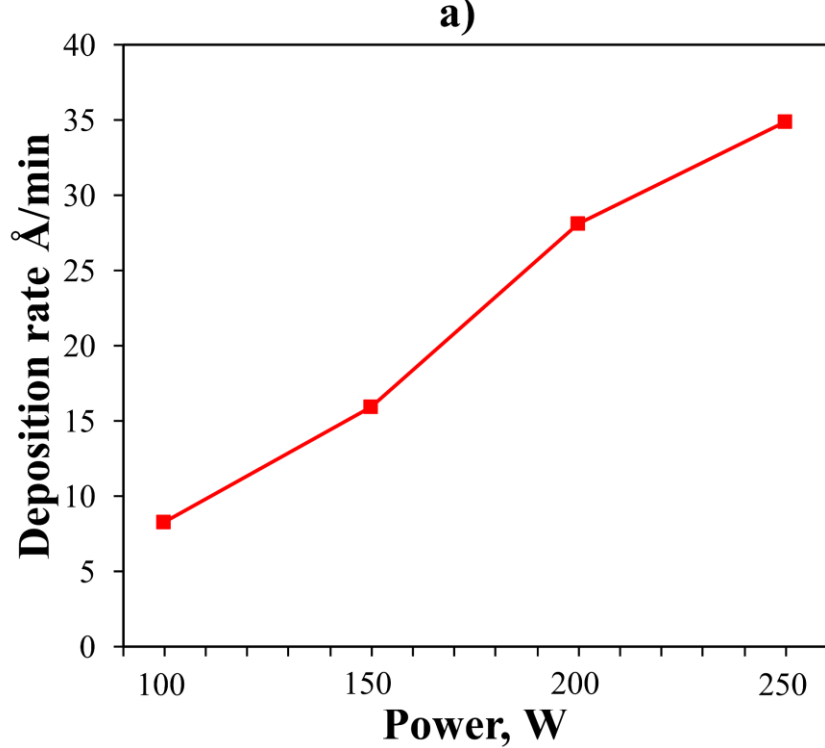


Figure 1 – Dependence of characteristics on the power of the magnetron: a) Deposition rate of SiC films; b) Refractive index and extinction coefficient of SiC films over a wavelength.

With an increase in the magnetron power, the deposition rate grows almost linearly, from 6.7 to 27.8 Å/min in the power range of 100 - 250 W.

In order to calculate the optical constants of SiC films, we used the transmission and reflection spectra of films on a sapphire substrate. The values of the refractive index and extinction coefficient of SiC films in the wavelength range of 300-1100 nm were calculated using the SCOUT software by curve fitting (Fig. 1 (b)). A decrease in the magnetron power and an increase in the wavelength leads to a decrease in the refractive index from 3.25 to 2.43 and the extinction coefficient from 0.7 to 0.

The SiC films deposited at a magnetron power of 250 W have the highest refractive index and extinction coefficient. The refractive index of these films is gradually decreased from 3.25 to 2.80 in the wavelength range 300 - 800 nm, while the extinction index sharply decreases from 0.7 to 0 in the range 300 - 600 nm.

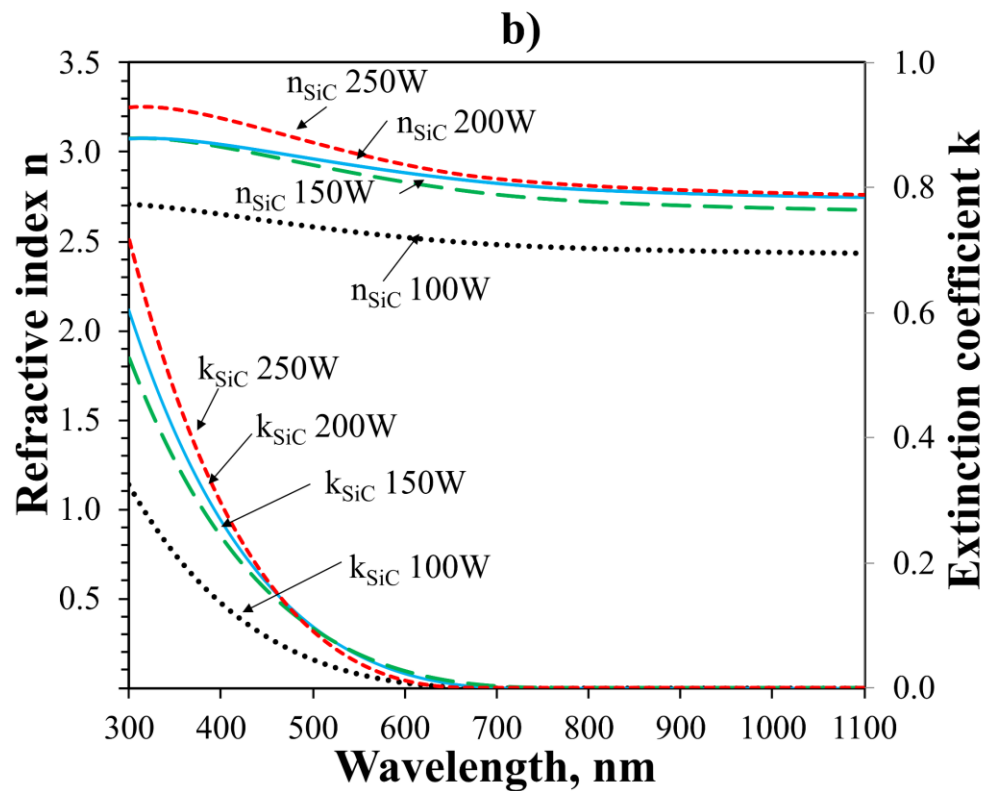


Figure 1 – Dependence of characteristics on the power of the magnetron: a) Deposition rate of SiC films; b) Refractive index and extinction coefficient of SiC films over a wavelength.

Films deposited at a power of 100 W have much lower optical constants. The refractive index of such films gradually decreases from 2.71 to 2.47 in the range 300 - 800 nm. The extinction coefficient has a similar tendency to decrease in the same range of 300 - 600 nm, but still has lower values - less than 0.3. This suggests that silicon carbide films deposited at a magnetron power of 100 W are more transparent in the range 300 - 600 nm.

# Antireflection coatings simulation

To simulate the structure and obtain results as close to reality as possible, we used the optical constants of films directly deposited on our own MAGNA TM-200-1 installation at certain parameters. The simulations were primarily done using the Lumerical FDTD software. Antireflection coating consisting of the SiC and MgF<sub>2</sub> layers was deposited on polished silicon 2 microns thick. The low thickness of substrate does not affect the final reflection result, but significantly reduces the calculation time.

The thickness of the SiC films varied from 40 to 70 nm with a step of 10 nm, while for MgF<sub>2</sub> it remained unchanged - 130 nm. A "plane wave" with wavelengths in the range of 300-1100 nm was used as a light source. The simulation was performed in 3D mode. Despite the high reflection in the 350-550 nm wavelength range, all silicon carbide films are characterized by a decrease in reflection to values below 10% in the 550–1100 nm wavelength range and below 5% at least in the 680 - 940 nm range. For a 100 W/50 nm curve, the reflection is below 5% in the widest wavelength range 425–1100 nm.

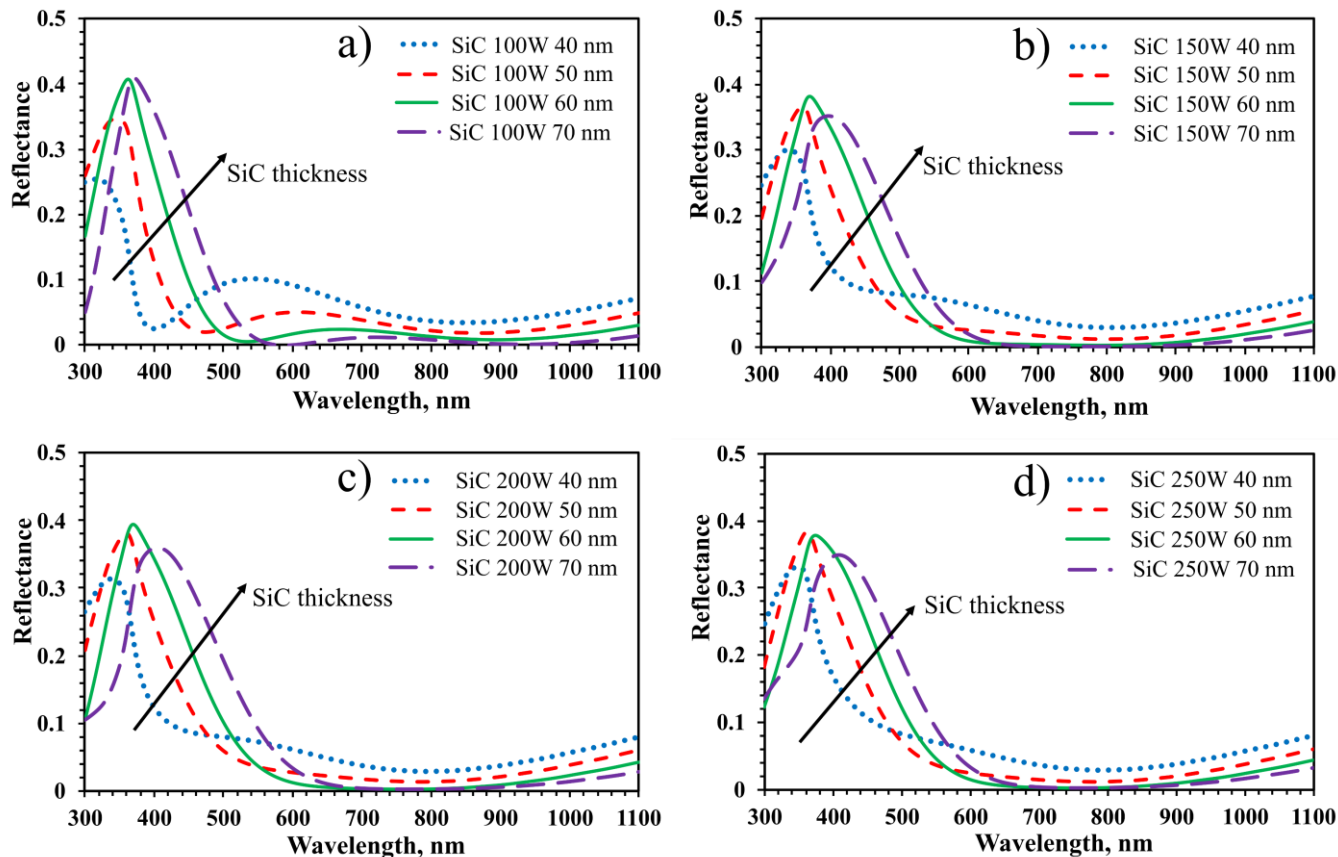


Figure 2 – Calculated Lumerical FDTD reflection for SiC films 40–70 nm thick in a Si/SiC/MgF<sub>2</sub> system deposited at a magnetron power: a) 100 W; b) 150 W; c) 200 W; d) 250 W



## Antireflection coatings simulation

To confirm obtained results, an identical structure was modeled using the SCOUT and OPAL software. For SCOUT it was taken into account that the Evolution 300 UV-VIS spectrophotometer measures at incidence angle of  $12.5^\circ$ . In this regard, the results are slightly different. However, for a 50 nm thick silicon carbide layer, the reflection curves simulated in SCOUT are generally comparable to the Lumerical FDTD results (Fig. 3 (a)). Films deposited at a magnetron power of 100 W also have the lowest reflection in the wavelength range 300–520 nm and 780–1100 nm. OPAL software was used to determine photon current. This allowed us to show the amount of reflected light, absorbed light in the substrate and in the antireflection layer. The simulation was performed for the same structures. The thickness of the silicon carbide layer varied within 40–70 nm, while the  $\text{MgF}_2$  thickness remained unchanged at 130 nm, surface morphology was planar. The magnitude of the incident light was  $44 \text{ mA/cm}^2$ .

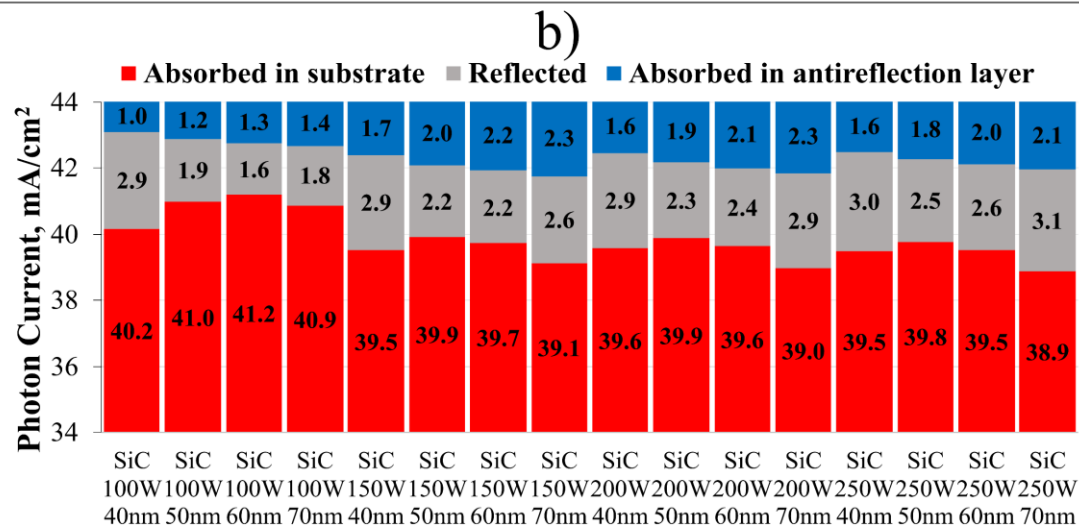
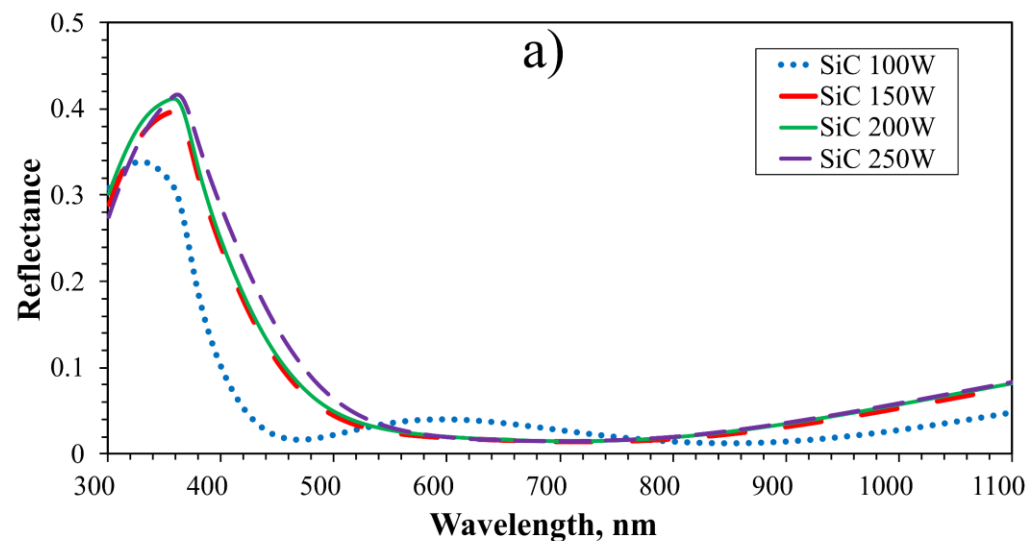


Figure 3 – a) Calculated reflection according to SCOUT software for SiC layers 50 nm thick in the Si/SiC/ $\text{MgF}_2$  system, deposited at a magnetron power of 100, 150, 200, 250 W; b) The amount of reflected photon current ( $\text{mA/cm}^2$ ), absorbed photon current in the substrate and in the antireflection layer calculated by OPAL

## Antireflection coatings simulation

An evaluation of the data obtained from the OPAL software (Fig. 3 (b)) shows that at a low magnetron power of 100 W, the photocurrent absorption in the substrate increases. Due to the increased extinction coefficient for films deposited at higher power the amount of photocurrent absorbed in the antireflection layer increases. Moreover, a thickness of 50 nm is optimal for photoelectric enhancement at a magnetron power in the range of 150–250 W. For a magnetron power of 100 W, a film 60 nm thick has the best properties.

Theoretically best antireflection effect is achieved by films with a thickness of 50-60 nm deposited at 100 W. This may be due to the presence of a more suitable refractive index of these films, which is closer to the theoretically optimal value  $n = 2.47$  (Fig. 1 (b)).

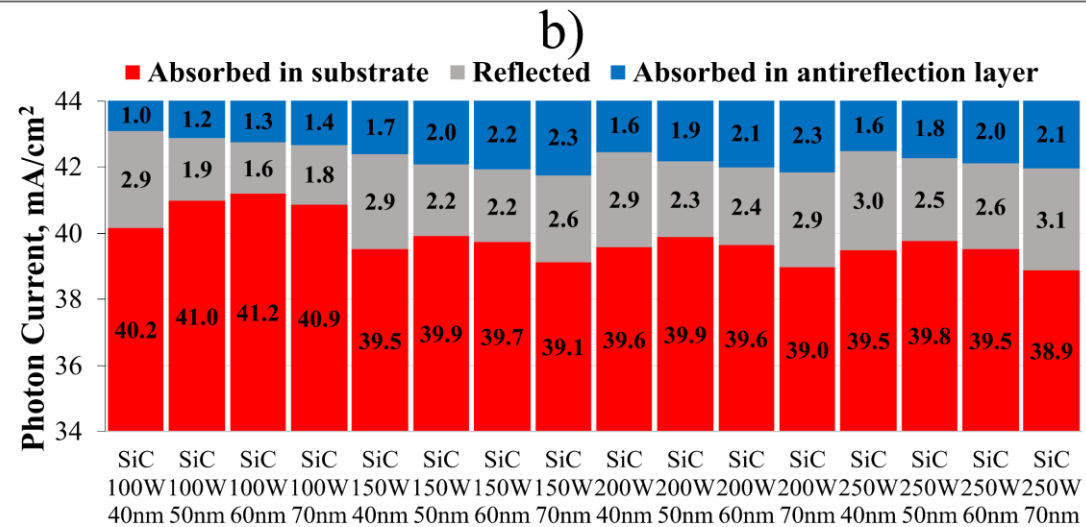
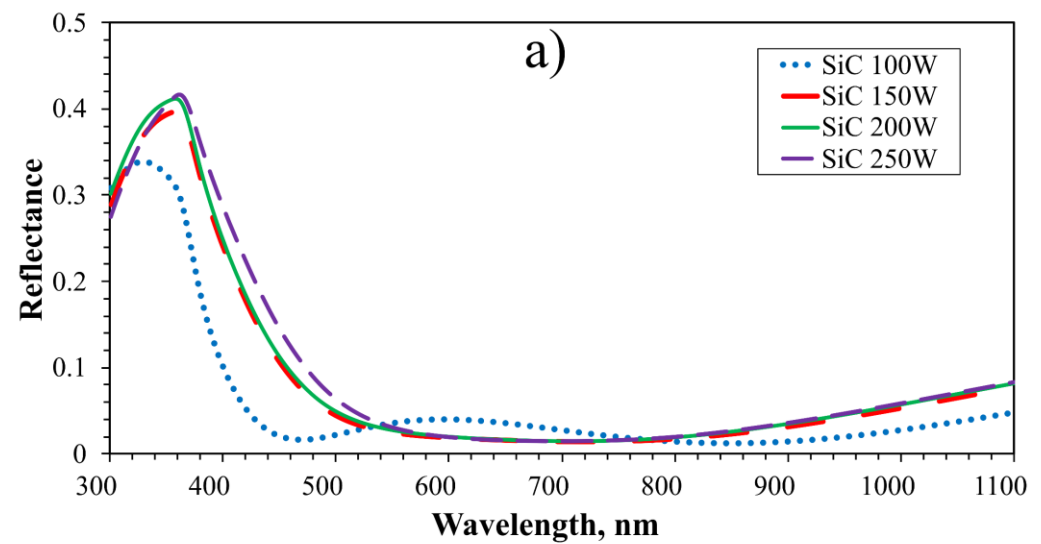


Figure 3 – a) Calculated reflection according to SCOUT software for SiC layers 50 nm thick in the Si/SiC/MgF<sub>2</sub> system, deposited at a magnetron power of 100, 150, 200, 250 W; b) The amount of reflected photon current (mA/cm<sup>2</sup>), absorbed photon current in the substrate and in the antireflection layer calculated by OPAL

Pairs of experimental and theoretical curves obtained from SiC films deposited at powers of 100-250 W are shown in Fig. 4. It was possible to achieve a high agreement between the experimental (broad black line) and theoretical (the narrow blue line) curves.

Fig. 4 (a) shows the results of SiC films deposited at a magnetron power of 100 W. Visual analysis shows a decrease in the amplitude of the curve oscillations at angles of  $2\theta \sim 0.8^\circ$ - $1.6^\circ$ , which is caused by the presence of a less dense oxide  $\text{SiO}_2$  film 0.9 nm thick and density  $\rho_{\text{SiO}_2} = 2.17 \text{ g/cm}^3$  between the silicon substrate and the silicon carbide film. In this case, the density of the SiC film  $\rho = 2.92 \text{ g/cm}^3$ , turned out to be lower than the reference value  $\rho_{\text{SiC}} = 3.21 \text{ g/cm}^3$ . A decrease in the density of the film can be due to the presence of nanopores or a violation of stoichiometry caused by a decrease in the

concentration of carbon in the chamber due to the formation and removal of  $\text{CO}_2$  molecules, and appearance of  $\text{SiO}_2$  molecules inside SiC layer. The thickness of the SiC film was found to be 54.3 nm, and its roughness was  $\sigma = 0.8 \text{ nm}$ . Thus, it was possible to obtain a silicon carbide film with a thickness close to the desired one, deposited at a magnetron power of 100 W.

An increase in the magnetron power to 150 W led to form SiC layer (Fig. 4 (b)):  $\rho = 3.05 \text{ g/cm}^3$ ,  $d = 54.9 \text{ nm}$ ,  $\sigma = 0.84 \text{ nm}$ .  $\text{SiO}_2$  layer:  $\rho = 2.18 \text{ g/cm}^3$ ,  $d = 0.6 \text{ nm}$ .

For the SiC film grown at 200 W (Fig. 4 (c)):  $\rho = 3.1 \text{ g/cm}^3$ ,  $\sigma = 1.4 \text{ nm}$ ,  $d = 51.5 \text{ nm}$ .  $\text{SiO}_2$  layer:  $\rho = 2.13 \text{ g/cm}^3$ ,  $d = 0.9 \text{ nm}$ .

For the SiC film grown at 250 W (Fig. 4 (d)):  $\rho = 3.05 \text{ g/cm}^3$ ,  $d = 51.6 \text{ nm}$ ,  $\sigma = 1.03 \text{ nm}$ .  $\text{SiO}_2$  layer:  $\rho = 2.18 \text{ g/cm}^3$ ,  $d = 0.2 \text{ nm}$  due to increasing the duration of ionic cleaning from 2 to 3 minutes.

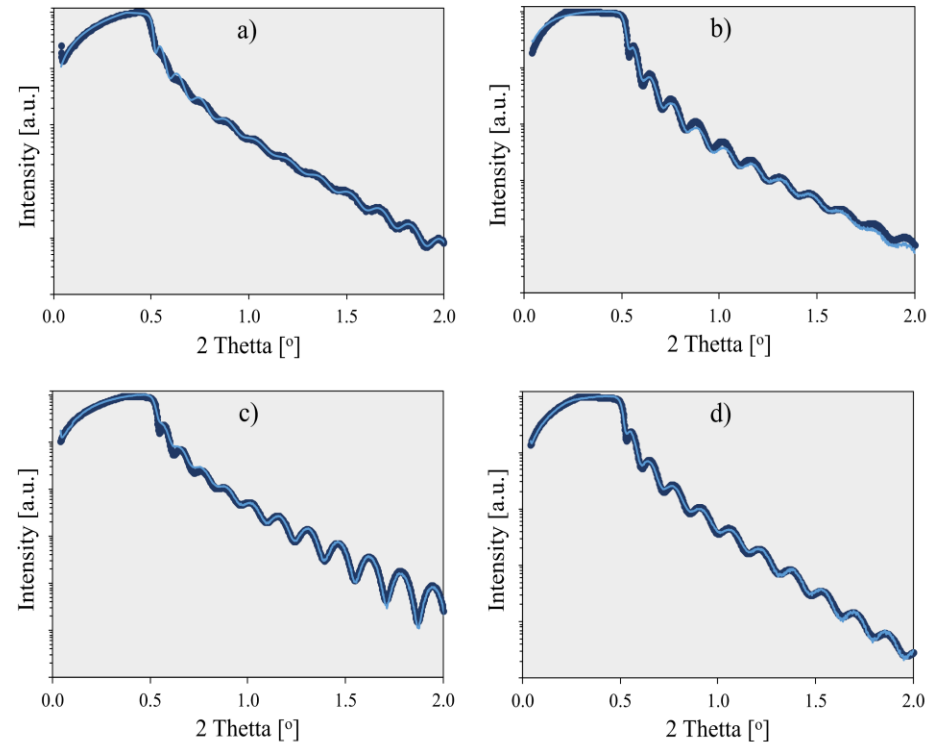


**Figure 4 – X-ray reflectometry of SiC films deposited by RF magnetron sputtering on silicon under different magnetron power: a) 100 W – 4500 s; b) 150 W – 2520 s; c) 200 W – 1500 s; d) 250 W – 1080 s**

From the equation  $x = x_1 + (\rho_x - \rho_1) \cdot (x_2 - x_1) / (\rho_2 - \rho_1)$ , where  $\rho_1 = 2.33 \text{ g/cm}^3$ ,  $\rho_2 = 3.21 \text{ g/cm}^3$ ,  $\rho_1 < \rho_x < \rho_2$ ,  $x_1 = 0$ ,  $x_2 = 1$ ,  $x_1 < x < x_2$ , and  $\rho_x = 2.92 \text{ g/cm}^3$ ,  $3.05 \text{ g/cm}^3$ ,  $3.10 \text{ g/cm}^3$ ,  $3.05 \text{ g/cm}^3$  of the studied layers obtained at a magnetron power of 100, 150, 200, 250 W, respectively, the composition of films was determined: SiC/100W=SiC<sub>0.67</sub>; SiC/150W=SiC<sub>0.82</sub>; SiC/200W=SiC<sub>0.88</sub>; SiC/250W=SiC<sub>0.82</sub>.

It follows that, in the absence of pores, the SiC/100W film should have the maximum deviation from stoichiometry and an excess of silicon, i.e. the maximum refractive index, since  $n_{\text{Si}} > n_{\text{C}}$  (see paragraph 4.1). However, calculations show (Fig. 1) that the refractive index in the case of SiC/100W has the lowest values in the entire wavelength range of 300–1100 nm. For other films, the refractive index increases with increasing magnetron power.

We can conclude that the values of the film density and refractive index are influenced to a greater extent not by the stoichiometry of the film composition, but by its porosity. Since the pore refractive index is close to 1, this can cause a decrease in the refractive index value with increasing the pore concentration and volume. When sputtering a silicon carbide target, along with silicon and carbon atoms, nanoparticles can come off. With a decrease in the power of the magnetron, the concentration of nanoparticles in the film can increase, between which there may be pores. In this case, reducing the power to 100 W will cause a noticeable decrease in the refractive index. Nevertheless, an increase in extinction with an increase in the power of the magnetron indicates a slight increase in the silicon concentration and its negative effect on the optical properties of the film.

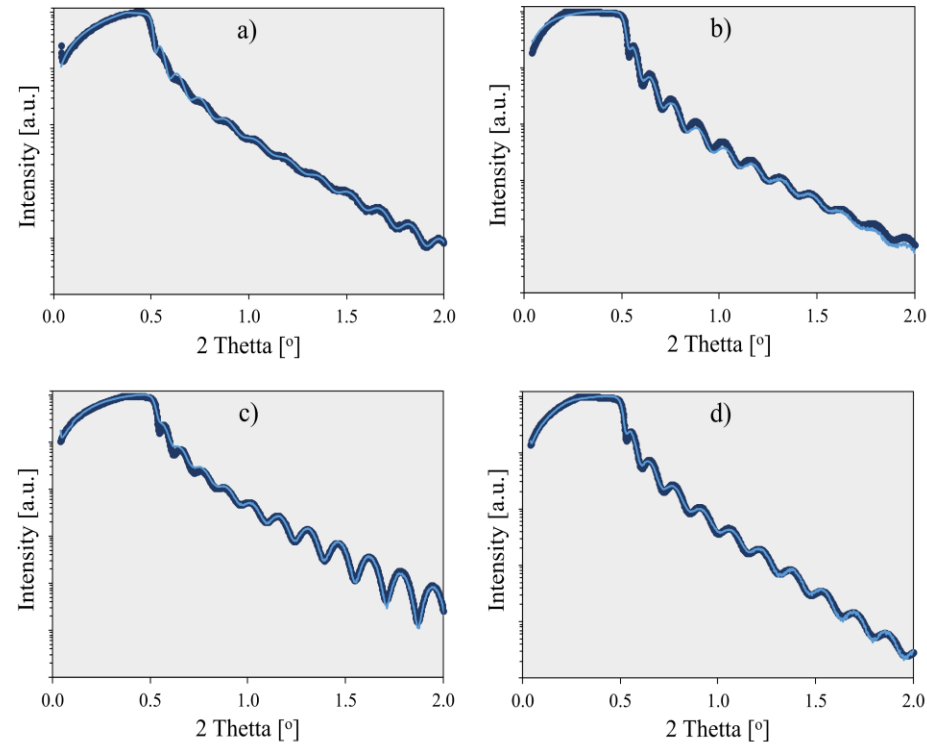


**Figure 4 – X-ray reflectometry of SiC films deposited by RF magnetron sputtering on silicon under different magnetron power: a) 100 W – 4500 s; b) 150 W – 2520 s; c) 200 W – 1500 s; d) 250 W – 1080 s**



## IR Spectroscopy

To establish a more reliable picture of the layer structure, an IR study of the films was carried out. The FWHM was  $262\text{ cm}^{-1}$  (100 W),  $238\text{ cm}^{-1}$  (150 W),  $262\text{ cm}^{-1}$  (200 W),  $253\text{ cm}^{-1}$  (250 W), and this corresponds to the parameters of amorphous silicon carbide ( $200\text{--}300\text{ cm}^{-1}$ ).

The IR spectrum (Fig. 5 (a)) obtained from the SiC/100W film shows the presence of broad absorption bands with maxima at  $808\text{ cm}^{-1}$  and  $1015\text{ cm}^{-1}$ . The maximum at  $808\text{ cm}^{-1}$  may be due to the prevalence of shortened Si–C bonds characteristic of small particles, for example, nanoclusters and nanocrystal nuclei.

An increase in the magnetron power, the maximum shifts from  $808\text{ cm}^{-1}$  (100 W) to  $797\text{ cm}^{-1}$  (150 W),  $794\text{ cm}^{-1}$  (200 W), and  $785\text{ cm}^{-1}$  (250 W). The shift of the maximum of the SiC peak to the region below  $795\text{ cm}^{-1}$  indicates a lower ordering of the structure corresponding to the vibrations of Si–C bonds of the stretching modes in amorphous silicon carbide. This may be due to the more intense sputtering of the target.

In the region between  $795$  and  $800\text{ cm}^{-1}$ , there are usually peaks characteristic of Si–C bonds of tetrahedral orientation.

The bands associated with longitudinal stretching vibrations of the Si–O bond, which are caused by the motions of bridging oxygen atoms in the  $\text{SiOSi}_3$  ( $1145\text{ cm}^{-1}$ ) and  $\text{SiO}_2\text{Si}_2$  ( $1205\text{ cm}^{-1}$ ) complexes, can contribute to the amplitude of the spectrum.

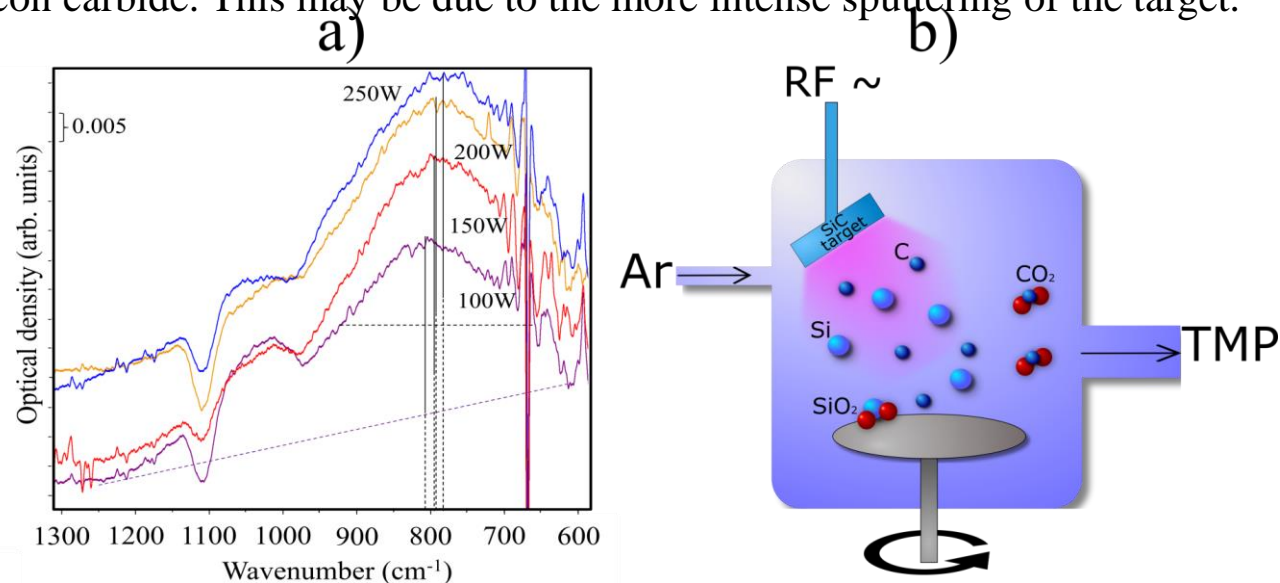


Figure 5 – a) IR absorption spectra of SiC films deposited by RF magnetron sputtering prepared under magnetron powers 100W, 150W, 200W, 250W. b) The process of sputtering SiC target and the interaction of Si and C atoms with residual oxygen, which leads to the formation of massive  $\text{SiO}_2$  and lightweight  $\text{CO}_2$  molecules

## IR Spectroscopy

The hypothesis about the possibility of detachment of small silicon carbide nanoparticles at a lower sputtering power of 100 W requires verification. In this case, one should expect a larger number of tetrahedrally oriented Si-C bonds, absorbing in the region of  $795\text{--}800\text{ cm}^{-1}$ . The small size of nanoparticles increases in the contribution to the spectrum of their surface containing shortened Si-C bonds, which leads to a shift in the maximum of IR absorption from  $795$  to  $808\text{ cm}^{-1}$ . The deposition of nanoparticles instead of individual atoms implies a less dense packing and the presence of a large number of nanopores and voids in the film, leading to a significant decrease in the density of the film. Indeed, in Fig. 5 (a), it can be seen (see solid vertical lines) that the amplitude of the absorption intensity of the SiC peak reduces with decreasing power from 0.038 (250 W) to 0.037 (200 W), 0.037 (150 W), and 0.030 (100 W). A significant decrease in the amplitude (A) and area ( $\sim A \times \text{FWHM}$ ) of the SiC peak of film deposited at 100 W indicates a significant decrease in the total number of Si-C bonds.

Thus, a decrease in the density ( $2.92\text{ g/cm}^3$ ) and the total number of Si-C bonds while maintaining the film thickness clearly indicates the presence of nanopores formed between SiC nanoparticles.

The decrease in refractive index of SiC films at a magnetron power of 100 W is explained by a decrease in the concentration of silicon atoms to a composition close to stoichiometric SiC and the presence of nanopores and voids (with  $n \sim 1$ ) due to the detachment of nanoparticles from the SiC target and their deposition on the silicon surface.

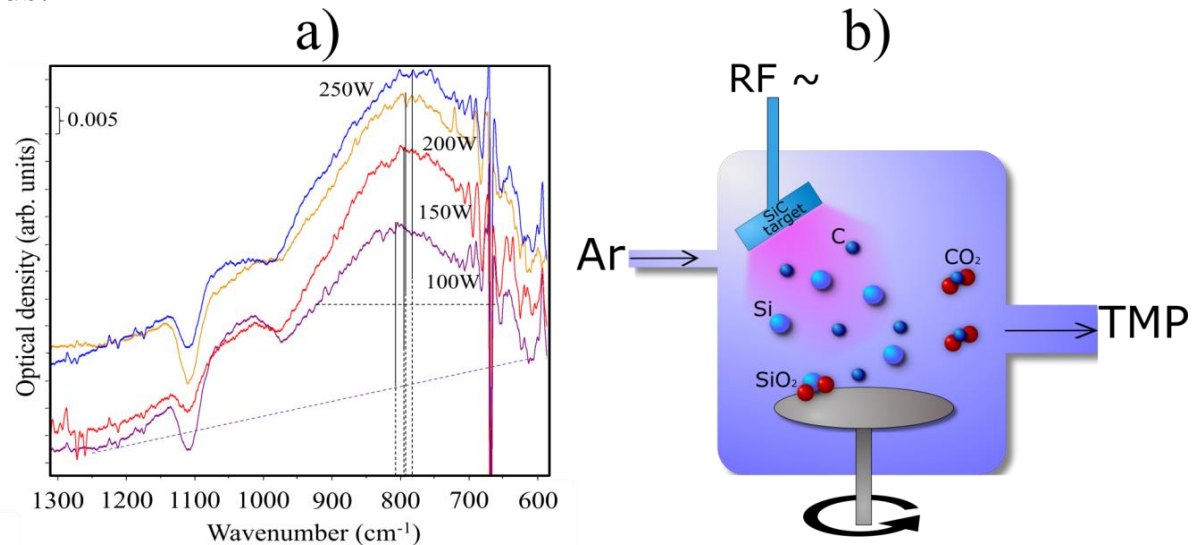


Figure 5 – a) IR absorption spectra of SiC films deposited by RF magnetron sputtering prepared under magnetron powers 100W, 150W, 200W, 250W. b) The process of sputtering SiC target and the interaction of Si and C atoms with residual oxygen, which leads to the formation of massive SiO<sub>2</sub> and lightweight CO<sub>2</sub> molecules

## Reflection

After the deposition of amorphous silicon carbide film on the silicon surface, the second layer of the antireflection coating ( $\text{MgF}_2$  of 130 nm thick) was synthesized. To determine the efficiency of double layer antireflection coating  $\text{SiC}/\text{MgF}_2$  the reflection spectrum was measured. Simultaneously, the experimentally obtained reflection values were compared with the simulated values provided by the Lumerical FDTD and SCOUT software. In addition, the experimentally obtained reflection spectrum from polished silicon was shown. To approximate the real and simulated conditions as much as possible, the thickness of the films for each deposition mode, as well as the presence of an oxide film, were taken into account (Fig. 6)..

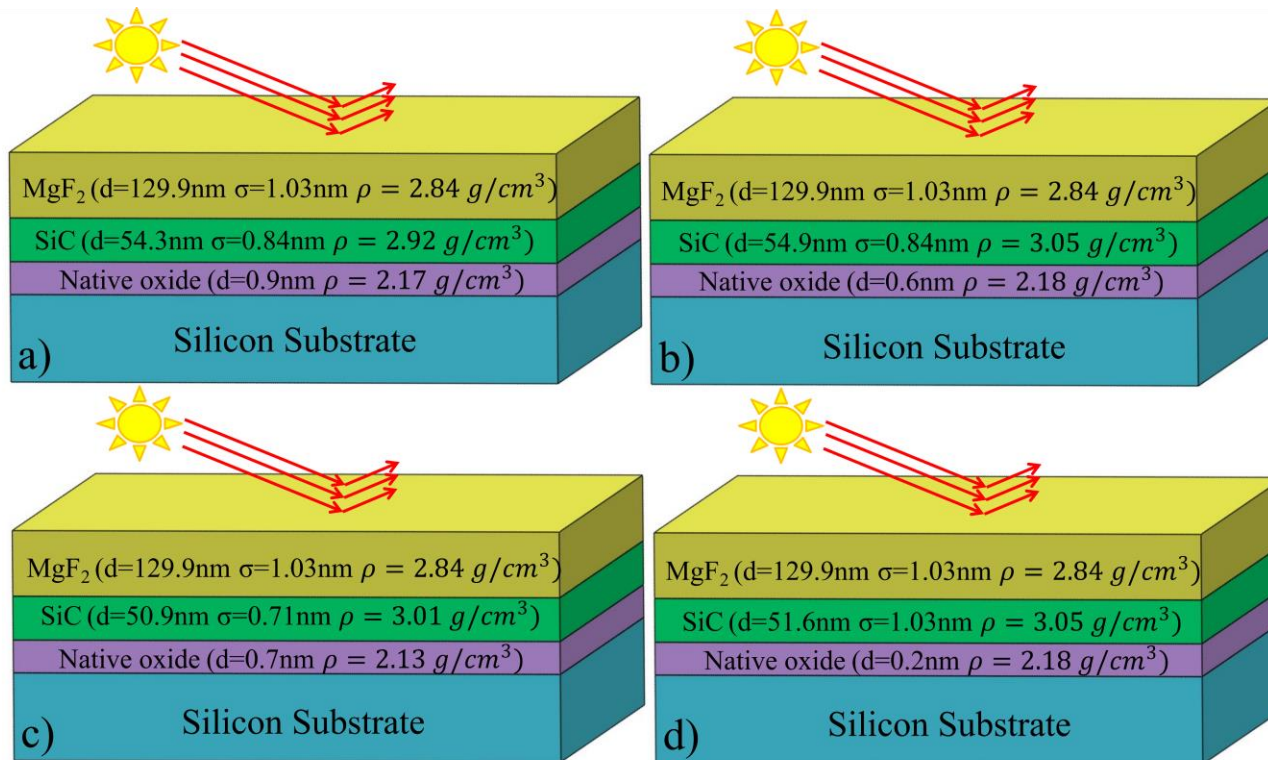
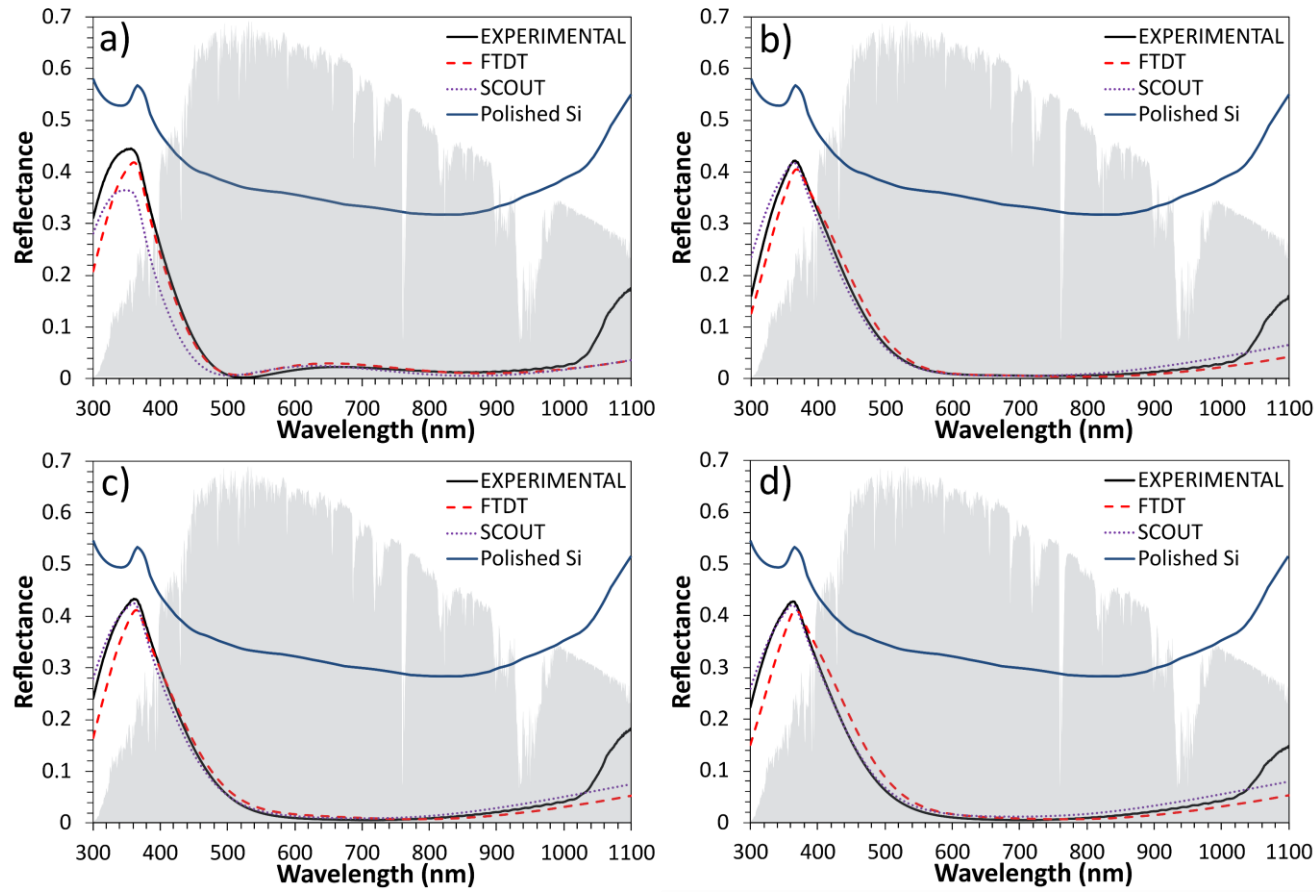


Figure 6 – Model of antireflection structure of samples:

- a) SiC 100W +  $\text{MgF}_2$ ;
- b) SiC 150W +  $\text{MgF}_2$ ;
- c) SiC 200W +  $\text{MgF}_2$ ;
- d) SiC 250W +  $\text{MgF}_2$

The theoretical and experimental curves obtained from SiC films deposited at a power of 100, 150, 200 and 250 W are very close (Fig. 7 (a-d)). In the case of actually synthesized coatings, it was possible to approach to the minimum reflection values of 0.2–3.0% (100 W, 475–1020 nm), 0.55–3.0% (150 W, 535–1005 nm), 0.66–3.0% (200 W, 530–947 nm), 0.57–3% (250 W, 537–938 nm), achieved during optimization using Lumerical FDTD and SCOUT. In case of 100 W and 150 W, the Lumerical FDTD gives a reflection spectrum closer to the experimental values. In case of 200 W, the reflectance curve obtained using SCOUT software is in better agreement with the experimental curve, especially in the range of 300–360 nm and 470–650 nm. For 250 W, the fit with the experimental curve is better for the SCOUT curve everywhere except in the 650–950 nm region.



**Figure 7 – Reflection spectra in the Si/SiC/MgF<sub>2</sub> system, for SiC layers ~ 50 nm thick, deposited under different power of the magnetron:**

- a) SiC 100W + MgF<sub>2</sub>;
- b) SiC 150W + MgF<sub>2</sub>;
- c) SiC 200W + MgF<sub>2</sub>;
- d) SiC 250W + MgF<sub>2</sub>



The best antireflection effect was achieved by using SiC/MgF<sub>2</sub> coatings containing silicon carbide film deposited at a magnetron power of 100 W. This is due to the optimal refractive index for creating a gradient structure with a decreasing refractive index from the substrate ( $n_{\text{sub}}$ ) to the medium ( $n_{\text{air}}$ ).

Simulations has showed that optimal parameters for the synthesis of antireflection SiC layers in the SiC/MgF<sub>2</sub> coating are 100 W/50 nm, at these parameters the reflection is below 3% in the widest wavelength range of 475–1020 nm.

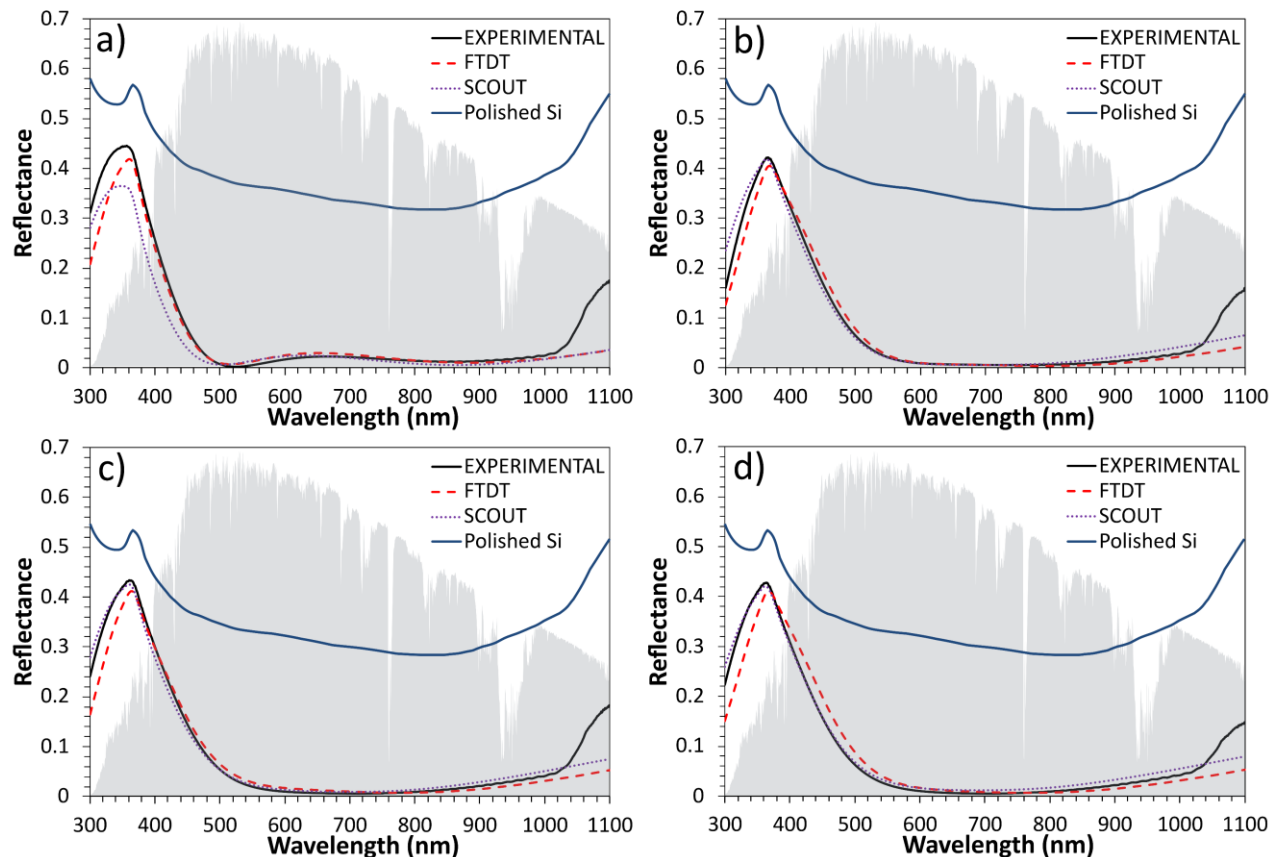


Figure 7 – Reflection spectra in the Si/SiC/MgF<sub>2</sub> system, for SiC layers ~ 50 nm thick, deposited under different power of the magnetron:  
a) SiC 100W + MgF<sub>2</sub>;  
b) SiC 150W + MgF<sub>2</sub>;  
c) SiC 200W + MgF<sub>2</sub>;  
d) SiC 250W + MgF<sub>2</sub>

The optimal thickness of SiC film for an antireflection coating was 5 determined by computer simulations using Lumerical FDTD and SCOUT software. The simulation was carried out for the SiC/MgF<sub>2</sub> system, where silicon carbide films were deposited at a magnetron power of 100, 150, 200, 250 W, while the thickness of the magnesium fluoride films remained unchanged and amounted to 130 nm. The simulation results showed that the optimal parameters for the synthesis of SiC antireflection layer are 100W/50nm. With these parameters, the reflection is less than 3% in the widest wavelength range of 475-1020 nm. The dependence of the physical properties of the synthesized films on the power of the magnetron is investigated. Using reflection and transmission spectroscopy it was experimentally revealed that a decrease in the magnetron power from 250 to 100 W leads to a decrease in the refractive index. According to our results the best antireflection effect can be achieved with SiC/MgF<sub>2</sub> coatings when SiC films are deposited at 100 W magnetron power. The reflectance spectra are consistent with the simulation spectra, especially in the 475-1020 nm range, where the surface reflects only 0.2-3.0% of the incident light. The obtained results are explained by the correlation between the structural properties, composition of amorphous silicon carbide films and antireflection properties.

**(“Optical Materials”, 2022. IF3.75)**